Modeling Particle-Laden Compressible Flows with an Application to Plume-Surface Interactions

by

Gregory Steven Shallcross

A dissertation submitted in partial fulfillment
of the requirements for the degree of
Doctor of Philosophy
(Mechanical Engineering and Scientific Computing)
in The University of Michigan
2021

Doctoral Committee:

Assistant Professor Jesse Capecelatro, Chair
Associate Professor Eric Johnsen
Professor Venkat Raman
Assistant Professor Aaron Towne

Gregory Steven Shallcross

grshall@umich.edu

ORCID iD: 0000-0002-3004-8350

For my family.

ACKNOWLEDGEMENTS

Before I begin I want to say thank you to my parents Mary Ann and Steven and my brother Michael Shallcross. Throughout my life, they have always offered their love and support, encouraging me to pursue my interests and excel in everything I do. They have always been there for me when others expressed doubt in my abilities, reminding me that I can do anything I put my mind to. I would not be who I am today without them.

Next, I want to say thank you to my advisor Prof. Capecelatro for giving me the opportunity to pursue a PhD at the University of Michigan. He has a deep understanding and interest in computational fluid dynamics and multiphase flows which regularly carries over to our conversations outside of the lab. I admire his enthusiasm for research and the work we do as students. His drive, determination, and supportive nature makes research hurdles easier to overcome. In addition, I want to say thank you to the rest of my committee members Prof. Venkat Raman, Prof. Eric Johnsen, and Prof. Aaron Towne. Their lectures, coursework, and discussions prepared me for the challenges I faced as a graduate student. In short, they improved my fundamental understanding of fluid dynamics, turbulence, multiphase flows, and computational modeling, all of which contributed to this work.

Outside of Michigan, I want to thank my mentors while interning at NASA facilities. This includes Jason Rabinovitch, Francisco Canabal, Josh Wilson, Chris Morris, and Manish Mehta. I enjoyed our discussions on research and related engineering topics. It was always fun to talk about abstract problems that usually led to

whiteboard sessions or random derivations. In addition, I want to thank my collaborators especially, David Buchta and Rodney Fox. Working with them was a pleasure. From earlier in my academic career, I want to thank my undergraduate mentors Prof. Haibo Dong and Dr. Don (Dojo) Jordan. They inspired me to pursue a PhD in computational fluid dynamics and I will forever be grateful for their support and advice over the years.

Lastly, I want to say thank you to all of the friends I've made along the way, especially Sarah Beetham, Aaron Lattanzi, Yuan Yao, Ali Kord, Meet Patel, Griffin Cearley, Kazuya Murakami, Angela Wu, and Lucca Henrion. From the late nights working on coursework to taking breaks to talk about life outside of research, they have helped me get through the past five years. I wish them all success for life after research at the University of Michigan.

This work was supported by a NASA Space Technology Research Fellowship. Computational resources were provided by the Advanced Research Computing Technology Services at the University of Michigan.

TABLE OF CONTENTS

DEDICATION ii

ACKNOWLEDGEMENTS iii

LIST OF FIGURES viii

LIST OF TABLES xiv

LIST OF APPENDICES xvi

ABSTRACT xvii

CHAPTER

I. Introduction 1

1.1 Background and motivation 1
1.2 Physics of PSI 3
1.3 Experimental studies of PSI 7
1.4 Summary of numerical approaches 9
1.5 Numerical simulations of PSI 11
1.6 Particle-laden compressible flows 13
1.7 Objectives and Goals 16
1.8 Organization of the Dissertation 18

II. Volume Filtered Formulation 19

2.1 Introduction 19
2.2 Microscale (model-free) equations 19
2.3 Filtered equations of motion 21
2.3.1 Volume-filter operators 21
2.3.2 Filtered mass conservation 23
2.3.3 Filtered momentum 23
2.3.4 Filtered energy 25
2.4 Filtered particle equations of motion 31

2.5 A summary of unclosed terms 31

III. Assessment of the Compressible Eulerian–Lagrangian Method 33

3.1 Introduction 33
3.1.1 Fluid-phase description 34
3.1.2 Particle-phase description 34
3.2 Discretization 35
3.2.1 Consistent interphase exchange 37
3.2.2 Assessment of the numerical method 38
3.2.3 Two-dimensional shock particle curtain analysis . . 41
3.2.4 Three-dimensional shock particle curtain analysis . 45
3.3 Conclusions 49

IV. New Immersed Boundary Method for Compressible Flows . 51

4.1 Introduction 51
4.2 Purely explicit, characteristic-based volume penalization . . . 54
4.3 Signed-distance levelset 55
4.4 Traditional characteristic-based volume penalization 55
4.4.1 Dirichlet condition 55
4.4.2 Neumann condition 56
4.4.3 Free-slip condition 56
4.5 Discussion on the penalization parameters 57
4.6 Regularization 59
4.7 Application to the Navier–Stokes equations 60
4.8 Application to the Euler equations 62
4.9 Results and discussion 64
4.9.1 Inviscid flows 64
4.9.2 Viscous flows 76
4.10 Conclusions 82

V. Quantification of Unclosed Terms during Shock-Particle Interactions 84

5.1 Introduction 84
5.2 *A posteriori* analysis 85
5.2.1 Simulation configuration 86
5.2.2 Discretization of the microscale equations 87
5.2.3 Role of filtering on the Mach number 89
5.2.4 Role of filtering on the velocity fluctuations 91
5.2.5 Assessment of the unclosed terms 94
5.3 Coarse-grained modeling 98
5.3.1 Modeling PTKE and the pseudo-turbulent Reynolds stresses 98

5.3.2 Discretization of the volume-filtered equations . . . 102
5.3.3 Verification – a converging-diverging nozzle 102
5.3.4 Modeling PTKE in a two-dimensional shock-particle configuration 103
5.3.5 Modeling PTKE in a three-dimensional shock-particle configuration 108
5.4 Conclusions 112

VI. Eulerian–Lagrangian Simulations of Plume-Surface Interactions 114

6.1 Introduction 114
6.2 Governing equations 116
6.2.1 Fluid-phase equations 116
6.2.2 Particle-phase description 116
6.3 System description 119
6.4 Numerics 120
6.4.1 Nozzle geometry and initial conditions 121
6.5 Single-phase jet impingement validation 123
6.5.1 Mean velocity magnitude and centerline velocity comparison 123
6.5.2 Surface pressure comparison 125
6.6 Multi-phase PSI 127
6.6.1 Joint probability density functions of particle volume fraction versus Mach and Reynolds number 129
6.6.2 Granular temperature 130
6.6.3 Vertical particle motion in the granular bed 132
6.7 Conclusions 135

VII. Conclusions 137

7.1 Summary of achievements 137
7.2 Prospectives on Future work 141
7.2.1 Modeling particle forces in compressible flows 141
7.2.2 Modeling unresolved contributions in particle-laden compressible flows 144
7.2.3 Multiphase PSI studies 145

APPENDICES 148
A.1 Details on evaluating surface quantities 149
B.1 Methodology for *a posteriori* filtering 154
B.2 Term reconstruction through approximate deconvolution . . . 155
B.3 Drag dependence on PTKE 157

BIBLIOGRAPHY 159

LIST OF FIGURES

Figure

1.1 Example of PSI and crater formation from Mars landing. Images adapted from NASA Jet Propulsion Laboratory (JPL) and Caltech. 2

1.2 Regimes of flow during PSI. Conditions are compiled from studies for different landing environments [148, 16]. This image is from a numerical simulation of jet impingement on a granular bed, details provided in Chapter VI. 5

1.3 Methods for numerical simulation of particle-laden compressible flows. Lander image (on the right) adapted from NASA Marshall Space Flight Center and Jacobs/ESSCA. 10

1.4 Schematic of a shock-particle interaction at an initial state (a) and some later time (b). 17

3.1 (a) Pressure and (b) density profiles of each phase (lines) compared against the reference case from Saito et al. [202] (symbols). 40

3.2 (a) Pressure profiles and (b) density profiles of the fluid and particle phases with $\delta_f = 0$ (a)–(b) and $\delta_f = 10d_p$ (c)–(d). 41

3.3 Two-dimensional (a) pressure profiles and (b) particle spreading rates for cases D1-D4. 46

3.4 Two-dimensional (a) pressure profiles and (b) particle spreading rates for cases E1-E3. 46

3.5 Two-dimensional (a) pressure profiles and (b) particle spreading rates for cases F1-F4. 47

3.6 Two-dimensional (a) pressure profiles and (b) particle spreading rates for cases H1-H4. 47

3.7 Two-dimensional (a) pressure profiles and (b) particle spreading rates for cases G1-G4. 48

3.8 Three-dimensional (a) pressure profiles and (b) particle spreading rates for different drag laws for cases I1-I4. 48

3.9 Three-dimensional (a) pressure profiles and (b) particle spreading rates for collisional for cases J1-J2. 49

4.1 Masking function $\mathcal{X}$ typically employed in CBVP (- - -) and the proposed regularized function $\widetilde{\mathcal{X}}$ with $\epsilon = 1.5\Delta$ (—). Region where the fluid equations are solved is highlighted in blue and the region in which the penalized terms are applied is highlighted in red. 61

4.2 L_2 error norm of an acoustic wave interacting with a vertical wall (a) aligned with the grid and (b) offset from the grid for $\epsilon = 0$ (■) and $\epsilon = 1.5\Delta$ (▲). Lines of convergence are shown for $\mathcal{O}(\Delta x)$ (· · ·) and $\mathcal{O}(\Delta x^2)$ (- - -). 66

4.3 Mach number contours for an inviscid flow past a stationary cylinder (shown in red) with $\Delta x = D/40$. Contour lines are evenly spaced on a scale ranging from 0 to 0.2. 68

4.4 Surface pressure coefficient for potential flow around a cylinder with $\Delta x = D/20$ (-●-), $\Delta x = D/40$ (- - -), $\Delta x = D/80$ (····), $\Delta x = D/160$ (- -), and the analytic solution (4.19) (—). 69

4.5 Evolution of drag coefficient for an oscillating cylinder in an inviscid fluid with $\Delta x = D/40$ and $\epsilon = 0$ (—), $\epsilon = 1.5\Delta$ (—), $\epsilon = 3\Delta$ (—). Analytic solution given by Eq. (4.21) (- - -). 72

4.6 Instantaneous temperature field for a $\mathrm{Ma}_\infty = 2$ flow past a two-dimensional wedge with $\epsilon = 0$. Theoretical shock wave angle (- - -). . 73

4.7 Temporal evolution of the coefficient of drag during a shock-cylinder interaction with $\mathrm{Ma}_s = 1.3$. $\Delta x = D/40$ and $\epsilon = 0$ (-●-), $\Delta x = D/80$ and $\epsilon = 0$ (- - -), $\Delta x = D/40$ and $\epsilon = 1.5\Delta$ (····), and $\Delta x = D/80$ and $\epsilon = 1.5\Delta$ (—). Experimental data (○) [229, 134] and numerical data using adaptive grid refinement (- - -) [54, 134]. Here, t_o corresponds to the instant the shock interacts with the cylinder. 75

4.8 Unsteady drag coefficient for a $\mathrm{Ma}_s = 1.22$ shock interacting with a sphere with $\Delta x = D/40$. $\epsilon = 0$ (- - -), $\epsilon = 1.5\Delta$ (·····), experimental data [222] (—), and a reference line indicating $C_D = 0$ (·····). Here, $(t - t_o) = 0$ corresponds to the instant the shock begins to interact with the sphere. 76

4.9 Coefficient of pressure for a steady flow interacting with circular cylinder at $\mathrm{Ma}_\infty = 0.1$ and $\mathrm{Re} = 300$. (a) $\Delta x = D/40$ with $\epsilon = 0$ (—) and $\Delta x = D/80$ with $\epsilon = 0$ (····). (b) $\Delta x = D/40$ with $\epsilon = \Delta$ (-●-), $\epsilon = 1.5\Delta$ (-·-·-), and $\epsilon = 3\Delta$ (····). Numerical body-fitted data [193] (△). 77

4.10 Velocity dilation $(\nabla \cdot \boldsymbol{u})D/u_\infty$ for a viscous subsonic flow past a cylinder with $\Delta x = D/40$ at $(t\,u_\infty)/D = 460$. Dilatation varies between -2.6 (black) and 2.6 (white). 78

4.11 Coefficient of pressure for a steady flow past a circular cylinder at $\mathrm{Ma}_\infty = 2$ and $\mathrm{Re} = 300$. (a) $\Delta x = D/40$ (—) and $\Delta x = D/80$ (····) with $\epsilon = 0$. (b) $\Delta x = D/40$ for $\epsilon = \Delta$ (-●-), $\epsilon = 1.5\Delta$ (-·-·-), and $\epsilon = 3\Delta$ (····). Numerical body-fitted data [228] (□). 80

5.1 Mach number fields (color) for $\varphi_p = 0.21$. Contours of $\mathrm{Ma} = 1$ (—). 88

5.2 Mach number (left) and particle volume fraction (right) as a function of filter size for $\varphi_p = 0.21$ when $t = 2.334$. Contours of $\mathrm{Ma} = 1$ (—). 90

5.3 Relative contributions of the fluctuating kinetic energy averaged across the entire domain. Filtered fluctuations, $\langle \widetilde{\boldsymbol{u}} \cdot \widetilde{\boldsymbol{u}} \rangle_{xy} - \langle \widetilde{\boldsymbol{u}} \rangle_{xy} \cdot \langle \widetilde{\boldsymbol{u}} \rangle_{xy}$ (-●-), and sub-filtered fluctuations, $\langle \boldsymbol{u} \cdot \boldsymbol{u} \rangle_{xy} - \langle \widetilde{\boldsymbol{u}} \cdot \widetilde{\boldsymbol{u}} \rangle_{xy}$ (··■··), as a function of filter size for $\varphi_p = 0.21$ when $t = 2.334$, normalized by the total fluctuating energy. 92

5.4 Comparison of PTKE obtained from ensemble averaging (—) and volume filtering with $\delta_f = d_p$ (- - -), $\delta_f = 2d_p$ (·····), $\delta_f = 4d_p$ (-·-·-), and $\delta_f = 8d_p$ (—) at $t = 2.334$. The shaded region (■) indicates particle location. 93

5.5 Filter size dependent Knudsen number as a function of φ_p with $\delta_f = d_p$, (—), $\delta_f = 2d_p$ (—), $\delta_f = 4d_p$ (—), and $\delta_f = 8d_p$ (—). Reference lines are also shown for $\mathrm{Kn}_\delta = 1$ (· · ·) and the three volume fractions under consideration (- - -). 95

5.6 Magnitude of the Favre averaged sub-filtered stresses appearing in Eq. (2.30) as a function of filter size for $(a)-(b)$ $\varphi_p = 0.04$, $(c)-(d)$ $\varphi_p = 0.21$, and $(e)-(f)$ $\varphi_p = 0.44$ when $t = 2.334$. $\langle|\overline{p}\widetilde{\boldsymbol{u}}|\rangle_y$ (—), $\langle|\boldsymbol{R}_{Tu}|\rangle_y$ (- - -), $\langle|\boldsymbol{R}_{\tau u}|\rangle_y$ (- - -), $1/2\langle|\boldsymbol{R}_{uu}|\rangle_y$ (·····), and $\langle|\boldsymbol{R}_u\cdot\widetilde{\boldsymbol{u}}|\rangle_y$ (- - -) normalized by $\rho_1 u_1^3$. The shaded region (■) indicates particle location. 96

5.7 Error in the pressure field as a consequence of excluding PTKE in Eq. 2.33 for $\varphi_p = 0.21$ when $t = 2.334$. Averaged error (—) and local error (color). The shaded region (■) indicates particle location. 97

5.8 Verification of a converging-diverging nozzle. 104

5.9 Power-law fit of the coefficient appearing in the dissipation model (5.3) to the two-dimensional simulations. Values extracted from DNS (●) and $C_f = 52\varphi_p^{1.5}$ (- - -). 105

5.10 Comparison of PTKE from filtered DNS (—) and VF-EL (- - -) with $\delta_f = 4d_p$. Coefficients of $C_f = 0.25,\ 5.0,$ and 15.0 were used for $\varphi_p = 0.04,\ 0.21,$ and 0.44, respectively. The shaded region (■) indicates particle location. 107

5.11 Instantaneous snapshot of PTKE from the two-dimensional VF-EL with $\varphi_p = 0.21$ at $t = 1.334$. 107

5.12 Instantaneous snapshot of local Mach number from the two-dimensional VF-EL with $\varphi_p = 0.21$ at $t = 1.334$. 108

5.13 Averaged $\rho k = \mathrm{tr}(\boldsymbol{R}_u)/2$ obtained from DNS [152] (-○-) and VF-EL (—) as a function of Mach number and volume fraction. $\mathrm{Ma}_s = 1.22$ evaluated at $t = 0.818$, $\mathrm{Ma}_s = 1.66$ at $t = 0.620$, and $\mathrm{Ma}_s = 3.00$ at $t = 0.237$. The shaded region (■) indicates particle location. 109

5.14 Components of the pseudo-turbulent Reynolds stress obtained from DNS [152] (symbols) and VF-EL (lines) as a function of Mach number and volume fraction. $\mathrm{Ma}_s = 1.22$ evaluated at $t = 0.818$, $\mathrm{Ma}_s = 1.66$ at $t = 0.620$, and $\mathrm{Ma}_s = 3.00$ at $t = 0.237$. DNS $R_u(1,1)$ (-○-), DNS $(R_u(2,2)+R_u(3,3))/2$ (-△-), VF-EL $R_u(1,1)$ (—), and VF-EL $(R_u(2,2)+R_u(3,3))/2$ (- - -). The shaded region (■) indicates particle location. 110

5.15 Coefficient appearing in the dissipation model (5.3) for three-dimensional simulations. Values extracted from $\varphi_p = 0.10$ (■) and $\varphi_p = 0.20$ (▲). Power-law fits for $\varphi_p = 0.10$ (—) and $\varphi_p = 0.19$ (- - -) given by $C_f = 150\mathrm{Ma}_s^{-10} + 83\varphi_p - 2$. 111

6.1 Diagram of inter-particle collisions. Image was adapted from Capecelatro and Desjardins [34] and modified for the presented notation. . 119

6.2 Nozzle configuration for jet impingement. 121

6.3 Nozzle geometry used for analytical levelset information. 123

6.4 Mean velocity magnitude contours for (a) $h_x/D_N = 2.08$, (b) $h_x/D_N = 3.65$, and (c) $h_x/D_N = 4.16$ with $NPR = 4.03$, $D/\Delta x = 40$, and a lip thickness of $0.5\,D$. Results on the left of each image are the time-averaged numerical results while results on the right are images courtesy of Henderson et al. [77]. 125

6.5 Mean centerline velocity plots for (a) $h_x/D_N = 2.08$, (b) $h_x/D_N = 3.65$, and (c) $h_x/D_N = 4.16$ with $NPR = 4.03$. Numerical data is indicated by (—) while experimental data from Henderson et al. [77] is indicated by (-o-). 126

6.6 Mean noramlized surface pressure plot for $h_x/D_N = 1.96$ and NPR = 2.69 for normalized radius, where r_N is the nozzle radius. Numerical data is indicated by (—) while experimental data from Snedeker et al. [216] is indicated by (····). 128

6.7 Sonic jet impingement on a granular bed with NPR = 4.03, $(h_x - h_b)/D_N = 3.65$, and $h_b = 1$ at time, $tD_N/u^* = 55.32$. The flow is colored by local Mach number while an iso-surface of volume fraction is included for $\alpha = 0.6$ to show the presence of the granular bed. . . 128

6.8 (a) Maximum particle Mach number and (b) maximum particle Reynolds number versus non-dimensional time during PSI at time $tD_N/u^* = 55.32$. 130

6.9 Granular temperature (Θ_p) visualized in log scale for different times. The nozzle outline is shown in white and corresponds to the levelset $\phi = 0$. A volume fraction contour for $\alpha = 0.6$ (teal) is also shown. . 133

6.10 Average Lagrangian particle velocity magnitude, conditioned by volume fraction, at $tD_N/u^* = 55.32$. 133

6.11 Average particle velocity in the x direction versus normalized radius in the particle bed at $tD_N/u^* = 55.32$. The particle velocity is averaged across cross sections in the x-direction for $x/D_N = 3.66$ (•), $x/D_N = 4.90$ (•), and $x/D_N = 6.13$ (•). 134

A.1 Illustration of the interpolation procedure used in this work. Masking function used in the volume penalization $\mathcal{X}$ (- - -) and modified Roma kernel (—). The red shading indicates the area of integration at a marker located at the surface of the immersed boundary (●). 150

B.1 Ensemble averaged PTKE obtained from DNS (—) and recovered from deconvolution with $\delta_f = d_p$ (- - -), $\delta_f = 2d_p$ (····), $\delta_f = 4d_p$ (-·-), and $\delta_f = 8d_p$ (—). Quantities are calculated for $\varphi_p = 0.21$ when $t = 2.334$. The shaded region ( ) indicates particle location. . 156

B.2 Effect of drag law on the components of the pseudo-turbulent Reynolds stress for $\varphi_p = 0.1$ and $\mathrm{Ma}_s = 1.66$ at $t = 0.62$. Same line types as in Fig. 5.14. 158

LIST OF TABLES

Table

1.1 Ambient atmospheric conditions [75] and environmental properties for Earth, Mars [186], and Titan [185, 80, 74, 76, 16] at an altitude of 0 km for each planetary body/satellite, respectively. 4

3.1 Parameters used in the Riemann problem. A1-A4 is a filtered grid refinement study and B1-B4 is an unfiltered grid refinement study. . 40

3.2 Two-dimensional shock tube cases. Where D1-D4 is a domain study for varying Ly, E1-E4 is a grid refinement study, F1-F5 is a an interphase filter study, and G1-G2 is a collisional study. 43

3.3 Three-dimensional shock tube cases. Where I1-I4 is a drag law analysis and J1-J2 is a collisional study. All described include $N_p = 36159$ particles 43

4.1 Results for drag coefficient (C_D), RMS coefficient of lift ($C_{L,RMS}$), and Strouhal number (Sr) for subsonic flow past a cylinder with $\Delta x = D/40$, unless otherwise specified, and different values of ϵ. 78

4.2 Results for drag coefficient (C_D), pressure drag coefficient ($C_{D,p}$), and frictional drag coefficient ($C_{D,f}$) for supersonic flow past a cylinder with $\Delta x = D/40$ unless otherwise labeled and different regularization parameters (ϵ). 80

4.3 Drag coefficient (C_D), pressure drag coefficient ($C_{D,p}$), frictional drag coefficient ($C_{D,f}$), and shock standoff distance (L_{shock}) for a viscous supersonic flow past a sphere. 81

5.1 A summary of gas-phase volume filtered equations of motion. 101

5.2 Parameters used in the three-dimensional shock-particle simulations. All simulations are performed with pre-shock conditions of $\rho_2 = 1$, $p_2 = 0.714$, and $u_2 = 0$. VF-EL is performed with $\delta_f = 4d_p$ and $\Delta x = d_p$. Further details on the DNS can be found in Mehta et al. [150, 151, 153, 152]. 108

A.1 Results for drag coefficient (C_D), pressure drag coefficient ($C_{D,p}$), and frictional drag coefficient ($C_{D,f}$) for supersonic flow past a cylinder with $\Delta x = D/80$ and $\epsilon = 0$ using surface integration Eq. (A.2) with the delta function proposed by Roma et al. [198] and the modified interpolation scheme, and volume integration Eq. (A.1). Results are compared to numerical body-fitted data [228]. 153

LIST OF APPENDICES

Appendix

A. Additional Information on CBVP Method 149

B. Additional Information on Volume-filter Formulation Analysis 154

ABSTRACT

During planetary descent, rocket plumes fluidize and eject surface granular matter. Consequently, ejected matter has been shown to obscure the landing site and even collide with the lander, causing serious damage. Given the high risk and cost of space exploration, the challenges associated with plume-surface interactions (PSI) are capable of jeopardizing future missions. The erosion, fluidization, and ejecta of granular matter during PSI occurs under transonic/supersonic, high Reynolds number conditions. These flow conditions pose significant challenges in both experimental and numerical analyses. To date, accurate and predictive physics-based models of PSI at relevant landing conditions do not exist.

The objective of this project is to develop high-fidelity simulation capabilities to model compressible gas-particle flows at conditions relevant to PSI. To start, a rigorous derivation of the volume-filtered (locally averaged) compressible Navier–Stokes equations is presented for the first time. This derivation reveals many unclosed terms, for which models are either non-existent or not valid under the regimes of interest. To this end, key terms including *pseudo*-turbulent kinetic energy and *pseudo*-turbulent Reynolds stresses, are isolated and modeled via a transport equation in a new high-order finite difference Eulerian-Lagrangian framework. A new immersed boundary method is introduced to generate highly resolved, multi-particle simulations for model closure development. Using the proposed immersed boundary method and the Eulerian–Lagrangian framework, high-fidelity PSI simulations are performed. Single-phase jet impingement on flat surfaces is first shown for validation of the flow conditions. The work is then extended to PSI over a granular bed. For this

case, it is shown that that ejected particles can exceed sonic speeds at high particle Reynolds numbers while the majority of the granular bed experiences subsonic particle Mach numbers. In addition, granular temperature is found to be most prevalent in region of high shear during crater formation.

The uniqueness of this work lies in the combination of first principles physics and numerics to generate a modeling framework to improve predictions of plume-surface interactions for future missions involving entry, descent, and landing on planetary and satellite bodies.

CHAPTER I

Introduction

1.1 Background and motivation

In the near future, there are several missions planned by the public and private sectors that involve planetary exploration. One major challenge with these missions is landing. During landing, rocket exhaust can interact with planetary surfaces commonly referred to as plume-surface interactions (PSI). PSI results in the motion of loose granular matter which can be expelled towards the spacecraft. This can result in serious damage by colliding with the craft, hindering load-baring capacity due to the formation of large craters, and spoofing sensors from inhibited visibility [24, 166]. See Fig. 1.1 for an example of crater formation due to PSI during the Mars Curiosity Rover landing. During the Apollo 12 mission to the Moon in 1969, the Surveyor 3 craft experienced damage akin to "*sand-blasting and pitting*" from granular matter transported by the Apollo lander during descent [46, 155, 91]. In this same mission, it was described that the granular matter "*degraded optical equipment*" and led to technical difficulties with other machinery, such as the moon buggy [135]. For such reasons, this led Apollo astronaut John Young to claim that,"*Dust is the number one concern in returning to the moon*" [135].

Attempts have been made to mitigate the effects of PSI events during entry, descent, and landing (EDL). For recent missions to Mars, EDL has been broken down

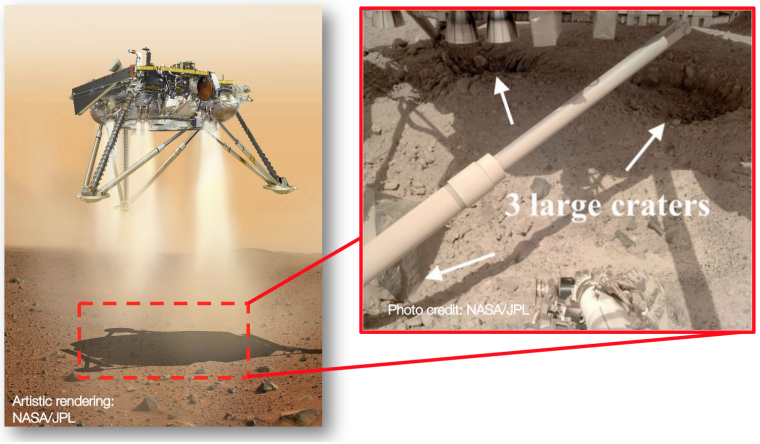

Figure 1.1: Example of PSI and crater formation from Mars landing. Images adapted from NASA Jet Propulsion Laboratory (JPL) and Caltech.

into four major parts; guided entry, parachute decent, powered descent, and the sky crane [137, 192, 110]. During the sky crane procedure, the spacecraft hovers above the planetary surface while its payload is slowly lowered with a series of cables. One purpose of the sky crane is to keep the rocket exhaust far away from the Martian surface which in turn should result in less severe PSI events. Regardless, it is still possible to experience damage while landing. For example during the Mars Curiosity Rover landing, the craft hovered approximately 7.5 m above the Martian surface during the sky crane maneuver [192, 218]. Meanwhile, rocket plumes interacted with the planetary surface ejecting granular matter resulting in a damaged wind sensor [5].

Further modifications to EDL maneuvers are required to account for larger payloads and different landing environments for future missions. As the mass of a spacecraft increases, the efficiency of parachutes decrease for low altitude decent [42, 203]. To avoid this, alternative deceleration methods, such as inflatable aerodynamic decelerators and different aeroshell/parachute shapes, have been suggested [42, 122]. While such methods may slightly reduce the severity of PSI events due to improved deceleration, many of these techniques require some finite atmosphere to be effective. For rarefied environments, rocket powered descent is the most viable option. Unfortunately, these descent procedures can lead to the severe PSI events as previously

described for the Apollo 12 mission to the Moon [46, 155, 91] and the Mars Curiosity rover landing [5]. Overall, rocket assisted decent and consequently PSI are largely unavoidable during landing. Given the high risk and cost of space exploration, work must be done to characterize, model, and mitigate damage from PSI events which are capable of jeopardizing future missions.

1.2 Physics of PSI

PSI involves high-speed chemically reacting plumes interacting with a planetary surface. For both atmospheric and rarefied environments the near-plume region behaves as a continuum [166], therefore the Navier–Stokes equations can be used to simulate jet exhaust. This is justified by the Knudsen number, $\mathrm{Kn} = \lambda/L$ where λ is the mean free path and L is some characteristic length scale, being sufficiently low, $\mathrm{Kn} \ll 1$ [114], in the vicinity of the plume. For example, simulations have shown that plume impingement for lunar environmental conditions exhibit Knudsen numbers on the order of $O(10^{-4})$ in the vicinity of the jet exit which increases to $0.2 < \mathrm{Kn} < 2.5$ at about 10 nozzle radii away from the exit [239]. Under rarefied conditions, the continuum assumption is not valid farther away from the plume; therefore, kinetic-based equations of motion are more applicable [239, 166]. For the purposes of this work, it is assumed that not only the near-plume region but also the surrounding atmosphere act as a continuum. With this assumption, studies can be performed for planets and satellites including but not limited to Earth, Mars, and Titan. Conditions for applicable landing environments are included in Table 1.1.

As rocket exhaust interacts with a planetary surface, the flow can be characterized by the Reynolds number,

$$\mathrm{Re} = \frac{\rho U L}{\mu}, \tag{1.1}$$

where ρ is the density of the fluid, U is characteristic velocity, and μ is the dynamic

	Earth	Mars	Titan
Density, ρ (kg/m^3)	1.2	1.66×10^{-2}	5.35
Pressure, p (kPa)	101.325	0.900	147
Ratio of Specific Heats , γ	1.4	1.29	-
Dynamic Viscosity, μ (Pa $\cdot$ s)	1.8×10^{-5}	1.5×10^{-5}	6.26×10^{-6}
Gravity, g (m/s^2)	9.81	3.72	1.35
Speed of Sound, c (m/s)	343	244	$\sim 191 \pm 1.5$
Mean free path, λ (m)	$\sim 6.6 \times 10^{-8}$	$\sim 5.8 \times 10^{-6}$	$\sim 7 \times 10^{-8}$

Table 1.1: Ambient atmospheric conditions [75] and environmental properties for Earth, Mars [186], and Titan [185, 80, 74, 76, 16] at an altitude of 0 km for each planetary body/satellite, respectively.

viscosity; Mach number,

$$\mathrm{Ma} = \frac{U}{c}, \tag{1.2}$$

where c is the speed of sound; and particle volume fraction,

$$\phi_p = \frac{V_p}{V}, \tag{1.3}$$

where V_p is the volume of particles that occupies some finite volume, V. See Fig. 1.2 for a breakdown of the regimes of flow during PSI. Near the jet exit, Mach numbers can approach and exceed supersonic flows at high Reynolds numbers. For example, the Mars Phoenix lander and Curiosity rover experienced jet exit Mach numbers of $\mathrm{Ma}_e = 4.67$ and $\mathrm{Ma}_e = 5.08$ with jet Reynolds numbers of $\mathrm{Re} = 3.4 \times 10^5$ and $\mathrm{Re} = 5.0 \times 10^5$ respectively [148]. The high-speed nature of these flows leads to the formation of compressible structures after interacting with an impinging surface. This includes but is not limited to plate shocks, wall shocks, and stagnation bubbles [148]. This occurs in the vicinity of granular matter with volume fraction ranging between $\phi_p = 0$ in the region of the plume devoid of particles to close packing, $\phi_p = 0.63$ for spheres, at the surface.

In the stagnation bubble, recirculation occurs in the presence of deep beds of granular matter. This leads to fluidization, whereby solid particles moves dynamically

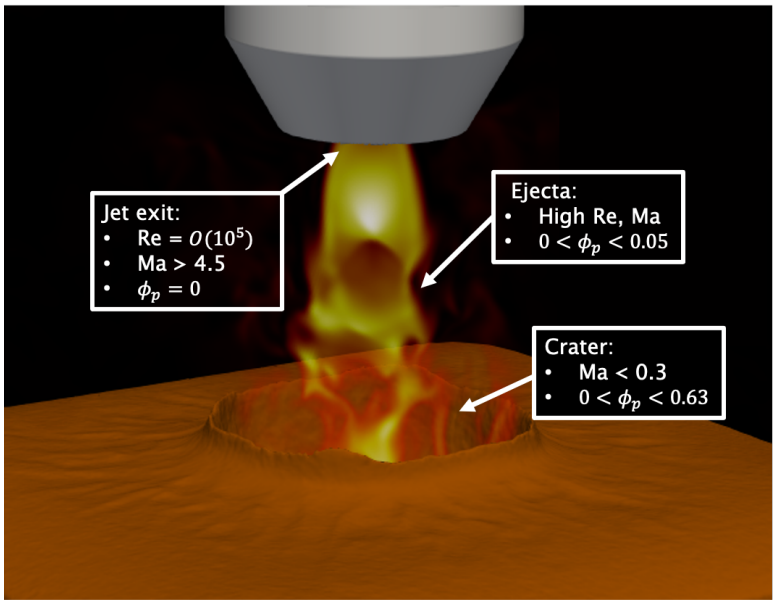

Figure 1.2: Regimes of flow during PSI. Conditions are compiled from studies for different landing environments [148, 16]. This image is from a numerical simulation of jet impingement on a granular bed, details provided in Chapter VI.

in a liquid-like manner [69]. For numerical simulations of PSI under Titan conditions, subsonic flow regimes were observed in this region in the presence of dense particle volume fractions ranging between $\phi_p = 0.45$ and closed packing. Meanwhile, these fluidized particles traveled at velocities between 0 m/s and 200 m/s [16]. Even with a jet exit Mach number of $\mathrm{Ma}_e = 1.5$ considered in the numerical simulations performed by Balakrishnan and Bellan [16], the local Reynolds number in the vicinity of the stagnation bubble is high due to the high speed flows within the viscous exhaust. During the fluidization process, dilute concentrations of particles, $\alpha_p < 0.05$, are periodically ejected. It was also reported that ejected particles can reach speeds up to ~ 350 m/s [16], which is fast enough to causing damage seen in previous missions [46, 155, 91, 5].

After interacting with the planetary surface, exhaust propagates outward from the landing zone forming a wall jet. As shown in Carling and Hunt [37] and highlighted by Mehta et al. [148], this phenomenon can result in transonic to supersonic

flow regimes at high Reynolds numbers. Consequently, these structures lead to flow induced surface stresses that can lift and propel additional granular matter during landing [155, 148]. As the flow moves radially away from the crater, the Mach number decays towards subsonic flow conditions. Even then, granular shear phenomenon can result in the transport of additional particle matter, similar to sediment based erosion [105, 107].

A wide range of flow regimes and physics are experienced during PSI, leading to mechanisms that cause granular erosion and crater formation during landing. As outlined in Metzger et al. [155], these mechanisms include viscous erosion [117, 90], bearing capacity failure [4], and diffused gas eruption [206]. During viscous erosion, the jet interacts with surface granular matter which is initially at rest. After overcoming local frictional forces for large particles or cohesive forces for smaller particles [117], the dynamic pressure of the flow acts to lift and propel granular matter away from the landing zone [90, 155]. Under bearing capacity failure, there exists jet conditions for which craters begin to form. After meeting some threshold, the static pressure of the jet exceeds the load bearing capacity of the surrounding granular material leading to rapid particle motion [4]. For diffused gas eruption, the jet flow is forced into the interstitial sites of particle matter via dynamic pressure [206, 155]. Consequently this can lift and propel large amounts of material during extended plume impingement events.

Later, two additional mechanisms were discovered, diffusion-driven flow and diffusive gas explosive erosion. Diffusion-driven flow occurs when flow induced forces "*...cause the soil to shear in the bulk.*" [155]. This leads to more prominent granular transport in the presence of deeper craters [155]. The final mechanism, diffusive gas explosive erosion, was identified by Mehta et al. [147] and occurs in the presence of pulsatile jets. During this phenomenon, "*cyclic shock waves*" form and propagate through the impinging surface, violently expelling large amounts of granular material

during landing [147].

1.3 Experimental studies of PSI

The physics and mechanisms described in Section 1.2 were partially discovered through observational imaging during landing and experiments of PSI. These methods have been the primary means to analyze crater formation with a goal of characterizing PSI and developing models for future missions.

During space exploration, images and videos are regularly taken during and after landing to study this phenomenon [206, 164, 89]. One example was the use of imaging during the Viking missions to Mars. Upon landing, images of the Martian surface were used classify granular matter composition and size during erosion [89]. While beneficial, the utility of these methods is limited. The small number of exploratory missions combined with technology limitations mean that the quantity and quality of data is short of what is needed to study PSI. In contrast, laboratory based experiments are repeatable and are capable of capturing high resolution images at rates required to potentially model this phenomenon [113].

Around the Surveyor and Apollo era, laboratory experiments were performed to characterize granular erosion and crater formation while landing on the Moon [197, 117, 4, 206]. An earlier study for jet impingement came from Roberts [196], leading to a deterministic model of crater formation and erosion. This model is based on the theory that crater formation is governed by the height of the impinging jet and resulting flow field. Using this information it is possible to predict the flow induced forces from viscous shear stresses on the granular surface from radial propagation of the exhaust during impingement [196, 90]. While elegant, this model does not always compare well against data for crater formation and erosion. When comparing to Roberts theory, Hutton [90] stated that "*... a factor of uncertainty of about 5 for erosion predictions is not excessive.*" The observed errors led to the model's

improvement over the years to account for effects like a polydisperse particle phase [90, 154].

This was followed by vacuum based studies from Land and Clark [117] where a $\mathrm{Ma}_e = 5$ jet was fired at granular beds while varying the nozzle pressure ratio and impingement height. It was revealed that after some critical height, the jet did not result in the erosion of granular matter. Experimental studies were further extended by using a descending rocket nozzle for standard Earth atmospheric conditions, as seen in Alexander et al. [4]. For some reported cases, granular matter was violently expelled 40 ft into the air while traveling in excess of 60 ft/s [4]. For both vacuum and atmospheric conditions, it was observed that soil properties and flow conditions had a significant effect on crater formation [117, 4]. The combination of these works set the groundwork for recent PSI experiments which aimed to tackle uncertainties in transient crater formation and ejecta phenomena [155, 156], albeit with some simplifying assumptions.

As highlighted in previous studies, it is difficult replicating planetary environmental conditions for standard laboratory experiments [4, 155]. Unfortunately, unless conditions match those experienced during landing, the physics of particle fluidization and ejection can be compromised. To remedy this, a recent experiment used a drop-tower in combination with a pressurized vessel to study this phenomenon [113], allowing test cases to mimic conditions for various landing environments. That being said, experiments could only be performed at relatively small scales. Apart from replicating environmental conditions, real-time jet impingement measurements are not straight forward. During PSI, fluidized granular matter prevents optical access to the rocket plume and the crater that forms. Instead, studies sometimes rely on post-experiment measurements [155, 23, 156] or introduce an intrusive optical window, such as a transparent wall, to measure crater formation [155]. Both methods are problematic and can lead measurement errors [117] or worse, modifications to the

impinging flow structure and the resulting physics of fluidization. To avoid this, other approaches like non-intrusive x-ray imaging have been used with some success [117].

In summary, there is a lot that can be learned from experimental PSI; however, it is difficult to execute accurate studies of plume impingement on granular beds. This has led to the development of cratering models based on rough landing images and measurements under non-applicable environmental conditions [196, 90, 154]. As a result, the subsequent models don't always capture the physics of PSI [90, 154]. These inaccuracies, among other factors, make numerical approaches an attractive alternative as they could potentially provide a high-resolution, non-intrusive framework for data collection and model development.

1.4 Summary of numerical approaches

Various methods can be used to perform numerical simulations of particle-laden compressible flows in PSI regimes, see Fig. 1.3. In the absence of modeling for a continuum flow regime, one can discretize and solve the Navier–Stokes equations directly and apply appropriate boundary conditions to the surface of each and every particle. This results in high-resolution data and is typically referred to as particle resolved direct numerical simulation (PR–DNS). For subsonic flows, PR–DNS has been performed for triply periodic systems of particles [79, 21, 233] leading to improved mean drag estimations on collections of spheres that are volume fraction dependent. Concerning high-speed compressible flows, there has been increasing interest in simulating fully resolve shock particle interactions [236, 238, 151, 153, 152, 172, 173]. Because sub-particle resolution is required, these simulations can be prohibitively expensive. Even with state-of-the-art high-performance computing clusters, simulations are limited to a relatively small number of particles, approximately $O(10^3)$ [234, 171, 152].

For a larger number of particles, one can formulate the equations of motion to solve for scales greater than the particle diameter. Obtaining a mathematical description

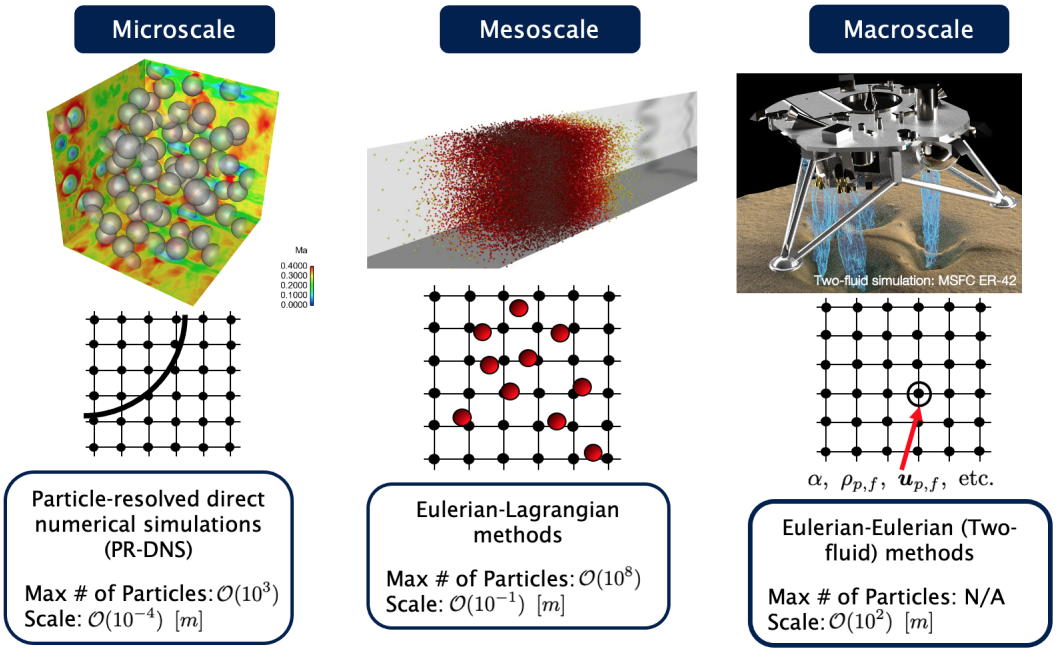

Figure 1.3: Methods for numerical simulation of particle-laden compressible flows. Lander image (on the right) adapted from NASA Marshall Space Flight Center and Jacobs/ESSCA.

that captures these two-phase flows typically involves ensemble averaging [258] or volume filtering [6, 34, 43, 13]. Sometimes referred to as mesoscale methods, each and every particle is tracked without needing to resolve stresses along individual particle surfaces. Similar to single-phase flows, averaging and filtering procedures inevitably result in unclosed terms that require modeling [189]. While some quantities from experiments or PR–DNS have a clear physical interpretation (e.g., the drag coefficient or heat transfer rate), their connection to these unclosed terms is not always obvious. This is especially true for high-speed flows whereby filtering or averaging the governing equations reveals quantities such as *pseudo*-turbulent Reynolds stresses and *pseudo*-turbulent kinetic energy that contain additional physics [13, 152, 214]. While less expensive than PR–DNS, mesoscale approaches require information to be stored for each and every particle, making these methods memory intensive as concentrations increase. As a result, modern simulations are limited to approximately

$O(10^8)$ particles, at least for incompressible flows [36].

For larger scale two-phase flows with high particle concentrations, it is common to assume that both the gas and particle phases act as continua. Commonly referred to as macroscale two-fluid approaches, the equations of motion can be derived and discretized in such a way that both the particle and fluid can be solved on an Eulerian grid [127, 85, 59]. Regardless of the formulation, information regarding individual particle motion is not tracked and consequently there is no computational limit to the number of particles for a given simulation. These methods are well suited for particle-laden flow problems where the computational domain is extremely large and there are high particle concentrations. Because of these properties, NASA has been heavily involved in developing and testing two-fluid models for PSI in recent years [149, 124, 13, 14, 66].

1.5 Numerical simulations of PSI

Recently, macroscale methods have employed using Reynolds Averaged Navier Stokes (RANS) or Large Eddy Simulation (LES) formulations to study PSI. With regards to RANS, it is possible to perform numerical simulations of a full landing site including specific immersed geometries that closely resemble the actual lander or rover of interest [208, 209, 148]. While these simulations provide substantial information regarding averaged impinging surface values, the referenced works are typically performed in the absence of particle. In comparison, recent two-fluid LES simulations have been performed for unsteady, high-resolution jet impingement on granular beds [13, 14, 15]. These studies involve supersonic jets for environmental conditions on Earth [13] and Titan [14, 15, 17]. In addition to qualitative comparisons to crater formation from landing images [13], the simulations provide information on particle-fluid coupling, such as force contributions during crater formation [15] and joint probability distribution functions showing that dense particle concentrations in

the crater predominately experience subsonic flow conditions [17].

Under PSI conditions, simulations need to account for a wide range of length-scales (i.e., small scale particle motion, large scale granular transport, etc.), time-scales (i.e., acoustic timescales, particle reaction time, etc.), and operating conditions. Due to high Reynolds numbers, Mach numbers, and particle concentrations, compressible two-fluid formulations heavily rely on modeling to account for unresolvable contributions in the flow. This can further complicate simulations when robust models are not available or even accurate under the conditions being considered. To provide closure to two-fluid methods for PSI, it is common to use models borrowed from incompressible flows for both the fluid and particle phases [13, 14]. In addition these models rely on a continuum assumption for the particle-phase. During particle ejection events, this assumption breaks down and can lead to errors. As a result, the accuracy of compressible two-fluid simulations can be compromised.

In summary, mesoscale methods are a promising approach to simulate large scale crater formation and ejecta dynamics; however, these methods need to be improved to make accurate predictions of PSI. As opposed to using existing single-phase incompressible closures, new physics-based models must be generated based on first principles. Unfortunately, microscale and mesoscale methods are not tractable alternatives to simulate a full landing site. Alternatively simple conical problems well suited for higher-resolution methods, can be used to isolate key physics of PSI and inform macroscale approaches. A range of studies involving compressible phenomena, shock-particle interactions, and particle-laden turbulence [24, 166] can be used for model development required for the PSI and particle-laden compressible flow communities.

1.6 Particle-laden compressible flows

PSI is characterized by two-phase gas-particle flows under a wide range of Reynolds numbers, Mach numbers and volume fractions. Physics-based simulation tools for predicting PSI requires a sound mathematical and physical description of compressible particle-laden flows. However, a consistent form of the averaged equations of motion remains elusive for these flows. Many different approaches have been used to derive an averaged set of equations that do not require resolving the microscale physics, ranging from energy balances and thermodynamic principles [127, 85] to kinetic theory [59]. The choice of formulation methodology may result in different unclosed terms or even a mathematical ill-posed set of equations [128, 121, 236, 238]. There are even debates on fundamentals, such as the proper form of particle-fluid coupling terms [127, 85, 236]. A clear set of equations needs to be established in order to inform model develop for under-resolved methods. Similar challenges exist for modeling particle motion in compressible flows.

Fluidized and ejected particles during PSI can experience a wide range of effects from phenomena like shock-particle and particle-turbulence interactions that have clear physical interpretations. This can be described by forces that arise in expressions like the Basset-Boussinesq-Oseen (BBO) and Maxey-Riley equations [18, 30, 170, 143, 178, 179]. For example, the BBO equation was originally formulated for an isolated spherical particle in the presence of a creeping flow in the limit of small Reynolds numbers. This is given by,

$$
\begin{aligned}
m_p \frac{d\boldsymbol{v}_p}{dt} = & \underbrace{3\pi\mu d_p \left(\boldsymbol{u}-\boldsymbol{v}_p\right)}_{\text{Stokes drag}} - \underbrace{V_p \nabla p}_{\text{Buoyancy}} + \underbrace{\frac{\rho_p V_p}{2}\frac{d}{dt}\left(\boldsymbol{u}-\boldsymbol{v}_p^{(i)}\right)}_{\text{Inviscid-unsteady}} \\
& \underbrace{+ \frac{3}{2} d_p^2 \sqrt{\pi\rho\mu} \int_{t_0}^{t} \frac{1}{\sqrt{t-\xi}} \frac{d}{d\xi}\left(\boldsymbol{u}-\boldsymbol{v}_p\right) d\xi}_{\text{Viscous-unsteady}} + \underbrace{\boldsymbol{F}_b}_{\text{Body forces}} .
\end{aligned}
\tag{1.4}
$$

Here $\boldsymbol{v}_p$ is the particle velocity, ρ_p is density of the particle, t is time, and d_p is the particle diameter. The terms on the right hand side account for Stokes drag, the resolved pressure gradient or buoyancy, added mass or inviscid-unsteady effects, Basset or viscous-unsteady effects, and additional body forces such as gravity [99, 178]. The equation was originally formulated for low Reynolds number, steady flows; however, the forces are still relevant to general particle motion. For large particle to fluid density ratios in the presence of some finite slip velocity, particle motion is dominated by drag. In the presence of a large pressure gradient, buoyancy forces are important. Unsteady effects are proportional to acceleration difference between the phases and fluid-to-particle density ratio. For incompressible gas-solid flows, these terms are often negligible. For compressible gas-solid flows, strong local acceleration can be generated by discontinuities like shock waves and thus they may be non-negligible [125, 126]. Considering compressible flow regimes, recent works have extended the BBO and Maxey-Riley equations for finite Mach and Reynolds numbers [178, 179]. While such relations exist, they are usually formulated for isolated particles. Particle suspensions at finite volume fraction and Reynolds numbers do not exhibit realistic forcing behavior.

Characterization of drag on spheres/particles for higher speed, compressible flows has been a topic of interest for hundreds of years [10, 44]. Examples of work date back to the 18th and 19th centuries where cannon-fire data was used to evaluate steady drag under high-speed flows [157]. Other studies have been performed to cover a wider range of Mach and Reynolds numbers as shown in Bailey and Hiatt [10] and Clift et al. [44]. Experimental studies combined with numerical works have led to improved drag correlations for a wide range of conditions such as those presented in Henderson [78] and Loth [133]. That being said, it is rather challenging to create correlations for drag on spheres for varying Mach number as opposed to traditional definitions that rely on Reynolds number. As discussed in Nagata et al. [167, 168],

flow behavior, such as shock strength and downstream recirculation, changes with Mach number which greatly affects the forces experienced by a sphere. The largest uncertainties exist for transonic regimes where other parameters relevant to heating and viscous effects can contribute to larger force variations. Existing models fail to capture these effects, prompting the need for detailed simulations under a wide range of flow conditions [167, 168, 261]. It is important to note that all of this work is for single particle motion. The physics associated with multi-particle interactions can have profound effects on particle forcing.

Studies involving low speed [1, 87, 55] and high-speed flows [151, 171, 172] exhibit a distribution of forces for multi-particle suspensions. As particles interact with the wakes of other particles, fluctuations in the flow can lead to variations in surface stresses and thus a distribution of force in the particle system. Simulations of multi-particle systems have been performed for modeling purposes; however, forces are typically averaged across the collection of simulated particles [79, 21, 233]. This means that only the mean in particle force is captured, even when accounting for particle concentrations through volume fraction corrections [69, 233, 126]. In addition, the wakes from particle-fluid and particle-particle interactions can lead to sub-particle fluctuations that are not captured for mesoscale and macroscales modeling approaches [13, 152, 214]. This includes *pseudo*-turbulent kinetic energy (PTKE) and *pseudo*-turbulent Reynolds stresses that can account for a large portion of the kinetic energy in compressible flows [84, 207, 171, 152]. There are very few models to capture these effects and those that do exist are limited by flow regime and or problem configuration [146, 172, 214].

To improve models for multi-particle systems in compressible flow regimes, different flow configurations have been considered. One example is shock-particle curtain interactions which are commonly used to study collective particle motion experimentally [126, 249, 250, 237, 52, 238, 53] and numerically [236, 238, 151, 153, 152, 172,

173]. As an illustrative example, consider the particle-laden shock-tube depicted in Fig. 1.4. A shock propagates through a fluid towards a collection of disperse particles (Fig. 1.4(a)). Shortly after it passes through (Fig. 1.4(b)), transmitted and reflected shocks form, wakes are generated (shown in grey), and the gas accelerates at the downstream edge of the particles. This leads to choking events where the local Mach number can exceed $\mathrm{Ma} = 1$. Meanwhile, data for temporal pressure measurements and particle spreading rates can be collected. This provides insight into large-scale particle motion in compressible flows, which can otherwise be difficult to isolate.

Other configurations, like particle-laden jets, also provide useful information related to high-speed particle-laden flows [217, 175, 108]. During these studies, particles are injected into under-expanded jets which exhibit sonic to supersonic flow regimes. With modern high-speed videography and predictive particle trajectory algorithms [174], data for individual particle trajectories and particle velocity distributions are captured for model development and numerical validation purposes [108, 256]. These techniques combined with Schlieren imaging, provide information on the modification of compressible flow structures in the presence of different particle loadings. Overall, the data extracted from this work provides insight into particle motion under flow regimes where improved models are required.

To summarize, there are many shortcomings associated with modeling particle-laden compressible flows. A set of filtered/averaged governing equations and applicable models do not exist within the literature for coarse grained multi-particle systems [121, 236, 238]. Thus, a systematic approach must be taken to improve predictions and simulations of complex engineering problems like PSI.

1.7 Objectives and Goals

The goal of this research is to formulate a numerical framework grounded in first principles for simulating compressible gas-particle flows to study plume-induced soil

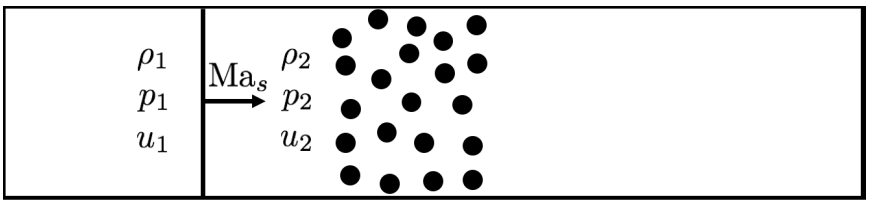

(a) $t = 0$

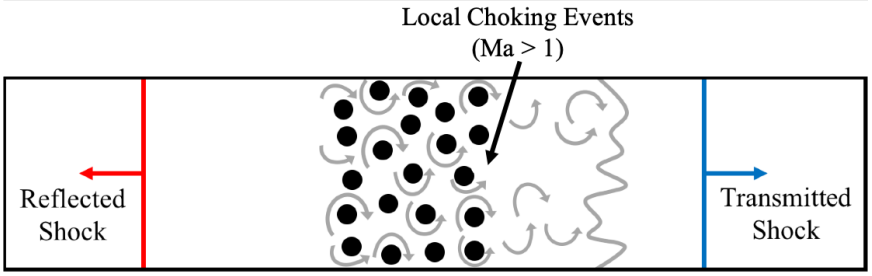

(b) $t > 0$

Figure 1.4: Schematic of a shock-particle interaction at an initial state (a) and some later time (b).

erosion. In this work, a volume-filtered Eulerian–Lagrangian approach is developed where particles are treated in a deterministic manner and coupled with a gas phase which is resolved at a scale larger than the particles. The primary objectives of this project include:

1. Derive a set of equations from first principles that act as a basis for model development.

2. Extract micro-physics from unclosed contributions in said formulation.

3. Develop reduced order closure models for key unclosed terms.

4. Perform simulations of plume-induced fluidization with the newly developed modeling framework and characterize cratering and ejecta dynamics.

These objectives will lead to a robust method for capturing relevant multiphase physics associated with particle-laden compressible flows. The numerical models and

methods developed here, in addition to new insight on the two-phase flow dynamics, will provide useful guidance for efforts in simulating full-scale landing sites.

1.8 Organization of the Dissertation

This dissertation consists of work completed in the form of manuscripts from journals and conference presentations that are in print, under review, or in preparation for future submission. The remainder of this document is organized as follows. In Chapter 2, the governing equations of motion are presented along with the numerical framework. Following, a rigorous derivation of the volume-filtered compressible Navier–Stokes equations is presented with a description of unclosed terms [33, 214]. In Chapter 3, the formulation is evaluated for standard Eulerian–Lagrangian studies for canonical shock-particle interactions [211]. For the purpose of creating high resolution data, an improved compressible flow immersed boundary method is introduced in Chapter 4 [213]. Using the high resolution data, unclosed terms from Chapter 2 are evaluation using an *a posteriori* filtering procedure in Chapter 5. With the information garnered from this analysis, a transport equation for *pseudo*-turbulent kinetic energy (PTKE) is proposed. Initial work regarding single and multiphase PSI studies is shown in Chapter 6 [212]. Finally, conclusions are drawn from this work and an outlook on the future of numerical simulations of particle-laden compressible flows and PSI is presented.

CHAPTER II

Volume Filtered Formulation

2.1 Introduction

Many methods have been employed to derive the governing equations motion for compressible multiphase flows. As described in Section 1.6 the combination of these approaches have led to issues regarding the presence of unclosed terms [127, 85, 59], the mathematical consistency of formulations [128, 121, 236], and proper treatment of particle fluid coupling [127, 85, 236]. Given the inconsistencies in literature, it can be argued that a correct form of the filtered or averaged equations of motion for compressible multiphase flows is an open problem. In this chapter, the described equations are re-derived using the volume filtering approach originally proposed by Anderson and Jackson [6]. This reveals a series of unclosed fluid and particle phase terms that may require modeling.

2.2 Microscale (model-free) equations

The governing equations describing a viscous compressible flow were originally introduced in Chapter I but are included here for reference. They are given by

$$\frac{\partial \rho}{\partial t} + \nabla \cdot (\rho \boldsymbol{u}) = 0, \tag{2.1}$$

$$\frac{\partial \rho \boldsymbol{u}}{\partial t} + \nabla \cdot (\rho \boldsymbol{u} \otimes \boldsymbol{u} + p\mathbb{I} - \boldsymbol{\tau}) = 0, \tag{2.2}$$

and

$$\frac{\partial \rho E}{\partial t} + \nabla \cdot (\{\rho E + p\}\boldsymbol{u} + \boldsymbol{q} - \boldsymbol{u} \cdot \boldsymbol{\tau}) = 0, \tag{2.3}$$

where each variable denotes a microscale quantity (i.e., a scalar or vector field at a scale smaller than an individual particle). Here, $\mathbb{I}$ is the identity matrix, ρ is the density, $\boldsymbol{u}$ is the velocity, p is the pressure, and E is the total energy. In this work, all variables are non-dimensionalized with the ambient density $\rho^\star_\infty$, a characteristic length scale $L^\star$, dynamic viscosity μ_∞, heat capacity at constant pressure $C^\star_p$, and speed of sound $c^\star_\infty = \sqrt{\gamma p^\star_\infty / \rho^\star_\infty}$ with constant $\gamma = 1.4$ the specific heat ratio and $p^\star_\infty$ the ambient pressure. All dimensional quantities are denoted by a superscript $\star$, and the subscript ∞ indicates a reference quantity (taken to be air at ambient conditions).

The non-dimensional viscous stress tensor can be expressed as

$$\boldsymbol{\tau} = \frac{\mu}{\mathrm{Re}_c}\left(\nabla \boldsymbol{u} + \nabla \boldsymbol{u}^\mathsf{T}\right) + \frac{\lambda}{\mathrm{Re}_c}\nabla \cdot \boldsymbol{u}\mathbb{I}, \tag{2.4}$$

and the non-dimensional heat flux is

$$\boldsymbol{q} = -\frac{\mu}{\mathrm{Re}_c \mathrm{Pr}}\nabla T, \tag{2.5}$$

where $\mathrm{Pr} \equiv \mathrm{C_p^\star}\mu^\star/\mathrm{k}^\star$ is the Prandtl number with $\mu^\star$ and $k^\star$ the dynamic viscosity and thermal conductivity, respectively. The Reynolds number based on the reference sound speed is defined as $\mathrm{Re}_c = \mathrm{Re}/\mathrm{Ma}_c$, where $\mathrm{Re} = \rho^\star_\infty \mathrm{U}^\star \mathrm{L}^\star / \mu^\star_\infty$ is the flow Reynolds number with $U^\star$ a characteristic velocity, and $\mathrm{Ma}_c = U^\star / c^\star_\infty$ is the reference Mach number. In this work, the non-dimensional viscosity is modeled as a power law $\mu = [(\gamma - 1)T]^n$, with $n = 0.666$ as a model for air. The second coefficient of viscosity is given by $\lambda = \mu_B - \frac{2}{3}\mu$ where the bulk viscosity $\mu_B = 0.6\mu$ is chosen as a model

for bulk viscosity of air. The thermodynamic pressure, p, and temperature, T, are obtained via the equation of state for an ideal gas, given in non-dimensional form as

$$T = \frac{\gamma p}{(\gamma - 1)\rho} \quad \text{and} \quad p = (\gamma - 1)\left(\rho E - \frac{1}{2}\rho \boldsymbol{u} \cdot \boldsymbol{u}\right). \tag{2.6}$$

2.3 Filtered equations of motion

Here the filtered equations of motion for particle-laden flows are presented. Additional details can be found in Shallcross et al. [214]. This section follows the volume-filtering procedure originally proposed Anderson and Jackson [6], extending it to the compressible form of the Navier–Stokes equations. Note that filtering and averaging procedures have been attempted for multi-phase compressible flows [92, 13]; however, a through derivation including all unclosed contributions and a description of the process has not been shown.

2.3.1 Volume-filter operators

In order to account for the effect of particles without requiring to resolve the fluid-phase equations on the scale of the particle surface, the Navier–Stokes equations are split into microscale (sub particle-scale) processes, and mesoscale processes, i.e., processes that take place on a scale larger than the particle diameter. Following Anderson and Jackson [6], we begin by defining a filtering kernel $\mathcal{G}$ with a characteristic length δ_f, such that $\mathcal{G}(r) > 0$ decreases monotonically with increasing r, and is normalized such that its integral over the entire physical space is unity. The local voidage at a point $\boldsymbol{x}$ and time t is defined as

$$\alpha\left(\boldsymbol{x}, t\right) = \int_{\mathcal{V}} \mathcal{I}(\boldsymbol{y}) \mathcal{G}(|\boldsymbol{x} - \boldsymbol{y}|) \ \mathrm{d}\boldsymbol{y} = \int_{\mathcal{V}_f} \mathcal{G}(|\boldsymbol{x} - \boldsymbol{y}|) \ \mathrm{d}\boldsymbol{y}, \tag{2.7}$$

where $\mathcal{V}$ indicates that the integral is taken over all points $\boldsymbol{y}$ occupied by the fluid-particle system and $\mathcal{I}$ is an indicator function defined as

$$\mathcal{I}(\boldsymbol{y}) = \begin{cases} 1 & \text{if fluid} \\ 0 & \text{otherwise.} \end{cases} \tag{2.8}$$

To abbreviate the notation throughout the remainder of this section, the integral will be taken over $\mathcal{V}_f$, all points $\boldsymbol{y}$ occupied by the fluid. Taking $\delta_f \gg d_p$, with d_p the particle diameter, and assuming $\mathcal{G}$ varies little over the surface of a particle, the particle volume fraction can be expressed as

$$\alpha_p(\boldsymbol{x}, t) = 1 - \alpha \approx \sum_{i=1}^{N_p} \mathcal{G}\big(|\boldsymbol{x} - \boldsymbol{x}_p^{(i)}|\big)\, \mathcal{V}_p^{(i)}, \tag{2.9}$$

where N_p is the total number of particles in the system, and $\boldsymbol{x}_p^{(i)}$ and $\mathcal{V}_p^{(i)}$ are the position and volume of the i-th particle, respectively.

Any flow quantity $\boldsymbol{a}(\boldsymbol{x}, t)$ can be decomposed into filtered and sub-filtered components such that $\boldsymbol{a}(\boldsymbol{x}, t) = \overline{\boldsymbol{a}}(\boldsymbol{x}, t) + \boldsymbol{a}'(\boldsymbol{x}, t)$, where the volume filtered quantity is given by

$$\alpha\overline{\boldsymbol{a}}(\boldsymbol{x}, t) = \int_{\mathcal{V}_f} \boldsymbol{a}(\boldsymbol{y}, t)\; \mathcal{G}(|\boldsymbol{x} - \boldsymbol{y}|)\; \mathrm{d}\boldsymbol{y}. \tag{2.10}$$

For convenience in the following formulation, we introduce a Favre filtered quantity $\widetilde{\boldsymbol{a}} = \overline{\rho\boldsymbol{a}}/\overline{\rho}$. With this, any fluid property $\boldsymbol{a}$ can be split into its associated Favre averaged and residual components as $\boldsymbol{a} = \widetilde{\boldsymbol{a}} + \boldsymbol{a}''$. Unlike ensemble averaging, the filtering operation invokes local spacial averaging and consequently volume filtered quantities are stochastic in nature such that $\overline{\boldsymbol{a}'} \neq 0$ and $\widetilde{\boldsymbol{a}''} \neq 0$.

2.3.2 Filtered mass conservation

Volume filtering the microscale density equation (2.1) yields

$$\frac{\partial \alpha \overline{\rho}}{\partial t} + \nabla \cdot (\alpha \overline{\rho} \widetilde{\boldsymbol{u}}) = 0, \tag{2.11}$$

and requires no closure.

2.3.3 Filtered momentum

While the derivation of the volume-filtered momentum equation can be found elsewhere [6, 34, 43], special care needs to be taken when considering high-speed flows. For example, volume filtering the pressure gradient term in (2.2) yields

$$\int_{\mathcal{V}_f} \nabla p \mathcal{G}(|\boldsymbol{x} - \boldsymbol{y}|) \ \mathrm{d}\boldsymbol{y} = \nabla (\alpha \overline{p}) - \sum_{i=1}^{N_p} \int_{\mathcal{S}_i} \boldsymbol{n} p \mathcal{G}(|\boldsymbol{x} - \boldsymbol{y}|) \ \mathrm{d}\boldsymbol{y}, \tag{2.12}$$

where $\boldsymbol{n}$ is the unit normal vector outward from the surface of the particle and $\boldsymbol{n}p$ represents the interfacial pressure at $\mathcal{S}_i$, the surface of particle 'i'. Decomposing the local pressure $p = \overline{p} + p'$, assuming the characteristic size of the filter kernel $\delta_f \gg d_p$ and applying the divergence theorem, the volume filtered pressure gradient can be expressed as

$$\int_{\mathcal{V}_f} \nabla p \mathcal{G}(|\boldsymbol{x} - \boldsymbol{y}|) \ \mathrm{d}\boldsymbol{y} = \nabla (\alpha \overline{p}) - \overline{p} \nabla \alpha - \sum_{i=1}^{N_p} \int_{\mathcal{S}_i} \boldsymbol{n} p' \mathcal{G}(|\boldsymbol{x} - \boldsymbol{y}|) \ \mathrm{d}\boldsymbol{y}, \tag{2.13}$$

where the last term on the right-hand side of (2.13) is typically modeled as a contribution to drag. In the context of compressible flows, $\overline{p} \nabla \alpha$ represents a nozzling term that accelerates the gas due to particles restricting the area where fluid can flow [85]. In low-Mach number flows, it is common to simplify the momentum equation by employing the product rule, i.e., $\nabla(\alpha \overline{p}) = \overline{p} \nabla \alpha + \alpha \nabla \overline{p}$, such that the non-conservative

nozzeling term $\overline{p}\nabla\alpha$ cancels out. As pointed out by Houim and Oran [85], the product rule is not valid when dealing with compressible flows in general. However, as discussed by Houim and Oran [85], assuming volume fraction is strictly determined from the position of the particle phase (i.e., fluid quantities are independent of particle density), the product rule will hold.

Applying the same procedure to the viscous stress tensor, the volume filtered momentum equation can be expressed as

$$\frac{\partial \alpha\overline{\rho}\widetilde{\boldsymbol{u}}}{\partial t} + \nabla\cdot\left(\alpha\left\{\overline{\rho}\widetilde{\boldsymbol{u}}\otimes\widetilde{\boldsymbol{u}} + \boldsymbol{R}_u\right\}\right) = \alpha\nabla\cdot\left(\overline{\boldsymbol{\tau}} - \overline{p}\mathbb{I}\right) + \boldsymbol{\mathcal{F}}. \tag{2.14}$$

In the above expression, the volume filtered stress tensor is

$$\overline{\boldsymbol{\tau}} = \frac{\widetilde{\mu}}{\mathrm{Re}_c}\left(\nabla\widetilde{\boldsymbol{u}} + \nabla\widetilde{\boldsymbol{u}}^{\mathsf{T}}\right) + \frac{\widetilde{\lambda}}{\mathrm{Re}_c}\nabla\cdot\widetilde{\boldsymbol{u}}\mathbb{I} + \boldsymbol{R}_\mu, \tag{2.15}$$

where the sub-filtered flux $\boldsymbol{R}_\mu$ is sometimes modeled as an effective viscosity (e.g., [258, 180, 68]).

In addition, $\boldsymbol{\mathcal{F}}$ is the sub-filtered momentum exchange term expressed as

$$\boldsymbol{\mathcal{F}} = \sum_{i=1}^{N_p}\int_{\mathcal{S}_i}\boldsymbol{n}\cdot\left(p'\mathbb{I} - \boldsymbol{\tau}'\right)\mathcal{G}(|\boldsymbol{x}-\boldsymbol{y}|)\ \mathrm{d}\boldsymbol{y}. \tag{2.16}$$

Finally, $\boldsymbol{R}_u$ is an unresolved stress that arises from filtering the non-linear convective term. This term is usually referred to as a pseudo-turbulent Reynolds stress [146] and is defined as

$$\boldsymbol{R}_u = \overline{\rho}\left(\widetilde{\boldsymbol{u}\otimes\boldsymbol{u}} - \widetilde{\boldsymbol{u}}\otimes\widetilde{\boldsymbol{u}}\right). \tag{2.17}$$

While this term is typically neglected in incompressible flow models, recent work has shown that these unresolved velocity fluctuations can contribute to a significant portion of the total kinetic energy during particle-shock interactions [84, 207, 152].

2.3.4 Filtered energy

Turning our attention now to the gas-phase energy equation (2.3), volume filtering the microscale heat flux yields

$$\int_{\mathcal{V}_f} \nabla \cdot \boldsymbol{q}\mathcal{G}(|\boldsymbol{x}-\boldsymbol{y}|)\ \mathrm{d}\boldsymbol{y} = \nabla \cdot (\alpha \overline{\boldsymbol{q}}) - \sum_{i=1}^{N_p} \int_{\mathcal{S}_i} \boldsymbol{n} \cdot \boldsymbol{q}\mathcal{G}(|\boldsymbol{x}-\boldsymbol{y}|)\ \mathrm{d}\boldsymbol{y}. \tag{2.18}$$

Decomposing the microscale heat flux into $\boldsymbol{q} = \overline{\boldsymbol{q}} + \boldsymbol{q}'$ and rearranging yields

$$\int_{\mathcal{V}_f} \nabla \cdot \boldsymbol{q}\mathcal{G}(|\boldsymbol{x}-\boldsymbol{y}|)\ \mathrm{d}\boldsymbol{y} = \alpha \nabla \cdot \overline{\boldsymbol{q}} - \mathcal{Q}, \tag{2.19}$$

where $\mathcal{Q}$ accounts for sub-filtered heat transfer at the particle surface typically modeled using a Nusselt number correlation (e.g., [72, 221]), defined as

$$\mathcal{Q} = \sum_{i=1}^{N_p} \int_{\mathcal{S}_i} \boldsymbol{n} \cdot \boldsymbol{q}'\mathcal{G}(|\boldsymbol{x}-\boldsymbol{y}|)\ \mathrm{d}\boldsymbol{y}. \tag{2.20}$$

and the volume filtered heat flux is

$$\overline{\boldsymbol{q}} = \frac{\widetilde{\mu}}{\mathrm{Re}_c \mathrm{Pr}} \nabla \widetilde{T} + \boldsymbol{R}_q. \tag{2.21}$$

Similar to the sub-filtered viscous stress tensor appearing in (2.15), in low-Mach number formulations $\boldsymbol{R}_q$ is sometimes modeled as an effective thermal conductivity to account for enhanced heat dissipation at the particle scale [224, 43, 73].

Volume filtering the work due to pressure in (2.3) yields

$$\int_{\mathcal{V}_f} \nabla \cdot (p\boldsymbol{u})\mathcal{G}(|\boldsymbol{x}-\boldsymbol{y}|)\ \mathrm{d}\boldsymbol{y} = \nabla \cdot (\alpha \overline{p\boldsymbol{u}}) - \sum_{i=1}^{N_p} \int_{\mathcal{S}_i} \boldsymbol{n} \cdot (p\boldsymbol{u})\mathcal{G}(|\boldsymbol{x}-\boldsymbol{y}|)\ \mathrm{d}\boldsymbol{y}. \tag{2.22}$$

In this expression, $\overline{p\boldsymbol{u}}$ contains the product between sub-filtered pressure and velocity

fluctuations, which will be combined with additional sub-filtered terms to form $\boldsymbol{R}_{Tu}$ later. Similarly, volume filtering the work due to viscous stresses in (2.3) yields

$$-\int_{\mathcal{V}_f} \nabla\cdot(\boldsymbol{u}\cdot\boldsymbol{\tau})\mathcal{G}(|\boldsymbol{x}-\boldsymbol{y}|)\ \mathrm{d}\boldsymbol{y} = -\nabla\cdot(\alpha\widetilde{\boldsymbol{u}}\cdot\overline{\boldsymbol{\tau}}) - \nabla\cdot(\alpha\boldsymbol{R}_{\tau u}) + \sum_{i=1}^{N_p}\int_{\mathcal{S}_i}\boldsymbol{n}\cdot(\boldsymbol{u}\cdot\boldsymbol{\tau})\mathcal{G}(|\boldsymbol{x}-\boldsymbol{y}|)\ \mathrm{d}\boldsymbol{y}, \tag{2.23}$$

where $\boldsymbol{R}_{\tau u} = \overline{\boldsymbol{u}\cdot\boldsymbol{\tau}} - \widetilde{\boldsymbol{u}}\cdot\overline{\boldsymbol{\tau}}$, which is unclosed and represents work due to the sub-filtered viscous stress.

We emphasize here that the surface contributions on the right-hand side of Eqs. (2.22) and (2.23) must be treated with care. Unlike in the momentum equation, the presence of the gas-phase velocity in the sub-filtered stresses results in additional cross-terms when decomposing the variables. These cross-terms can be treated in a variety of ways, and the choice will have a direct consequence on how the unclosed terms should be interpreted. Focusing on the pressure work term $\sum_i\int_{\mathcal{S}_i}\boldsymbol{n}\cdot(p\boldsymbol{u})\mathcal{G}(|\boldsymbol{x}-\boldsymbol{y}|)\,d\boldsymbol{y}$, we highlight two approaches that can be taken:

1. Enforcing a no-slip condition at the particle surface, the fluid-phase velocity can be decomposed into $\boldsymbol{u}\big|_{\mathcal{S}_i} = \boldsymbol{v}_p^{(i)} + \dot{r}_p^{(i)}\boldsymbol{n}$, where $\boldsymbol{v}_p^{(i)}$ is the velocity of particle 'i' and $\dot{r}_p^{(i)}$ is the rate of change of its radius. Decomposing pressure into its filtered and sub-filtered contributions, and assuming the particles are rigid and incompressible (i.e., $\dot{r}_p = 0$), the last term on the right-hand side of (2.22) becomes

$$-\sum_{i=1}^{N_p}\int_{\mathcal{S}_i}\boldsymbol{n}\cdot(p\boldsymbol{u})\mathcal{G}(|\boldsymbol{x}-\boldsymbol{y}|)\ \mathrm{d}\boldsymbol{y} = -\overline{p}\sum_{i=1}^{N_p}\int_{\mathcal{S}_i}\boldsymbol{n}\cdot\boldsymbol{v}_p^{(i)}\mathcal{G}(|\boldsymbol{x}-\boldsymbol{y}|)\ \mathrm{d}\boldsymbol{y} - \sum_{i=1}^{N_p}\int_{\mathcal{S}_i}\boldsymbol{n}\cdot\left(p'\boldsymbol{v}_p^{(i)}\right)\mathcal{G}(|\boldsymbol{x}-\boldsymbol{y}|)\ \mathrm{d}\boldsymbol{y}. \tag{2.24}$$

Applying Leibniz rule on the first term on the right-hand side of Eq. (2.24) and recognizing that $\boldsymbol{v}_p$ is uniform across the volume of each particle, Eq. (2.24) can be rewritten as

$$\begin{aligned} -\sum_{i=1}^{N_p} \int_{\mathcal{S}_i} \boldsymbol{n} \cdot (p\boldsymbol{u}) \mathcal{G}(|\boldsymbol{x}-\boldsymbol{y}|) \ \mathrm{d}\boldsymbol{y} &= \overline{p} \nabla \cdot (\alpha_p \boldsymbol{u}_p) \\ &\quad - \sum_{i=1}^{N_p} \boldsymbol{v}_p^{(i)} \cdot \int_{\mathcal{S}_i} p' \boldsymbol{n} \mathcal{G}(|\boldsymbol{x}-\boldsymbol{y}|) \ \mathrm{d}\boldsymbol{y}, \end{aligned} \tag{2.25}$$

where $\boldsymbol{u}_p$ is a filtered (Eulerian) representation of the particle-phase velocity that can be obtained via

$$\alpha_p \boldsymbol{u}_p = \sum_{i=1}^{N_p} \boldsymbol{v}_p^{(i)} \mathcal{G}\big(|\boldsymbol{x} - \boldsymbol{x}_p^{(i)}|\big) \, \mathcal{V}_p^{(i)}. \tag{2.26}$$

As discussed by Houim and Oran [85], assuming constant particle density the disperse phase continuity equation can be employed to yield

$$\overline{p} \nabla \cdot (\alpha_p \boldsymbol{u}_p) = -\overline{p} \frac{\partial \alpha_p}{\partial t} = \overline{p} \frac{\partial \alpha}{\partial t}, \tag{2.27}$$

where $\overline{p} \partial \alpha / \partial t$ represents a pDV work term due to particles entering or leaving a control volume. While the first term on the right-hand side of Eq. (2.25) and the expression above are equivalent, expressing this in terms of volume fraction gradients, as is done in Eq. (2.25), may be more convenient numerically. It is interesting to note that Houim and Oran [85] arrived at this term via a control volume analysis, in which an 'interfacial pressure' was used at the particle surface and for closure assumed this to be equal to the local gas-phase pressure. Meanwhile, the pDV work term naturally appears through volume filtering, and we show that the pressure used is indeed the local gas-phase pressure.

A similar approach can be applied to the viscous work term, which yields

$$\int_{\mathcal{V}} \nabla \cdot (\boldsymbol{u} \cdot \boldsymbol{\tau}) \mathcal{G}(|\boldsymbol{x} - \boldsymbol{y}|) \ \mathrm{d}\boldsymbol{y} = \nabla \cdot (\alpha \widetilde{\boldsymbol{u}} \cdot \overline{\boldsymbol{\tau}}) + \nabla \cdot (\alpha \boldsymbol{R}_{\tau u}) + \overline{\boldsymbol{\tau}} : \nabla (\alpha_p \boldsymbol{u}_p) - \sum_{i=1}^{N_p} \int_{\mathcal{S}_i} \boldsymbol{n} \cdot \left(\boldsymbol{v}_p^{(i)} \cdot \boldsymbol{\tau}' \right) \mathcal{G}(|\boldsymbol{x} - \boldsymbol{y}|) \ \mathrm{d}\boldsymbol{y}, \tag{2.28}$$

It is important to note that the last term in Eqs. (2.25) and (2.28) represents the same unclosed term that appeared in Sec. 2.3.3 typically modeled as drag, except multiplied by the particle velocity, which can be rewritten as $\boldsymbol{u}_p \cdot \boldsymbol{\mathcal{F}}$.

2. Alternatively, if the fluid-phase velocity is not replaced by the particle velocity in the last term on the right-hand side of (2.22), pressure and velocity can respectively be split into filtered and sub-filtered components as

$$- \sum_{i=1}^{N_p} \int_{\mathcal{S}_i} \boldsymbol{n} \cdot (p\boldsymbol{u}) \mathcal{G}(|\boldsymbol{x} - \boldsymbol{y}|) \ \mathrm{d}\boldsymbol{y} = - \sum_{i=1}^{N_p} \int_{\mathcal{S}_i} \boldsymbol{n} \cdot (\overline{p} \ \widetilde{\boldsymbol{u}} + \overline{p}\boldsymbol{u}'' + p'\widetilde{\boldsymbol{u}} + p'\boldsymbol{u}'') \, \mathcal{G}(|\boldsymbol{x} - \boldsymbol{y}|) \ \mathrm{d}\boldsymbol{y}. \tag{2.29}$$

Once again, a similar approach can be applied to the viscous work term. It can immediately be seen that this approach results in different closure terms, none of which resemble $\boldsymbol{\mathcal{F}}$ that appears in Eq. (2.14).

In summary, different choices can be made when volume filtering the pressure and viscous work terms in the energy equation. While both are correct, they require different closure. Here we employ Approach 1 as it leads to fewer unclosed terms.

Applying Approach 1 and filtering the remaining terms yields

$$\begin{aligned}\frac{\partial \alpha\overline{\rho}\widetilde{E}}{\partial t} &+ \nabla\cdot\left(\alpha\overline{\rho}\widetilde{E}\widetilde{\boldsymbol{u}}\right) + \nabla\cdot\left(\alpha(\overline{p}\widetilde{\boldsymbol{u}} - \widetilde{\boldsymbol{u}}\cdot\overline{\boldsymbol{\tau}})\right) + \alpha\nabla\cdot\overline{\boldsymbol{q}} \\ &= -\left(\overline{p}\mathbb{I} - \overline{\boldsymbol{\tau}}\right) : \nabla\left(\alpha_p \boldsymbol{u}_p\right) + \boldsymbol{u}_p\cdot\boldsymbol{\mathcal{F}} + \mathcal{Q} - \nabla\cdot\left(\alpha\{\boldsymbol{R}_{Tu} + \frac{1}{2}\boldsymbol{R}_{uu} - \boldsymbol{R}_{\tau u}\}\right),\end{aligned} \tag{2.30}$$

which leads to a number of unclosed terms that are often neglected, such as the pseudo-turbulent diffusion $\boldsymbol{R}_{uu} = \overline{\rho}\left(\widetilde{\boldsymbol{u}\cdot\boldsymbol{u}\otimes\boldsymbol{u}} - \widetilde{\boldsymbol{u}\cdot\boldsymbol{u}}\otimes\widetilde{\boldsymbol{u}}\right)$, pseudo-turbulent heat flux $\boldsymbol{R}_{Tu} = \overline{\rho}\left(\widetilde{T\boldsymbol{u}} - \widetilde{T}\,\widetilde{\boldsymbol{u}}\right)$, and work due to sub-filtered viscous stresses, $\boldsymbol{R}_{\tau u}$. The work due to momentum exchange is defined as

$$\boldsymbol{u}_p\cdot\boldsymbol{\mathcal{F}} = \sum_{i=1}^{N_p}\boldsymbol{v}_p^{(i)}\cdot\int_{\mathcal{S}_i}\boldsymbol{n}\cdot\left(p'\mathbb{I} - \boldsymbol{\tau}'\right)\mathcal{G}(|\boldsymbol{x}-\boldsymbol{y}|)\ \mathrm{d}\boldsymbol{y}. \tag{2.31}$$

It should be noted that $\widetilde{\boldsymbol{u}}\cdot\boldsymbol{\mathcal{F}}$ is sometimes employed as the work due to drag [126, 254], which was obtained by keeping the fluid velocity at the particle surface instead of decomposing it into $\boldsymbol{u}\big|_{\mathcal{S}_i} = \boldsymbol{v}_p^{(i)} + \dot{r}_p^{(i)}\boldsymbol{n}$. As shown in Approach 2, this procedure introduces additional terms that contain products of filtered and sub-filtered stresses with the fluid velocity, which are not properly accounted for by $\boldsymbol{\mathcal{F}}$. An alternative argument for the proper form of the work due to interphase exchange is presented in Ling et al. [127] where it is shown that $\boldsymbol{u}_p\cdot\boldsymbol{\mathcal{F}}$ must be used due to energy arguments.

2.3.4.1 Filtered equation of state

The filtered equation of state is given by

$$\widetilde{T} = \frac{\gamma\overline{p}}{(\gamma-1)\overline{\rho}}, \tag{2.32}$$

which does not result in any residual contributions if the Favre-filtered temperature is used in the filtered heat flux (2.21). Filtering the thermodynamic relation between

pressure and energy results in

$$\overline{p} = (\gamma - 1)\left(\overline{\rho}\widetilde{E} - \frac{1}{2}\overline{\rho}\widetilde{\boldsymbol{u}}\cdot\widetilde{\boldsymbol{u}} - \overline{\rho}k\right). \tag{2.33}$$

In this expression, $\overline{\rho}k = \mathrm{tr}\left(\boldsymbol{R}_u\right)/2$ where k is the pseudo-turbulent kinetic energy (PTKE). It can immediately be seen that k systematically acts to reduce the local pressure. As a consequence, neglecting this term could lead to underpredictions of the local Mach number. The role of PTKE on local Mach number will be analyzed in Sec. 5.2.5.

2.3.4.2 Transport of PTKE

To help guide model development in later sections, a transport equation is derived for the PTKE. Differentiating $\alpha\overline{\rho}k = \alpha\overline{\rho}\left(\widetilde{\boldsymbol{u}\cdot\boldsymbol{u}} - \widetilde{\boldsymbol{u}}\cdot\widetilde{\boldsymbol{u}}\right)/2$ in time, applying the same filtering procedure from prior sections and rearranging terms yields

$$\begin{aligned}\frac{\partial\alpha\overline{\rho}k}{\partial t} + \nabla\cdot\left(\alpha\overline{\rho}\widetilde{\boldsymbol{u}}k\right) + \frac{1}{2}\nabla\cdot\left(\alpha\boldsymbol{R}_{uu}\right) - \widetilde{\boldsymbol{u}}\cdot\nabla\cdot\left(\alpha\boldsymbol{R}_u\right) = \\ -\left(\overline{p}\mathbb{I} - \overline{\boldsymbol{\tau}}\right):\nabla\left(\alpha\widetilde{\boldsymbol{u}} + \alpha_p\boldsymbol{u}_p\right) + \left(\boldsymbol{u}_p - \widetilde{\boldsymbol{u}}\right)\cdot\boldsymbol{\mathcal{F}} \\ -\nabla\cdot\alpha\left(\boldsymbol{R}_{pu} - \boldsymbol{R}_{\tau u}\right) - \alpha\overline{p\nabla\cdot\boldsymbol{u}} + \alpha\overline{\boldsymbol{\tau}:\nabla\boldsymbol{u}}.\end{aligned} \tag{2.34}$$

In the expression above, the first line represents transport of PTKE. Except for the term containing $\boldsymbol{\mathcal{F}}$, the second line contains terms that are closed, i.e. they are entirely expressed in terms of volume-filtered quantities. The last line contains unclosed (sub-filtered) contributions, such as $\boldsymbol{R}_{pu}$ that involves fluctuations of sub-filtered velocity and pressure, that contributes to pressure diffusion. $\left(\boldsymbol{u}_p - \widetilde{\boldsymbol{u}}\right)\cdot\boldsymbol{\mathcal{F}}$ is a source term that acts to produce PTKE. Note that if k is omitted from the pressure relation (2.33) (as is typically done), the interphase source terms that contribute to PTKE would appear in the transport equation for the gas-phase pressure (see Buchta et al. [33] for details). A model to close the transported PTKE will be proposed in later sections.

2.4 Filtered particle equations of motion

The equations of motion of a single particle are given by

$$\frac{\mathrm{d}\boldsymbol{x}}{\mathrm{d}t} = \boldsymbol{v}_p \tag{2.35}$$

and

$$m_p \frac{\mathrm{d}\boldsymbol{v}_p}{\mathrm{d}t} = \int_S (-p\mathbb{I} + \boldsymbol{\tau}) \cdot \boldsymbol{n} dS. \tag{2.36}$$

To be consistent with the volume filtering procedure, one can decompose the stress in Eq. (2.36) into filtered and and sub-filtered components. By apply the divergence theorem and assuming that the stress varies very little across volume of a particle we have the following

$$m_p \frac{\mathrm{d}\boldsymbol{v}_p}{\mathrm{d}t} \approx \mathcal{V}_p \nabla \cdot (-\overline{p}\mathbb{I} + \overline{\boldsymbol{\tau}}) + \int_{\mathcal{S}_p} (-p'\mathbb{I} + \boldsymbol{\tau}') \cdot \boldsymbol{n} d\boldsymbol{y}. \tag{2.37}$$

Here, the filtered pressure and viscous stresses contribute to resolved forces on the particle while the fluctuating portions contribute to all other forces and require modeling. It is typically assumed sub-filtered contributions will include both steady and unsteady contributions including drag, added mass, Basset effects, etc. While the names of these contributions are synonymously used for incompressible and compressible flows, the physics and contributions of steady and unsteady forces is still a topic open for debate.

2.5 A summary of unclosed terms

The volume filtered conservation equations lead to a number of sub-filtered terms and the so-called "closure problem". In summary, the unclosed terms can be grouped into residual stresses $\boldsymbol{R}_u$ in Eqs. (2.14) and (2.33), $\boldsymbol{R}_\mu$ in Eq. (2.15), $\boldsymbol{R}_{Tu}$, $\boldsymbol{R}_{uu}$, $\boldsymbol{R}_{\tau u}$,

and $\boldsymbol{R}_q$ in Eq. (2.30), and $\boldsymbol{R}_{pu}$ in Eq. (2.34). In addition, a number of sub-filtered surface contributions appear in the form of interphase exchange terms, including the interphase exchange of momentum, $\boldsymbol{\mathcal{F}}$, in Eq. (2.14), as well as work due to momentum exchange, $\boldsymbol{u}_p \cdot \boldsymbol{\mathcal{F}}$, and heat exchange, $\mathcal{Q}$, in Eq. (2.30). Closure models have been proposed for some of these terms, such as drag (e.g., [69, 232, 177] to name a few) and heat exchange [72, 234], but for most part are only valid in the incompressible limit and therefore are likely not applicable to the current study. It is important to note that the unclosed stresses are analogous to those that appear in single-phase large-eddy simulations (LES), but physically represent substantially different effects.

In general the filtering operation commutes as long as the filtering kernel is homogeneous and independent of the coordinate system. In the presence of solid surfaces, the filtering operation does not commute and therefore unresolved contributions arise that must be modeled directly. This can be seen from the form of terms like $\boldsymbol{R}_u$ in (2.17) which implies that the influence of small scale structures is essentially unrecoverable from knowledge of larger scale motion. In both the present volume-filtered formulation and in LES, large scale structures are resolved while small scale structures require models. That being said, the classification "LES" should not be used lightly as it traditionally applies to cases where there exists an energy cascade. Moreover, these terms can be non-negligible even in laminar flows (e.g., via steady wakes), and thus the use of single-phase closure for the terms summarized above should be done with utmost care. The relative contribution of these unclosed terms will be evaluated in later sections using DNS.

CHAPTER III

Assessment of the Compressible Eulerian–Lagrangian Method

3.1 Introduction

Here the equations of motion for particle-laden compressible flows are evaluated in the absence of unclosed fluid phase terms. As previously mentioned, models for the unclosed terms highlighted in conservation of momentum, conservation of energy and the equation of state, see Section 2.5, do not exist for high speed, compressible flows. To evaluate the equations, an Eulerian–Lagrangian method is used where the fluid phase is solved on an Eulerian grid while particles are individually tracked in a Lagrangian manner. Such an approach has been shown to accurately capture two-way coupled fluid-particle flows up to $O(10^8)$ particles with regards to incompressible flows [36]. The method for individual particle tracking and two-way coupling, described in Capecelatro and Desjardins [34] for incompressible flows, is extended for compressible flows. A suite of test cases for method assessment and validation are performed.

3.1.1 Fluid-phase description

For testing purposes, all unclosed fluid phase terms highlighted in Section 2.5 are dropped and filtered term notation is removed for clarity. This leads to the following equations of motion

$$\frac{\partial \alpha\rho}{\partial t} + \nabla \cdot (\alpha\rho \boldsymbol{u}) = 0, \tag{3.1}$$

$$\frac{\partial \alpha\rho \boldsymbol{u}}{\partial t} + \nabla \cdot (\alpha\rho \boldsymbol{u} \otimes \boldsymbol{u}) = \alpha\nabla \cdot (\boldsymbol{\tau} - p\mathbb{I}) + \boldsymbol{\mathcal{F}}, \tag{3.2}$$

$$\frac{\partial \alpha\rho E}{\partial t} + \nabla\cdot(\alpha \boldsymbol{u} \left\{\rho E + p\right\} - \alpha \boldsymbol{u} \cdot \boldsymbol{\tau}) = -\alpha\nabla\cdot\boldsymbol{q} - (p\mathbb{I} - \boldsymbol{\tau}) : \nabla (\alpha_p \boldsymbol{u}_p) + \boldsymbol{u}_p\cdot\boldsymbol{\mathcal{F}} + \mathcal{Q} \tag{3.3}$$

and equation of state,

$$T = \frac{\gamma p}{(\gamma - 1)\rho} \quad \text{and} \quad p = (\gamma - 1)\left(\rho E - \frac{1}{2}\rho \boldsymbol{u} \cdot \boldsymbol{u}\right). \tag{3.4}$$

3.1.2 Particle-phase description

The displacement of an individual particle 'i' is given by

$$\frac{\mathrm{d}\boldsymbol{x}_p^{(i)}}{\mathrm{d}t} = \boldsymbol{v}_p^{(i)}, \tag{3.5}$$

where $\boldsymbol{x}_p^{(i)}$ is the position and $\boldsymbol{v}_p^{(i)}$ is the velocity of the i-th particle. The evolution of particle velocity of the can be expressed as

$$m_p \frac{\mathrm{d}\boldsymbol{v}_p^{(i)}}{\mathrm{d}t} = \mathcal{V}_p \nabla \cdot (-p\mathbb{I} + \boldsymbol{\tau}) + \boldsymbol{f}_{\text{drag}}^{(i)} + \boldsymbol{f}_{\text{col}}^{(i)}, \tag{3.6}$$

where $m_p = \pi\rho_p d_p^3/6$ is the particle mass and the unresolved portion, $\boldsymbol{f}_{\text{drag}}^{(i)}$, is typically modeled using a drag correlation. Other unresolved gas-particle interactions (e.g., Basset, lift, etc.) would appear here. In this work, $\boldsymbol{f}_{\text{drag}}^{(i)}$ is given by

$$\frac{\boldsymbol{f}_{\text{drag}}^{(i)}}{m_p} = \frac{3}{4}\frac{\rho}{\rho_p} C_D \frac{\alpha|\boldsymbol{u} - \boldsymbol{v}_p^{(i)}|}{d_p}\left(\boldsymbol{u} - \boldsymbol{v}_p^{(i)}\right) \tag{3.7}$$

where C_D the coefficient of drag. The term, $\boldsymbol{f}_{\text{col}}^{(i)}$, accounts for collisions between particles and is captured using the soft sphere model originally proposed by Cundall and Strack [47] which was modified to account for high-speed collisions in a robust manner in Capecelatro and Desjardins [34]. Here, the particle equations are non-dimensionalized using the same reference quantities used in Eqs. (2.1)–(6.4).

The evolution of particle temperature is given by

$$m_p C_{p,p} \frac{\mathrm{d}T_p^{(i)}}{\mathrm{d}t} = \mathcal{V}_p \nabla \cdot \boldsymbol{q} + \boldsymbol{q}_{\text{inter}}^{(i)}, \tag{3.8}$$

where $T_p^{(i)}$ is the temperature of the i-th particle and $C_{p,p}$ is the ratio of particle-to-fluid heat capacity. The sub-filtered heat flux, $\boldsymbol{q}_{\text{inter}}^{(i)}$, is given by

$$\frac{\boldsymbol{q}_{\text{inter}}^{(i)}}{m_p} = \frac{\text{Nu}}{3\tau_p \text{Pr}}(T - T_p^{(i)}), \tag{3.9}$$

where Nu is the Nusselt number modeled using the correlation of Gunn [72].

3.2 Discretization

Spatial derivatives are approximated using narrow-stencil finite difference operators D_i that satisfy the summation-by-parts (SBP) property [220]

$$PD + (PD)^{\mathsf{T}} = \text{diag}\left[-1,\ 0,\ \ldots,\ 0,\ 1\right]^{\mathsf{T}}, \tag{3.10}$$

where P is a symmetric positive-definite matrix and $D \in \mathbb{R}^{N \times N}$. In three dimensions, the finite-difference operator can be represented using the Kronecker product

$$\begin{aligned} D_1 &= D \otimes \mathbb{I}_N \otimes \mathbb{I}_N \\ D_2 &= \mathbb{I}_N \otimes D \otimes \mathbb{I}_N \\ D_3 &= \mathbb{I}_N \otimes \mathbb{I}_N \otimes D, \end{aligned} \tag{3.11}$$

where $\mathbb{I}_N$ is the $N \times N$ identity matrix. In this work, we consider a diagonal norm P in order to preserve the SBP property under a coordinate transformation for arbitrary order of accuracy [225]. This leads to $2s$-order centered-difference stencils at interior points and s-order accurate biased stencils near boundaries, with $s+1$ global accuracy. The majority of cases presented herein use the sixth-order interior formulation ($s = 3$) unless otherwise specified. To evaluate second and mixed derivatives, first derivative operators are applied consecutively, necessitating the use of artificial dissipation to damp the highest wavenumber components supported by the grid. High-order accurate SBP dissipation operators are used that provide artificial viscosity based on a $2s$-order derivative [140, 247].

The SBP scheme is combined with the simultaneous approximation treatment (SAT) at the domain boundaries to facilitate an energy estimate [38, 169]. This is achieved by enforcing the desired boundary conditions weakly by adding a penalty term to the right-hand-side of the governing equations. Non-reflecting characteristic boundary conditions and no-penetration free-slip walls are considered in the problems presented in this work via [227, 226]

$$\frac{\partial \boldsymbol{Q}}{\partial t} = R(\boldsymbol{Q}) + \sigma^I P^{-1} E_1 A^+ \left(\boldsymbol{Q} - \boldsymbol{Q}_b\right), \tag{3.12}$$

where $\boldsymbol{Q} = [\rho,\ \rho\boldsymbol{u},\ \rho E]^\mathsf{T}$ is the vector of conserved variables, $R(\boldsymbol{Q})$ is the right-hand side of the compressible flow equations, and σ^I is an inviscid penalty parameter. Setting $E_1 = [1,\ 0,\ \ldots,\ 0]^\mathsf{T}$ ensures the penalty is only applied at the domain boundary, and A^+ is the Roe matrix that selects the incoming characteristics. Setting $\sigma^I \leq -2$ ensures numerical stability [227, 226, 27]. The boundary data are supplied through a stationary target solution in the vector $\boldsymbol{Q}_b(\boldsymbol{x})$. The specific form used to enforce far-field non-reflecting characteristic boundary conditions and no-penetration free-slip walls are given in Vishnampet Ganapathi Subramanian [247]. In addition, an

absorbing sponge region [60] is applied at the domain boundary to prevent unphysical acoustic reflections by adding a damping term of the form $\Psi(\boldsymbol{x})\left[\boldsymbol{Q}(\boldsymbol{x},t)-\boldsymbol{Q}_b(\boldsymbol{x})\right]$ to the right-hand side of the conservation equations.

The equations are advanced in time using a standard fourth-order Runge–Kutta scheme, resulting in the usual Courant–Friedrichs–Lewy (CFL) restrictions on the simulation time step Δt. The acoustic CFL is given by

$$\mathrm{CFL}_a = \frac{\max\left(|\boldsymbol{u}|+c\right)\Delta t}{\min(\Delta \boldsymbol{x})} \tag{3.13}$$

and the viscous CFL is calculate as

$$\mathrm{CFL}_v = \frac{2N_d\mu\Delta t}{\min(\rho\Delta \boldsymbol{x})^2}, \tag{3.14}$$

where $\Delta\boldsymbol{x}$ is the local grid spacing, $c=\sqrt{\gamma p/\rho}$ is the local sound speed, and N_d is the number of dimensions. The simulation time step is restricted based on the maximum of these two quantities. Because the underlying discretization is purely explicit, the maximum CFL should not exceed unity. The immersed boundary method introduced in the following section is specifically designed to avoid adding any further restrictions on Δt. Unless otherwise specified, all cases are run with a constant CFL=0.5.

3.2.1 Consistent interphase exchange

In order to compute the interphase exchange terms appearing in the gas-phase equations (α, $\boldsymbol{u}_p$, $\boldsymbol{\mathcal{F}}$, and $\mathcal{Q}$) consistent with the volume filtered formulation, the particle data is projected to the mesh using a filter kernel, $\mathcal{G}$, of size δ_f. The interphase exchange terms are given by

$$\alpha = 1-\sum_{i=1}^{N_p}\mathcal{G}\left(|\boldsymbol{x}-\boldsymbol{x}_p^{(i)}|\right)\mathcal{V}_p, \tag{3.15}$$

$$\boldsymbol{\mathcal{F}} = -\sum_{i=1}^{N_p} \mathcal{G}\big(|\boldsymbol{x} - \boldsymbol{x}_p^{(i)}|\big)\, \boldsymbol{f}_{\text{drag}}^{(i)}, \tag{3.16}$$

$$\boldsymbol{u}_p \cdot \boldsymbol{\mathcal{F}} = -\sum_{i=1}^{N_p} \mathcal{G}\big(|\boldsymbol{x} - \boldsymbol{x}_p^{(i)}|\big)\, \boldsymbol{v}_p^{(i)} \cdot \boldsymbol{f}_{\text{drag}}^{(i)}, \tag{3.17}$$

and

$$\mathcal{Q} = -\sum_{i=1}^{N_p} \mathcal{G}\big(|\boldsymbol{x} - \boldsymbol{x}_p^{(i)}|\big)\, \boldsymbol{q}_{\text{inter}}^{(i)}. \tag{3.18}$$

The numerical implementation of Eqs. (3.15)–(3.18) requires special care. Maxey et al. [144] proposed to distribute the interphase coupling terms within a narrow envelope centered on the particle position to provide a local spatial average (or filtering) of the particle data on the mesh. However, a direct solution to this interphase coupling strategy is in general computationally intensive as it requires each particle to loop through a large number of neighboring grid points. More recently, Pepiot and Desjardins [182] proposed to project the particle data to the mesh using a high-order quintic spline kernel with compact support. To avoid excessive cost, the support of the kernel was set to the local grid spacing. However, such an approach will fail to converge under mesh refinement since the kernel support is proportional to the grid spacing. To address these shortcomings, Capecelatro and Desjardins [34] proposed a two step filtering approach that decouples the mesh size from particle diameter ratio in an efficient manner. First, particle data is sent to neighboring grid points via trilinear extrapolation. The solution is then diffused such that the projection resembles a Gaussian with characteristic size of δ_f. To avoid restrictive time step constraints in the diffusion process, the latter step is solved implicitly via approximate factorization with a second order alternating direction implicit (ADI) scheme.

3.2.2 Assessment of the numerical method

To assess the proposed Eulerian–Lagrangian method, the results of a multiphase shock tube are compared to the output of a Riemann solver. This study was set

up to reproduce the two dimensional particle gas mixture case specified introduced by Saito et al. [202]. In these cases, an impinging discontinuity comes into contact with a section of the domain consisting of a gas/particle mixture. For each case, the volume fraction was low enough such that collisions could be neglected. The domain size in the x (streamwise) and y (spanwise) directions are $L_x = 15$ and $L_y = 1$ with 600×40 grid points, respectively. These values were found to closely match the single phase shock tube pressure plots without domain dependence. Particles are initially randomly distributed throughout the right half of the domain with mean particle-phase volume fraction $\alpha_p = 5.172 \times 10^{-4}$. The particle to fluid density ratio is $\rho_p/\rho_f = 2500$, and particle diameter is 10 μm, resulting in 52518 particles for all cases. Although the physics of such dust-gas shock-tube problems are well known, no exact solutions exist that can be used for verification. Instead, the computed results are compared against the reference solution from Saito et al. [202] to assess the numerical methods employed. Figure 3.1(a) shows the pressure profile across the domain and Fig. 3.1(b) shows the density variation for the fluid and particle phases. Overall excellent agreement is observed, which indicates the SAT-SBP discretization is capable of capturing shock dynamics in the dilute regime with weak interphase coupling and no inter-particle collisions.

While overall good agreement is seen against the reference solution, it remains to be seen how such a method can handle particle-shock interactions in the presence of larger particles (i.e., with $\Delta x \approx d_p$). To this end, influence of the interphase filter size δ_f on the flow solution is assessed. To avoid excessively expensive domain sizes, the particle diameter was increased to 644.5 μ m for a domain of size $L_x = 15$ and $L_y = 2$, with 3000×400 grid points for baseline cases, A1 and B1, described in Table 3.1. The particle to fluid density ratio is $\rho_p/\rho_f = 2500$, and particles are randomly distributed throughout the right half of the domain. Four different grid spacings are considered with and without filtering, with an effective particle volume fraction set to be $\alpha_p =$

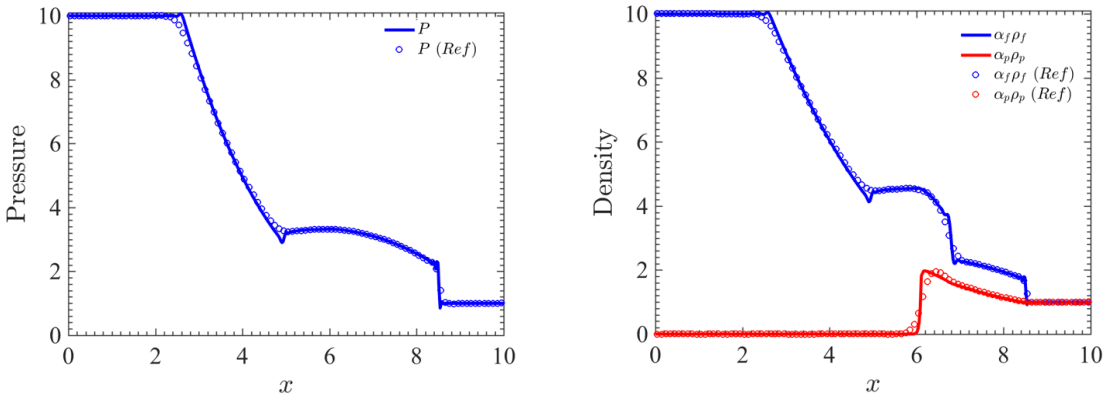

Figure 3.1: (a) Pressure and (b) density profiles of each phase (lines) compared against the reference case from Saito et al. [202] (symbols).

Case	Ly	α	N_p	Δx_i	δ_f
A1	2	5.172×10^{-4}	1264	$4d_p$	$10d_p$
A2	2	5.172×10^{-4}	1264	$2d_p$	$10d_p$
A3	2	5.172×10^{-4}	1264	$1d_p$	$10d_p$
A4	2	5.172×10^{-4}	1264	$0.5d_p$	$10d_p$
B1	2	5.172×10^{-4}	1264	$4d_p$	0
B2	2	5.172×10^{-4}	1264	$2d_p$	0
B3	2	5.172×10^{-4}	1264	$1d_p$	0
B4	2	5.172×10^{-4}	1264	$0.5d_p$	0

Table 3.1: Parameters used in the Riemann problem. A1-A4 is a filtered grid refinement study and B1-B4 is an unfiltered grid refinement study.

5.172×10^{-4}. A complete summary of the parameters used in the multiphase Riemann problem can be found in Table 3.1.

From Fig. 3.2, it can be seen that the filtering operation is necessary when the mesh spacing approaches the particle size. It was found that without the filtering step (i.e., $\delta_f = 0$ and thus interphase exchange is handled via tri-linear extrapolation only), cases B3 and B4 from Table 3.1 lead to unbounded volume fractions causing the solution to diverge. From Figs. 3.2 (a)–(b), the fluctuations in the unfiltered fluid phase appear to grow larger as the mesh is refined, which is not observed when the

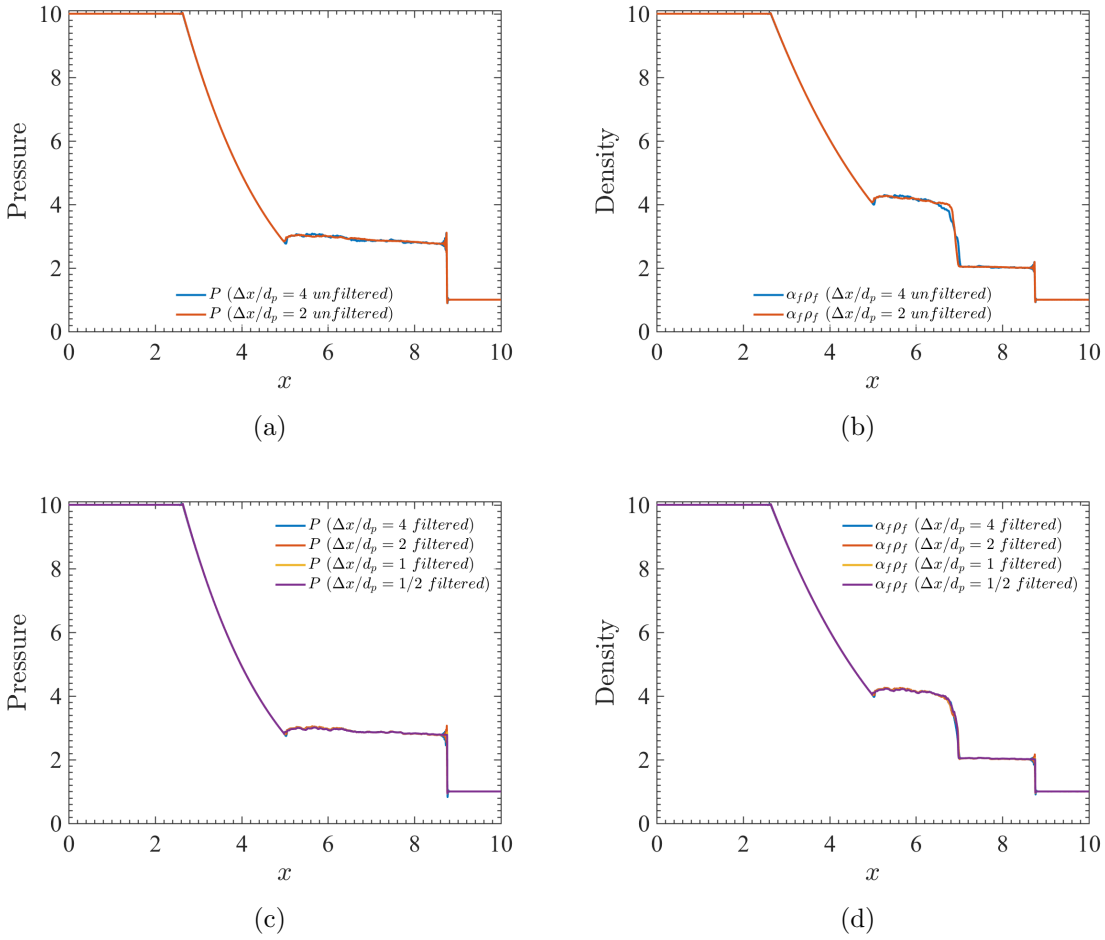

Figure 3.2: (a) Pressure profiles and (b) density profiles of the fluid and particle phases with $\delta_f = 0$ (a)–(b) and $\delta_f = 10d_p$ (c)–(d).

particle filter is used, as seen in Figs. 3.2 (c)–(d).

3.2.3 Two-dimensional shock particle curtain analysis

To assess the validity of the compressible Eulerian-Lagrangian method, a suite of particle-laden shock-tube studies was conducted and compare with experiments described in Ling et al. [126], Wagner et al. [249]. The initial conditions for pre-shock and post-shock values were non-dimensionalized to match a shock mach number of $M_s = 1.66$ while also satisfying the Rankine Hugoniot conditions. For this study, two dimensional simulations were conducted with a domain of $L_x = 100.05$ (streamwise)

and $L_y = 8.28$ with 1742×144 grid points, respectively. The particle-to-fluid density ratio was taken to be that of soda lime glass to air, i.e., $\rho_p/\rho_f = 2520$ with a particle diameter of 100 μm. The number of particles in each case is determined by the effective particle volume fraction, taken to be $\alpha_p = 0.21$ within a particle curtain of non-dimensional thickness of $\delta_c = 1$. For all simulations, monodisperse particles were randomly distributed within the curtain.

Simulations were compared to experimental data for particle spreading rates as well as normalized pressure profiles. Upstream and downstream spreading rates were calculated using the the first percent and 99th percent particle position for the upstream and downstream edges, respectively. The normalized pressure profiles were calculated for the upstream position $x_{up} = 15.7$, denoted by p_1, and downstream position $x_{down} = 82.1$, denoted by p_2, to match the measured data specified by Ling et al. [126]. The effect of domain size, grid spacing ($\Delta x = \Delta y$), interphase filter size (δ_f), coefficient of restitution (e), and collisions are evaluated. A summary of the cases for the numerical shock tube parametric study can be found in Table 3.3.

Starting with the domain size study (D1-D4), there is virtually no variation in the pressure profiles and only minor changes in the particle curtain spreading rate from case to case as shown in Figs. 3.3(a) and 3.3(b) respectively. Similarly with the grid refinement study (E1-E4), there was no significant change in the particle spreading rates and normalized pressure profiles with a finer grid spacing. Due to invariant data observed from case to case, all subsequent studies were conducted with $L_y = 8.28\delta_c$ and $\Delta x_i = d_p$.

Following, the effect of the interphase filter size is analyzed. For case F1, no filter was used for the particle phase. Because the mesh spacing was equal to the particle diameter, local quantities began to diverge in the simulation as seen in the previous study for the multiphase Riemann problem. Alternatively, implementing the filter for all other cases allowed the simulations to rub robustly. Compared to case F2, shown

Case	Ly	α	N_p	Δx_i	δ_f	e	Collisions
D1	4.14 δ_c	0.21	335	d_p	$4d_p$	0.85	On
D2	8.28 δ_c	0.21	669	d_p	$4d_p$	0.85	On
D3	16.56 δ_c	0.21	1338	d_p	$4d_p$	0.85	On
D4	33.12 δ_c	0.21	2676	d_p	$4d_p$	0.85	On
E1	8.28 δ_c	0.21	669	d_p	$4d_p$	0.85	On
E2	8.28 δ_c	0.21	669	$2d_p$	$4d_p$	0.85	On
E3	8.28 δ_c	0.21	669	$4d_p$	$4d_p$	0.85	On
F1	8.28 δ_c	0.21	669	d_p	N/A	0.85	On
F2	8.28 δ_c	0.21	669	d_p	$4d_p$	0.85	On
F3	8.28 δ_c	0.21	669	d_p	$6d_p$	0.85	On
F4	8.28 δ_c	0.21	669	d_p	$8d_p$	0.85	On
G1	8.28 δ_c	0.21	669	d_p	$4d_p$	0.85	Off
G2	8.28 δ_c	0.21	669	$2d_p$	$4d_p$	0.85	Off
H1	8.28 δ_c	0.21	669	d_p	$4d_p$	0.95	On
H2	8.28 δ_c	0.21	669	d_p	$4d_p$	0.75	On
H3	8.28 δ_c	0.21	669	d_p	$4d_p$	0.55	On
H4	8.28 δ_c	0.21	669	d_p	$4d_p$	0.35	On

Table 3.2: Two-dimensional shock tube cases. Where D1-D4 is a domain study for varying Ly, E1-E4 is a grid refinement study, F1-F5 is a an interphase filter study, and G1-G2 is a collisional study.

Case	Ly = Lz	α	Δx_i	δ_f	e	Collisions	Drag Law
I1	4.14 δ_c	0.21	d_p	$4d_p$	0.85	On	Ling [126]
I2	4.14 δ_c	0.21	d_p	$4d_p$	0.85	On	Loth [133]
I3	4.14 δ_c	0.21	d_p	$4d_p$	0.85	On	Theo [238]
I4	4.14 δ_c	0.21	d_p	$4d_p$	0.85	On	Gidaspow [69]
J1	4.14 δ_c	0.21	d_p	$4d_p$	0.85	On	Gidaspow [69]
J2	4.14 δ_c	0.21	d_p	$4d_p$	0.85	Off	Gidaspow [69]

Table 3.3: Three-dimensional shock tube cases. Where I1-I4 is a drag law analysis and J1-J2 is a collisional study. All described include $N_p = 36159$ particles

in Fig. 3.5(b), with an interphase filter of $\delta_f = 4d_p$, there was better agreement with the leading edge particle curtain trajectory for later times. Increasing the interphase particle filter to $\delta_f = 8d_p$ resulted in worse agreement in both the leading edge and trailing edge particle curtain spreading rates for later times. This suggests there is likely a critical filter size that is capable of realistic particle curtain spreading rates in such regimes. In addition, almost no difference in the normalized pressure profiles are observed between cases F2 through F4, as shown in Fig. 3.5(a).

The coefficient of restitution (e) was also varied to assess the influence of particle contact dynamics. For all cases (H1-H4), the normalized pressure profiles remained consistent, as given by Fig. 3.6(a). Increasing the coefficient of restitution to $e = 0.95$, as shown in Fig. 3.6(b), resulted in a worse match of both leading edge and trailing edge particle trajectories. Decreasing the value to $e = 0.55$, as shown in Fig. 3.6(b), led to a close match with the experimental data. However, lowering the coefficient of restitution even further to $e = 0.35$, as shown in Fig. 3.6(b), resulted in an over prediction in the leading edge particle trajectory and an under prediction in the trailing edge particle trajectory.

To determine the effect of collisions, case G1 shown by Figs. 3.7(a) and 3.7(b) without collisions is compare to case F2 for the same conditions with collisions. As can be seen, a better match in the leading edge and trailing edge spreading is seen when collisions are not used. while the normalized pressure profiles were unaffected by the presence of collisions. This observation likely points to cancellation errors in the simulated data. The drag law considered in this study was derived for incompressible flows, and thus Mach number dependencies are not considered. To further assess this, additional drag laws need to be analyzed for such cases.

3.2.4 Three-dimensional shock particle curtain analysis

Conditions for the three-dimensional shock particle curtain analysis resemble those described in the two-dimensional studies. To reiterate, a domain of $L_x = 100.05$ (streamwise) and $L_y \times L_z = 4.14 \times 4.14$ with a grid spacing equal to the particle diameter. The particle-to-fluid density ratio was taken to be that of soda lime glass to air, i.e., $\rho_p/\rho_f = 2520$ with a particle diameter of 100 μm. The number of particles in each case is determined by the effective particle volume fraction, taken to be $\alpha_p = 0.21$ within a particle curtain of non-dimensional thickness of $\delta_c = 1$, resulting in $N_p = 36159$ particles for each simulation considered. Monodisperse particles were randomly distributed within the curtain.

For analysis of drag law on particle curtain spreading, cases (I1-I4), it was found that the implemented drag law heavily influenced particle trajectories. From Fig 3.8(b), the models described in [133] and [238] resulted in large under predictions in the spreading rate of the trailing edge of the particle curtain. In comparison, the models proposed in [126] and [69] resulted in slightly better trailing spreading rates compared to experimental data. This discrepancy is likely due to the volume fraction effects that are included for the Gidaspow and Ling drag models; however, are not present for the Theo and Loth drag models. This also leads to discrepancies in the measured pressure upstream and downstream of the particle curtain, see Fig. 3.8(a). In particular, the absence of a volume fraction dependent drag law leads to delays in the upstream pressure profiles.

During the collisional study (J1-J2), the presence of collisions lead to larger errors when comparing particle curtain spreading behavior, as shown in Fig. 3.9(b). This is consistent with what is observed for two-dimensional shock particle interactions. As mentioned before, this is likely due to cancelation errors associated with particle forcing and unclosed term contributions found in the equations of motion.

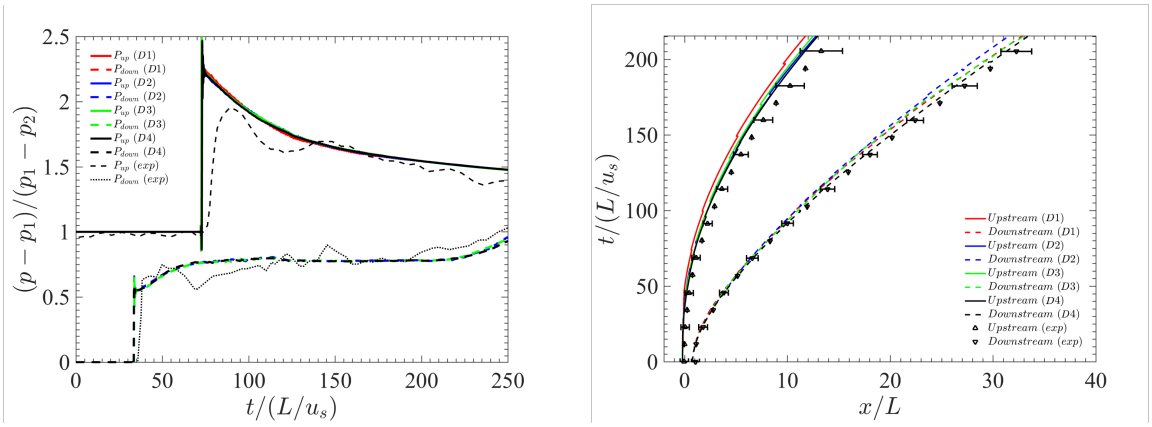

(a) (b)

Figure 3.3: Two-dimensional (a) pressure profiles and (b) particle spreading rates for cases D1-D4.

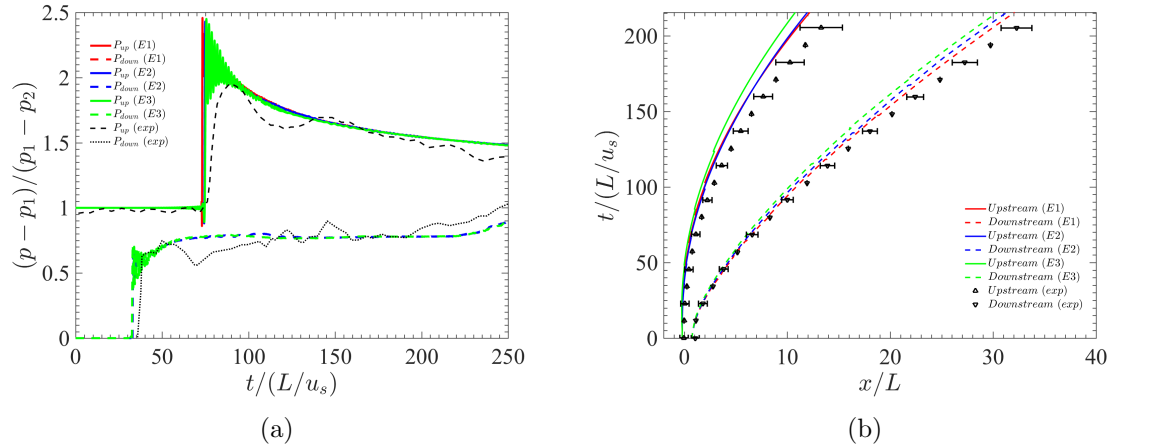

(a) (b)

Figure 3.4: Two-dimensional (a) pressure profiles and (b) particle spreading rates for cases E1-E3.

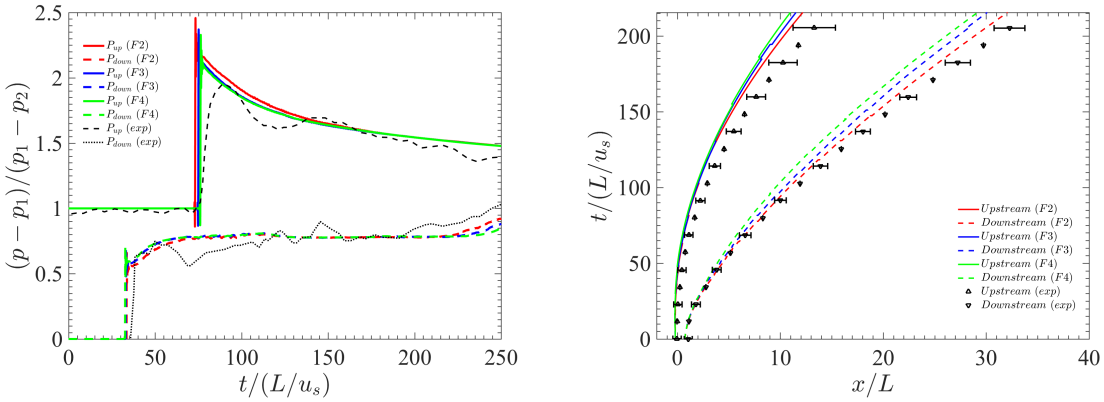

Figure 3.5: Two-dimensional (a) pressure profiles and (b) particle spreading rates for cases F1-F4.

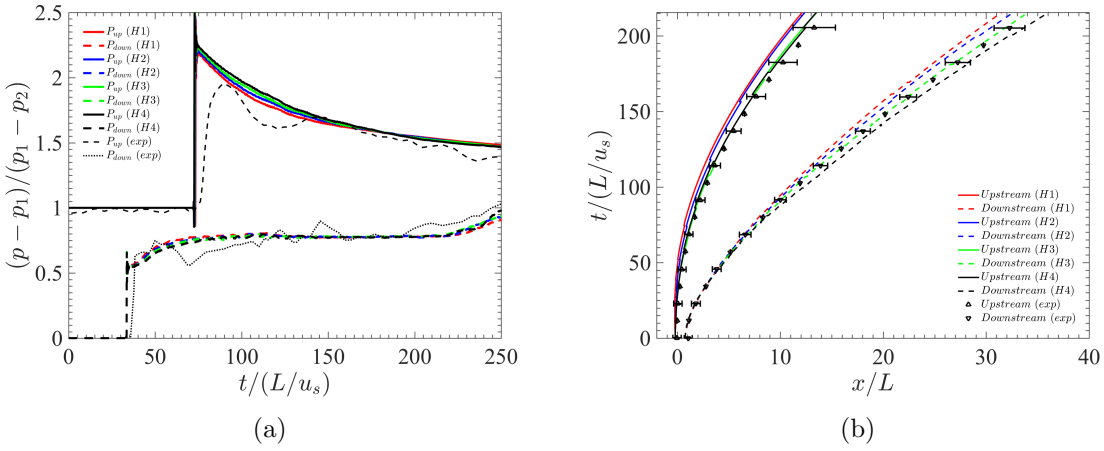

Figure 3.6: Two-dimensional (a) pressure profiles and (b) particle spreading rates for cases H1-H4.

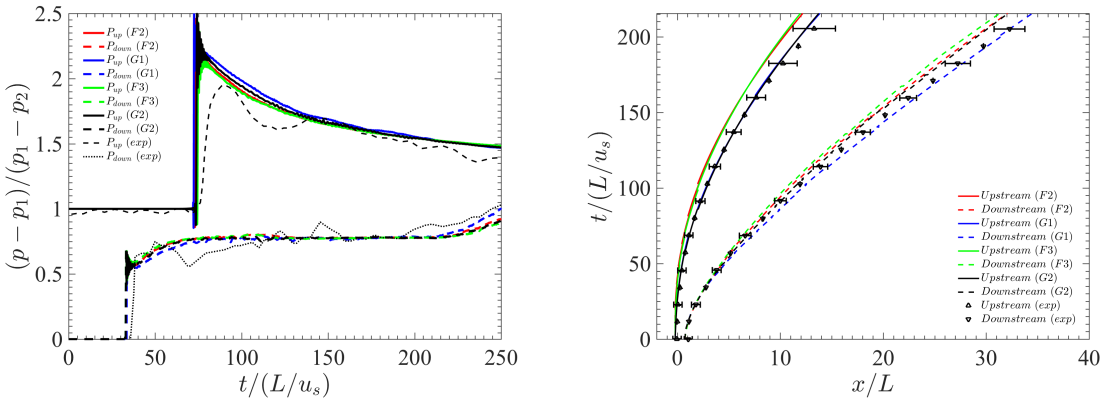

(a) (b)

Figure 3.7: Two-dimensional (a) pressure profiles and (b) particle spreading rates for cases G1-G4.

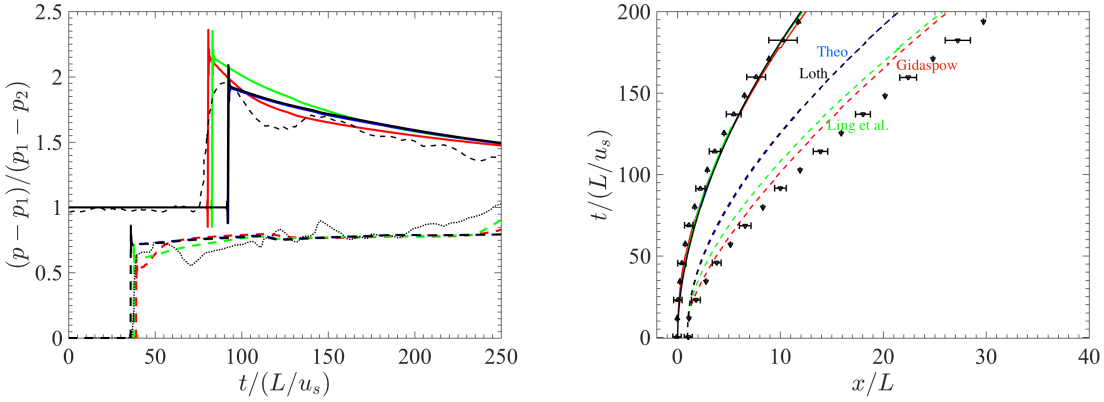

(a) (b)

Figure 3.8: Three-dimensional (a) pressure profiles and (b) particle spreading rates for different drag laws for cases I1-I4.

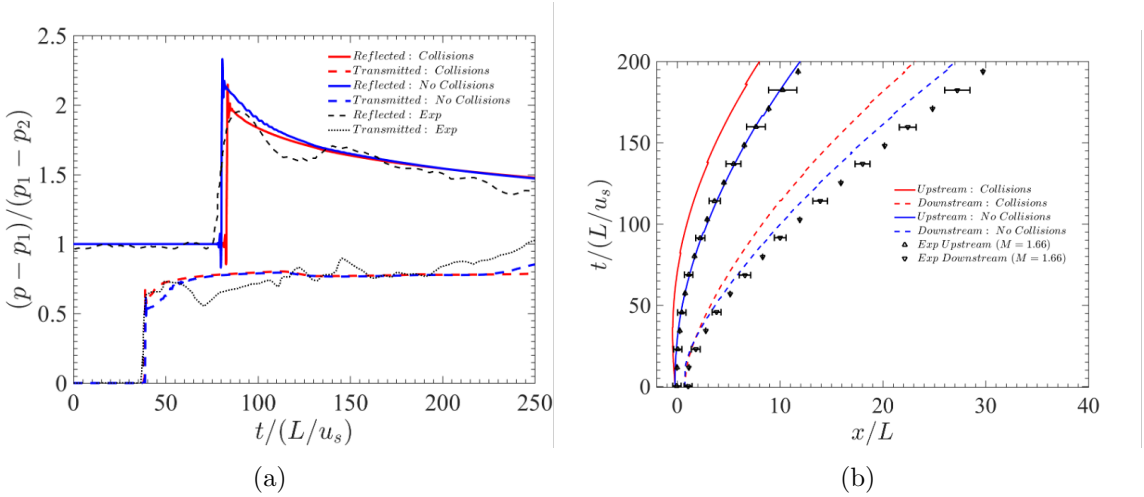

(a) (b)

Figure 3.9: Three-dimensional (a) pressure profiles and (b) particle spreading rates for collisional for cases J1-J2.

3.3 Conclusions

Simulations were conducted using a compressible Eulerian-Lagrangian formulation for particle-laden flows. Comparing results of the proposed discretization to literature for a multiphase Riemann problem showed excellent agreement. A grid refinement study for the multiphase Riemann problem revealed the importance of the interphase filtering operation on the stability of the method as the mesh spacing was refined. The study was then extended to compare against experimental data of particle-laden shock tubes. For two-dimensional shock-particle interactions, it was found that the interphase filter size δ_f and coefficient of restitution e had significant effects on particle phase spreading rates. Results generally agreed with experimental data; however, this was likely due to the cancellation errors and dimensional effects. For three-dimensional shock-particle interactions, it was observed that the implemented drag correlation and presence of particle collisions have a large effect on collected data. Further analysis is necessary to determine the validity of existing drag laws to determine if they bring proper closure to the governing equations presented in this work. While the study demonstrates the capability to capture shock particle interactions

with reasonable accuracy, improved models are clearly required to capture large scale collective motion.

CHAPTER IV

New Immersed Boundary Method for Compressible Flows

4.1 Introduction

In recent years, there has been increased focus towards simulating complex geometries in compressible flows. Body-fitted and unstructured meshes (e.g., [141, 62, 61, 142]) allow for accurate representations of geometric surfaces; however, in practice can be computationally expensive. Non-conforming grid methods, broadly classified herein as immersed boundary methods, are emerging as an attractive alternative. A number of approaches currently exist, such as continuous- and direct-forcing using Lagrangian markers [183, 198, 244, 29], ghost-point and ghost-cell methods [163, 67, 162, 29], and Brinkman/volume penalization methods [7, 106, 245, 131, 31, 84], each with its own benefits and limitations. While immersed boundary methods are well established for incompressible flows (see, e.g., Mittal and Iaccarino [161] and references therein), their extensions to compressible flows are less mature. The purpose of this study is to present a robust immersed boundary method for compressible flow computations that avoids introducing increased stiffness and requires minimal modification to the underlying discretization.

Originally developed for incompressible biological flow applications [183, 198, 184,

161], continuous-forcing involves the addition of a source term which acts to penalize the velocity at an immersed interface. The velocity on the mesh is interpolated to a set of Lagrangian markers distributed along the object's surface and used to create a source term that penalizes the velocity to a desired target value. This source term is then extrapolated to the mesh using a weighted delta function to impose a desired boundary condition on velocity. Since its original development by Peskin [183], numerous modifications and refinements have been proposed, almost entirely focused on incompressible flows. For example, the direct-forcing approach introduced by Mohd-Yusof [163] provides a sharper representation of the interface and alleviates the strict stability limit on the simulation time step by taking into account the underlying discretization. A popular formulation was introduced by Uhlmann [244], which involves the use of a series of discrete delta functions to simulate flow past incompressible, non-deformable objects. The interested reader is referred to Zhou and Balachandar [261] for a recent analysis of the spatio-temporal resolution of direct-forcing immersed boundary methods.

The aforementioned approaches are typically used for imposing conditions on the fluid velocity, and its extension to handling Neumann conditions on scalars must be done with care. Application of Neumann conditions are more straight forward in ghost-point and ghost-cell approaches, which involve communication of information between the interior and exterior of an immersed object on the computational grid without the use of Lagrangian markers [163, 240, 161]. This is accomplished by looping through grid points on the interior of an immersed object, locating corresponding image points normal to its surface and mirroring quantities from the image points to a set of ghost points at the interior to enforce a desired boundary condition. Further details can be found in [67, 162, 29]. Additional modifications need to be taken for objects with thin walls or sharp corners, often involving formulating and implicitly solving a linear system of equations [49, 25]. Recently, direct-forcing was combined

with the ghost-point method as a means to smoothly enforce velocity boundary conditions for compressible flows [29].

Brinkman penalization, first proposed by Arquis and Caltagirone [8], treats the solid as a porous medium with low permeability. Unlike in continuous/direct-forcing approaches and ghost point/cell methods, in this approach the transport equations are penalized within the entire volume of the solid object using pre-defined penalization parameters. Angot et al. [7] showed that the penalized incompressible Navier–Stokes equations converges towards an exact solution as the penalization parameter approaches zero. This method was later extended to viscous compressible flows through the use of non-reflecting boundary conditions [132]. Recently, Brinkman penalization was further modified to account for Neumann and Robin-type boundary conditions in viscous compressible flows through the addition of hyperbolic penalization terms, referred to as characteristic-based volume penalization (CBVP) [31, 84]. Brinkman penalization has also been implemented for inviscid flows [9] and recently extended to CBVP for solution to the Euler equations [32, 119, 120].

Piquet et al. [187] recently performed a detailed comparison of Brinkman penalization (without characteristic treatment for Neumann conditions) and ghost cell methods for viscous transonic and supersonic flows. At sufficient mesh resolution, it was found that both approaches yield qualitatively similar results. For moving objects, the implementation of the ghost cell method is more complex compared to volume penalization and is more computationally expensive as communication between ghost and image points, and corresponding interpolation weights, need to be calculated at every time step. Despite its simplicity, the Brinkman approach was found to suffer from a lack of regularity in the near-wall pressure fluctuations due to the lack of conditions imposed on pressure at the solid interface. However, it was noted in that work that CBVP addresses this issue.

Volume penalization techniques typically rely on a sharp cutoff function, or mask-

ing function, to distinguish between the interior and exterior of an object [32, 187, 119, 120]. This results in a "stair-stepped" interface that can give rise to grid-to-grid oscillations. It is also well established that introducing source terms to penalize the flow to a desired boundary condition in explicit formulations results in a stiff set of equations [241, 70, 201, 131, 187]. To this end, combinations of parameter tuning, sub-iterating at each timestep, and modifications to the computational stencil are common [131, 31, 187, 120].

The aim of this study is to introduce an approach that is simple, i.e., requires minimal modification to the underlying numerical framework, is efficient in the sense it does not introduce additional stiffness beyond the stability limits of the underlying discretization (and thus does not rely on iterative solution procedures) and is robust to sharp discontinuities such as shocks. In the following sections, a parameter-free CBVP method is presented for viscous and inviscid flows within a high-order finite difference framework. The approach is purely explicit where free parameters are chosen based on the limitations of the underlying discretization. A series of verification and validation cases are performed for one-, two-, and three-dimensional steady and unsteady flows, followed by recommendations for general use of the method.

4.2 Purely explicit, characteristic-based volume penalization

With the formulation presented in 2.3 and motivation to study plume-surface interactions, a framework must be established to simulate fluid-solid interactions involving complex geometries. In this section, we briefly review how boundary conditions are enforced using volume penalization for the Navier–Stokes equations and its extension to the Euler equations. The notation from Brown-Dymkoski et al. [31] is adopted for consistency in Secs. 4.4.1–4.4.3. Modifications to the traditional CBVP approach are then proposed to improve efficiency and robustness.

4.3 Signed-distance levelset

A signed-distance levelset function, $\phi(\boldsymbol{x}, t)$, is employed to distinguish the immersed solid from the surrounding fluid. Values outside of the immersed surface are positive while values on the interior are negative. A masking function $\mathcal{X}$ is introduced into the conservation equations to apply appropriate forcing in regions occupied by the immersed object, which can be represented by a Heaviside function according to

$$\mathcal{X}(\phi) = \begin{cases} 1, & \phi < 0 \\ \frac{1}{2}, & \phi = 0 \\ 0, & \phi > 0 \end{cases}. \tag{4.1}$$

In addition to locating the immersed object, the signed distance field provides a simple evaluation of the unit normal direction (outward from the object) $\boldsymbol{n} = \nabla\phi$ and curvature $\kappa = \nabla \cdot \boldsymbol{n}$. Throughout this work, ϕ is determined analytically. For arbitrary shapes, one can use the Lagrangian marker placement strategy obtained from stereolithography (STL) files as described in Boukharfane et al. [29].

4.4 Traditional characteristic-based volume penalization

4.4.1 Dirichlet condition

A Dirichlet condition on velocity is enforced according to

$$\frac{\partial \boldsymbol{u}}{\partial t} = (1 - \mathcal{X})\,\mathrm{RHS}_u - \mathcal{X}\frac{(\boldsymbol{u} - \boldsymbol{u}_o)}{\eta_b}, \tag{4.2}$$

where $\boldsymbol{u}_o$ is the target velocity and η_b is a penalization parameter that controls the rate at which the Dirichlet condition is enforced. This time scale will be discussed in detail in Sec. 4.5. RHS refers all terms excluding the unsteady term in the equation

corresponding to the variable in the subscript. For a no-slip, no-penetration boundary condition the velocity penalty is $\boldsymbol{u}_o = 0$.

4.4.2 Neumann condition

As described in [31], given a transport equation for a general scalar φ,

$$\frac{\partial \varphi}{\partial t} = \underbrace{-\nabla \cdot (\varphi \boldsymbol{u})}_{\mathrm{RHS}_\varphi}, \tag{4.3}$$

a Neumann boundary condition is enforced by propagating information along the interior normal to the surface. Information propagates at a constant characteristic speed proportional to η_c^{-1}, such that

$$\frac{\partial \varphi}{\partial t} = (1 - \mathcal{X})\,\mathrm{RHS}_\varphi + \mathcal{X}\left(\frac{\boldsymbol{n} \cdot \nabla \varphi}{\eta_c} + q_t\right), \tag{4.4}$$

where q_t is the target value for the gradient normal to the surface. The characteristic speed η_c^{-1} represents an additional penalization parameter that must be chosen with care, which will be described in detail in Sec. 4.5.

4.4.3 Free-slip condition

To enforce a free-slip condition, a Robin-type boundary condition is applied to velocity. This requires the application of a Dirichlet condition to penalize the normal component of velocity to zero. The target velocity in Eq. (4.2) is set to the tangential velocity $\boldsymbol{u}_o = \boldsymbol{u}_t = \boldsymbol{u} - (\boldsymbol{u} \cdot \boldsymbol{n})\boldsymbol{n}$.

For a traditional free-slip boundary condition, the tangential force due to viscous stress is zero, i.e., $\boldsymbol{\tau} \cdot \boldsymbol{n} = 0$. Here, a Neumann condition is ensured through the gradient of velocity by enforcing the normal kinetic energy to zero. Following the

procedures described in Secs. 4.4.2 and 4.4.1, the velocity treatment is given as

$$\frac{\partial \boldsymbol{u}}{\partial t} = (1 - \mathcal{X})\,\mathrm{RHS}_u + \mathcal{X}\left(\frac{\boldsymbol{n}\cdot\nabla\boldsymbol{u}}{\eta_c} + q_t - \frac{(\boldsymbol{u}-\boldsymbol{u}_o)}{\eta_b}\right), \tag{4.5}$$

where $q_t = 0$ to remove the normal component of velocity. For inviscid flows, additional modifications are required in the presence of curved surfaces to ensure constant total enthalpy and entropy at the boundary. These modifications will be presented in Sec. 4.8. It should be noted that this approach can easily be applied to other type of Robin boundary conditions, e.g., conjugate heat transfer in which a combination of Dirichlet and Neumann boundary conditions are enforced on temperature.

4.5 Discussion on the penalization parameters

Special care needs to be taken when selecting values for the penalization parameters appearing in Eqs. (4.2)–(4.5). Brown-Dymkoski et al. [31] showed that the leading error terms associated with CBVP are proportional to $\mathcal{O}(\eta_c, \sqrt{\eta_b})$. To keep the velocity penalty dominant over the propagation of scalars, it is suggested that $\eta_b/\eta_c \ll 1$. This constraint avoids excessive phase lag in reflected pulses as scalars are advected past the interface. According to Brown-Dymkoski et al. [31], restrictions on the characteristic time and velocity scales can be determined from a linear asymptotic analysis, revealing that $\eta_b < \eta_c$ and both η_b and η_c must be smaller than unity. Specific values are often chosen based on fine-tuning to specific cases. In Brown-Dymkoski et al. [31], the non-dimensional penalization parameters were given as $\eta_b = \mathcal{O}(10^{-5})$ with $10 \leq 1/\eta_c \leq 100$. Upwinding near immersed boundaries was employed in addition to implicit solvers for improved stability due to increased stiffness that results from these choices in parameters. Similar values for η_b and η_c were used in Hosseinzadeh-Nik et al. [84]. Lavoie et al. [120] found $\eta_b/\eta_c = 10^{-6}$ was adequate to obtain accurate results for subsonic flow around a NACA0012 airfoil and

flow around a high curvature ice horn. Due to increased stiffness associated with the penalization parameters, the system of equations were solved using the biconjugate gradient stabilized (BICGSTAB) algorithm [199] in combination with upwinding near immersed boundaries.

In the present work, we propose to choose these parameters according to the limitations of the underlying discretization. Due to the explicit nature of the discretization presented in Sec. 3.2, the characteristic speed $1/\eta_c$ should not exceed the local sound speed c. To ensure the parameter remains constant, the non-dimensional reference sound speed $c_\infty = \sqrt{\gamma p_\infty/\rho_\infty}$ is used. Based on the non-dimensionalization employed in the current work, $1/\eta_c = c_\infty = 1$. Similarly, the characteristic timescale used to penalize the velocity, η_b, is set to the fastest time permitted by the simulation, i.e., the simulation time step Δt. Considering the CFL restrictions given by Eqs. (3.13) and (3.14), the criterion on the time step is

$$\Delta t < \min\left[\frac{\min(\Delta \boldsymbol{x})}{\max(|\boldsymbol{u}| + c)}, \frac{\min(\rho \Delta \boldsymbol{x}^2)}{\max(2\mu, \lambda)}\right]. \tag{4.6}$$

Generally when satisfying the above relation, $\Delta t \ll 1$, and thus the requirement $\eta_b \ll \eta_c$ is satisfied. With this, the resulting scheme can be solved explicitly without necessitating sufficiently small time steps. Consequently, the error from the penalized boundary conditions is expected to converge as $\mathcal{O}(1, \sqrt{\Delta t})$. Of course, the efficacy of such an explicit formulation remains to be tested. A detailed assessment of the method is reserved for Sec. 4.9.

In addition to the penalization parameters, artificial diffusion is typically added within the immersed object to help obtain continuity of scalars and avoid the creation of discontinuities across the interface. The diffusion coefficient is typically chosen as $\nu_n \propto \Delta x^2/\eta_b$ [31, 32, 84, 120]. Since this nonphysical diffusion contributes to errors in the boundary conditions, the diffusion length scale should be as small as possible

while being sufficiently resolved. Using the fastest timescales supported by the discretization, $\nu_n \leq \min(\Delta \boldsymbol{x})^2/(2N_d\Delta t)$ according to the criterion given by Eq. (3.14). In other formulations [31, 84, 32], diffusion is only added to equations that contain the velocity penalty. We found in the present work that adding diffusion to all conserved variables improves stability for geometries with sharp corners. However, the specific choice of ν_n was found to have little effect on the results reported herein. Experience shows that the diffusion coefficient can be as small as $\nu_n = \min(\Delta \boldsymbol{x})^2/(20N_d\Delta t)$. Unlike previous works that have proposed the use of upwinding schemes and implicit methods for additional stability [31, 120], here no modifications are made to the stencil operators.

4.6 Regularization

In traditional velocity penalization methods, a sharp cutoff, or masking function, $\mathcal{X}$, is used to distinguish between the interior and exterior of the object [7, 106, 57, 187]. Consequently, the solution can be contaminated by grid-to-grid oscillations especially if high-order discretizations are employed. As will be shown in later sections, this can result in high dilatation near the interface that degrades robustness, especially in the presence of strong discontinuities like shock waves.

Motivated by the interface treatment employed in direct-forcing immersed boundary methods [244, 161], we propose a similar regularization that converges to a sharp cutoff in the limit of infinitely small grid spacing. With traditional immersed boundary methods, forcing is applied at the surface of the solid object using a series of mollified (or smoothed) Dirac delta functions. In a similar fashion, we propose to regularize the Heaviside function used for volume penalization such that the forcing smoothly decays from the object interior to the fluid domain over a small number of grid points. A benefit of such an approach over traditional immersed boundary methods is that this can be accomplished entirely on the grid using the levelset func-

tion ϕ instead of relying on Lagrangian marker particles distributed over the object's surface. Thus, the increased cost associated with Lagrangian marker particles, in addition to errors that are introduced due to the choice in the weight and placement of marker particles [56, 244, 259, 102, 261] are avoided.

Adopting a form typically employed in two-fluid formulations [223, 40, 210, 104], the regularized masking function is given by

$$\widetilde{\mathcal{X}} = \begin{cases} 1, & \phi \leq -\epsilon \\ \frac{1}{2} - \frac{\phi}{2\epsilon} - \frac{1}{2\pi} \sin\left(\frac{\phi\pi}{\epsilon}\right), & |\phi| < \epsilon \\ 0, & \phi > \epsilon \end{cases} \tag{4.7}$$

where the regularization parameter ϵ defines its steepness, which is typically chosen between $1 \leq \epsilon/\Delta \leq 3$ [223, 40, 104], where $\Delta = |\Delta \boldsymbol{x} \cdot \boldsymbol{n}|$ is the grid spacing normal to the surface. In the limit that $\epsilon = 0$, this simplifies to the original masking function given by Eq. (4.1). We briefly note that similar regularization of the masking function has been applied to Brinkman penalization for incompressible flows [194]. In order to avoid contamination of the boundary treatment by the fluid equations, we propose to apply $\widetilde{\mathcal{X}}$ only to the volume penalization terms and not to the right-hand side of the original conservation equations (see Fig. 4.1).

4.7 Application to the Navier–Stokes equations

Applying the regularized CBVP approach described heretofore with free parameters chosen based on the limitations of the discretization, the resulting conservation equations for a viscous compressible flow with impenetrable adiabatic boundary conditions can be expressed as

$$\frac{\partial \rho}{\partial t} = (1 - \mathcal{X}) \, \mathrm{RHS}_\rho + \widetilde{\mathcal{X}} \left(c_\infty \boldsymbol{n} \cdot \nabla \rho + \nu_n \nabla^2 \rho \right), \tag{4.8}$$

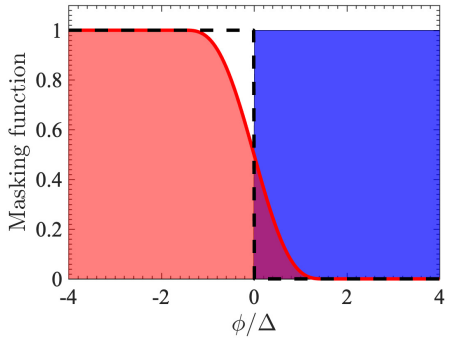

Figure 4.1: Masking function $\mathcal{X}$ typically employed in CBVP (- - -) and the proposed regularized function $\widetilde{\mathcal{X}}$ with $\epsilon = 1.5\Delta$ (—). Region where the fluid equations are solved is highlighted in blue and the region in which the penalized terms are applied is highlighted in red.

$$\frac{\partial \rho \boldsymbol{u}}{\partial t} = (1-\mathcal{X})\,\mathrm{RHS}_{\rho u} + \widetilde{\mathcal{X}}\left(c_\infty \boldsymbol{u}\,(\boldsymbol{n}\cdot\nabla\rho) - \frac{\rho\,(\boldsymbol{u}-\boldsymbol{u}_o)}{\Delta t} + \nu_n \nabla^2\,(\rho\boldsymbol{u})\right), \tag{4.9}$$

and

$$\begin{aligned}\frac{\partial \rho E}{\partial t} =& (1-\mathcal{X})\mathrm{RHS}_{\rho E} \\ &+ \widetilde{\mathcal{X}}\left(\frac{c_\infty}{\gamma}\boldsymbol{n}\cdot\nabla\,(\rho T) + \frac{c_\infty}{2}\,(\boldsymbol{u}\cdot\boldsymbol{u})\,\boldsymbol{n}\cdot\nabla\rho - \frac{\rho\boldsymbol{u}\cdot(\boldsymbol{u}-\boldsymbol{u}_o)}{\Delta t} + \nu_n\nabla^2\,(\rho E)\right),\end{aligned} \tag{4.10}$$

where $c_\infty = 1$ as a result of the non-dimensionalization. It should be noted that in addition to penalization parameters being replaced by the reference sound speed c_∞ and simulation time step Δt, the equations differ slightly from previous formulations [31, 32, 120]. First, due to the hyperbolic nature of the penalized equations, artificial diffusion is added to each of the conserved variables. This is to avoid the need to modify the stencil operators (e.g., use of upwinding [120]). In addition, the energy equation is written in terms of the penalized temperature instead of the total energy and velocity. While both formulations are mathematically consistent, the form employed here requires less memory storage.

4.8 Application to the Euler equations

The absence of viscosity results in the elimination of the viscous boundary layer and thus a free-slip condition on velocity. While it is straight forward to apply a slip velocity condition for flat boundaries (see Sec. 4.4.3), special attention is required for curved surfaces as it is well acknowledged that errors may arise without additional corrections [48, 19, 111, 103, 230, 260, 129].

As discussed in Dadone and Grossman [48], an inviscid flow over a curved boundary must satisfy the normal momentum equation at the wall, i.e., $\partial p/\partial n = -\rho\|\boldsymbol{u}\|^2\kappa$. In the context of volume penalization, this would involve applying a forcing term throughout the immersed solid by rearranging the energy equation in terms of the normal pressure gradient. To ensure constant entropy at the boundary this also involves corrections to both density and the tangential velocity [48, 103, 260, 129]. Curvature corrections are most often implemented based on high order reconstruction of the surface geometry followed by the computation of numerical fluxes into the surface via a Riemann problem at every point along the boundary [19, 111]. While concepts of left and right states for entropy-based corrections are contextually relevant for ghost-point/cell immersed boundary methods, the application to volume penalization methods is less straight forward.

Following Lavoie et al. [120], additional terms are employed to enforce the normal pressure relation, an adiabatic wall condition, constant normal entropy, constant total enthalpy, and a no-penetration wall condition. To determine the curvature correction on density, the normal pressure relation can be recast via the equation of state and enforcing constant entropy, s, [32, 120] which yields

$$\boldsymbol{n}\cdot\nabla s = 0 \rightarrow \boldsymbol{n}\cdot\nabla\rho = -\frac{\rho^2\|\boldsymbol{u}\|^2}{\gamma p}\kappa. \tag{4.11}$$

The penalty on temperature can be found by substituting the equation of state into

Eq. (4.11), giving

$$\frac{\rho}{\gamma p}\boldsymbol{n}\cdot\nabla p=\boldsymbol{n}\cdot\nabla\rho\rightarrow\boldsymbol{n}\cdot\nabla T=-\|\boldsymbol{u}\|^2\kappa. \tag{4.12}$$

Finally, the penalty on velocity is obtained by Eq. (4.11) as well as ensuring constant total enthalpy, $H=(\rho E+p)/\rho$,

$$\boldsymbol{n}\cdot\nabla H=0\rightarrow\boldsymbol{n}\cdot(\boldsymbol{u}\cdot\nabla\boldsymbol{u})=\|\boldsymbol{u}\|^2\kappa. \tag{4.13}$$

As noted in [120], this relation provides a condition on kinetic energy rather than on the velocity. The condition needs be chosen such that Dirichlet and Neumann conditions on velocity are orthogonal. Therefore, the simplest choice is

$$\boldsymbol{n}\cdot\nabla\boldsymbol{u}=\boldsymbol{u}\kappa. \tag{4.14}$$

The penalized equations can be derived by applying the product rule to the unsteady contributions in conservation of mass, momentum, and total energy and applying Eqs. (4.11)–(4.14) on the interior of immersed objects. With this, the regularized volume penalization for the Euler equations are given by

$$\frac{\partial\rho}{\partial t}=(1-\mathcal{X})\,\mathrm{RHS}_\rho+\widetilde{\mathcal{X}}\left(c_\infty\boldsymbol{n}\cdot\nabla\rho+c_\infty\frac{\kappa\rho^2\|\boldsymbol{u}\|^2}{\gamma p}+\nu_n\nabla^2\rho\right), \tag{4.15}$$

$$\begin{aligned}\frac{\partial\rho\boldsymbol{u}}{\partial t}=&(1-\mathcal{X})\,\mathrm{RHS}_{\rho u}\\&+\widetilde{\mathcal{X}}\left(c_\infty\boldsymbol{u}\,(\boldsymbol{n}\cdot\nabla\rho)+c_\infty\rho\boldsymbol{n}\cdot\nabla\boldsymbol{u}-\frac{\rho\,(\boldsymbol{u}\cdot\boldsymbol{n})\,\boldsymbol{n}}{\Delta t}\right.\\&\left.-c_\infty\kappa\rho\boldsymbol{u}\left(1-\frac{\rho\|\boldsymbol{u}\|^2}{\gamma p}\right)+\nu_n\nabla^2\,(\rho\boldsymbol{u})\right),\end{aligned} \tag{4.16}$$

and

$$\begin{aligned}\frac{\partial \rho E}{\partial t} =&(1-\mathcal{X})\mathrm{RHS}_{\rho E} \\ &+\widetilde{\mathcal{X}}\left(\frac{c_\infty}{\gamma}\boldsymbol{n}\cdot\nabla\left(\rho T\right)+\frac{c_\infty}{2}\left(\boldsymbol{u}\cdot\boldsymbol{u}\right)\boldsymbol{n}\cdot\nabla\rho+c_\infty\rho\boldsymbol{u}\cdot\left(\boldsymbol{n}\cdot\nabla\boldsymbol{u}\right)-\frac{\rho\boldsymbol{u}\cdot\left(\boldsymbol{u}\cdot\boldsymbol{n}\right)\boldsymbol{n}}{\Delta t}\right. \\ &\left.-\left(1-\frac{1}{\gamma-1}\right)c_\infty\kappa\rho\|\boldsymbol{u}\|^2+c_\infty\frac{\kappa\rho^2\|\boldsymbol{u}\|^4}{2\gamma p}+\nu_n\nabla^2\left(\rho E\right)\right).\end{aligned} \tag{4.17}$$

In the proposed formulation, curvature corrections are only applied near the surface of immersed object to avoid singularities due to infinite curvature at locations of converging normal vectors. These corrections are applied $8\Delta x$ into the solid, though the specific choice was found to have insignificant effect on the results reported herein. This ensures that curvature corrections are applied in regions within the maximum stencil size for the employed discretization. For geometries with sharp corners, infinite curvature can extend to the surfaces, leading to numerical issues. To this end, κ is taken as the minimum between the local curvature and the maximum resolvable curvature on the grid, i.e., $\kappa = \min(\nabla\cdot\boldsymbol{n}, 1/(2\Delta x))$.

4.9 Results and discussion

4.9.1 Inviscid flows

In this section, the explicit characteristic-based volume penalized introduced in the previous section is assessed for a series of cases of varying complexity. Here we focus on the inviscid formulation summarized in Sec. 4.8, with specific attention paid on the role of resolution, curvature corrections, and the regularization parameter, ϵ.

4.9.1.1 One-dimensional acoustic reflection

In this example, a one dimensional acoustic wave interacts with a wall immersed in an inviscid fluid. The original description of the case can be found in [31]; however,

it has been adapted for this work. Density, momentum, and pressure are initialized to be uniform fields with $\rho_\infty = 1$, $u_\infty = 0$, and $p_\infty = 1/\gamma$. The wave is added as a fluctuation in density, momentum, and pressure according to

$$\rho' = \rho u' = p' = 10^{-3} \left(\frac{(x - 0.4)}{0.2} - 1 \right)^4 \left(\frac{(x - 0.4)}{0.2} + 1 \right)^4, \quad 0.2 < x < 0.6. \quad (4.18)$$

A domain length of $L_x = 1.3$ is considered. The wave propagates downstream and interacts with a wall at $x = 0.65$. A no-penetration Dirichlet condition is applied on velocity. Both the sharp interface treatment ($\epsilon = 0$) and regularized interface ($\epsilon > 0$) are evaluated. Convergence studies are performed for an immersed wall aligned with the grid and a wall offset from the grid. An L_2 error norm of the density is evaluated inside the fluid ($\phi > 0$) at a non-dimensional time of $t = 0.6$ after the wall reflection has occurred. The reference solution is taken to be an advected wave in the absence of the wall using the finest resolution applied to each case. To avoid errors associated with the time integration scheme and isolate errors in the spatial discretization and volume penalization treatment, Δt is held constant for each case such that CFL ≤ 0.1.

The L_2-norm of the acoustic wall interaction is shown in Fig. 4.2. With $\epsilon = 0$, the convergence rate is first order regardless of whether the wall is aligned or offset from the grid. This should be expected with sharp interface volume penalization methods (refer to Sec. 4.5). Better convergence is observed with the regularized surface with $\epsilon = 1.5\Delta$. The error magnitude is also reduced with $\epsilon = 1.5\Delta$ when the grid is offset from the wall. It can be seen that the nature of the error depends on the choice of ϵ. It was found here that values of $1.5 \leq \epsilon \leq 2$ provided minimum error. Further examination of ϵ will be performed in the following sections.

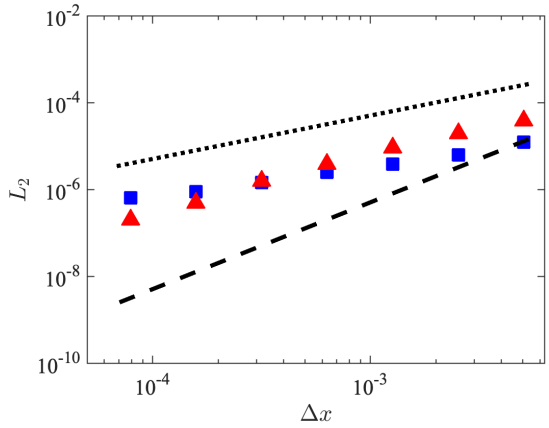

(a) Immersed wall aligned with the grid

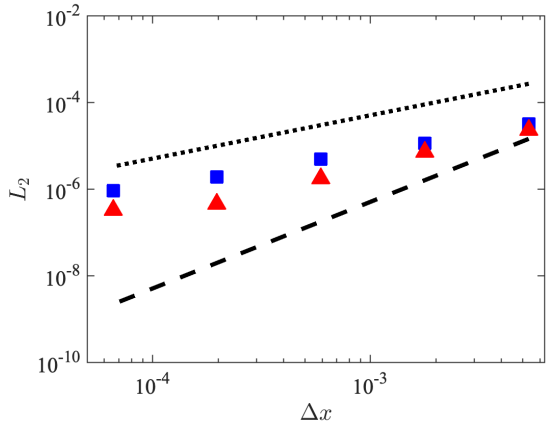

(b) Immersed wall offset with the grid

Figure 4.2: L_2 error norm of an acoustic wave interacting with a vertical wall (a) aligned with the grid and (b) offset from the grid for $\epsilon = 0$ (■) and $\epsilon = 1.5\Delta$ (▲). Lines of convergence are shown for $\mathcal{O}(\Delta x)$ ($\cdots$) and $\mathcal{O}(\Delta x^2)$ (- - -).

4.9.1.2 Inviscid flow past a stationary cylinder

In this test case we aim to assess the efficacy of the proposed volume penalization approach in predicting potential flow around a circular cylinder. This case is particularly useful in identifying the conditions that give rise to unphysical boundary layer separation when viscosity is absent. The fluid is assumed to be incompressible, inviscid, and irrotational such that potential flow theory can be used as a reference case. Under these conditions, the analytic solution for the pressure coefficient at the surface of a circular cylinder is given by [114]

$$C_p(\theta) = 2(p(\theta) - p_\infty)/(\rho_\infty u_\infty^2) = 2\cos(2\theta) - 1, \tag{4.19}$$

where θ is the angular coordinate with the stagnation points located at $\theta = 0$ and π.

The inviscid formulation given by Eqs. (4.15)–(4.17) is employed here. The flow is initialized with a uniform density ρ_∞, pressure p_∞, and velocity u_∞ corresponding to $\mathrm{Ma}_\infty = 0.1$ around a stationary cylinder with diameter D located at the center of the domain. A domain of size $L_x \times L_y = 20D \times 20D$ is considered with uniform grid spacing. Farfield boundary conditions and sponge zones are applied at each domain boundary. Four cases are considered: (i) a no-slip velocity condition with $\epsilon = 0$; (ii) a free-slip velocity condition without curvature correction terms (described in Sec. 4.8) and $\epsilon = 0$; (iii) a free-slip velocity with curvature correction terms and $\epsilon = 0$; and (iv) a free-slip velocity with curvature correction terms and $\epsilon = 1.5\Delta$. For each case, the grid spacing is varied between $20 \leq D/\Delta x \leq 160$.

Contours of the steady state Mach number are shown in Fig. 4.3(b). It can immediately be seen that without proper boundary treatment a wake forms downstream, breaking the expected symmetry of the potential flow solution. This is observed for both the no-slip and free-slip treatment without the curvature corrections described in Sec. 4.8. Symmetry is preserved when curvature corrections are applied for both

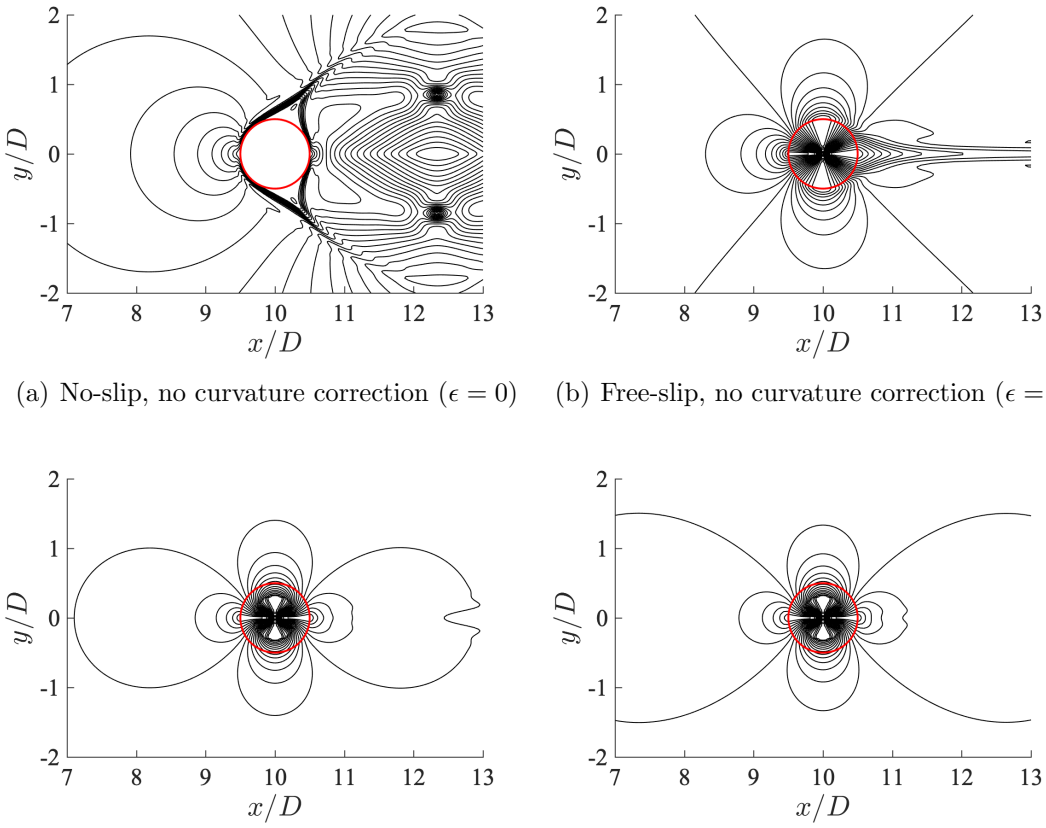

(a) No-slip, no curvature correction ($\epsilon = 0$)

(b) Free-slip, no curvature correction ($\epsilon = 0$)

(c) Free-slip, curvature correction ($\epsilon = 0$)

(d) Free-slip, curvature correction ($\epsilon = 1.5\Delta$)

Figure 4.3: Mach number contours for an inviscid flow past a stationary cylinder (shown in red) with $\Delta x = D/40$. Contour lines are evenly spaced on a scale ranging from 0 to 0.2.

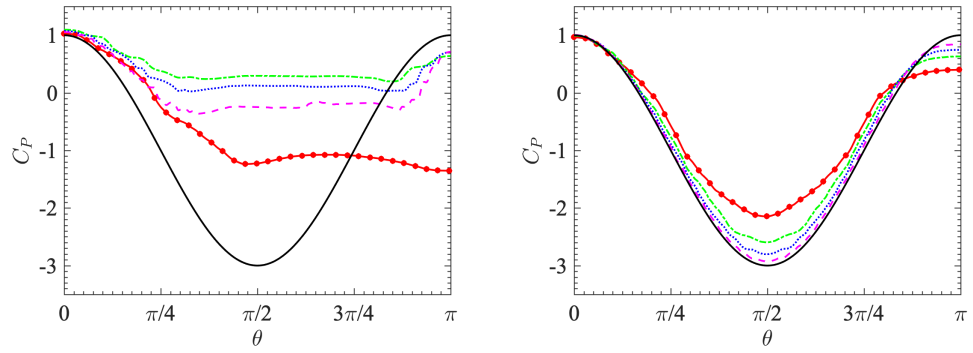

(a) No-slip, no curvature correction ($\epsilon = 0$) (b) Free-slip, no curvature correction ($\epsilon = 0$)

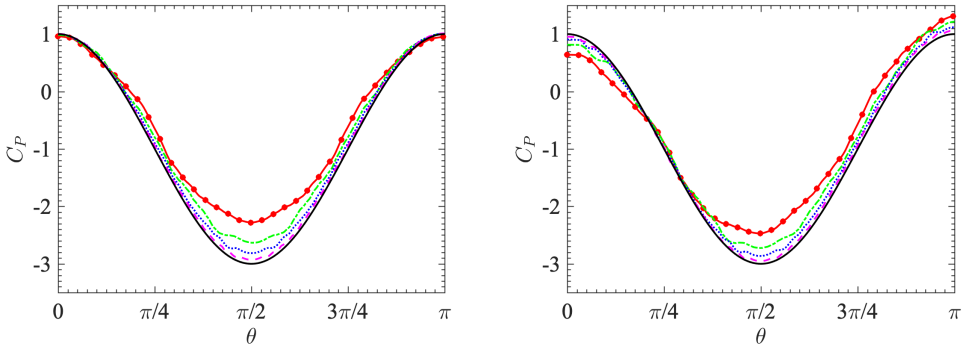

(c) Free-slip, curvature correction ($\epsilon = 0$) (d) Free-slip, curvature correction ($\epsilon = 1.5\Delta$)

Figure 4.4: Surface pressure coefficient for potential flow around a cylinder with $\Delta x = D/20$ (—●—), $\Delta x = D/40$ (- - -), $\Delta x = D/80$ (····), $\Delta x = D/160$ (– –), and the analytic solution (4.19) (——).

the sharp ($\epsilon = 0$) and regularized (with $\epsilon = 1.5\Delta$) treatment. Inspection of the Mach number contours reveals qualitatively similar flow features for these two cases.

Results for the corresponding pressure coefficient and comparison to theory given by Eq. (4.19) can be found in Fig. 4.4. The pressure coefficient is calculated using Eq. (4.19) where the pressure, $p(\theta)$, corresponds to the pressure interpolated to Lagrangian markers distributed along the surface of the cylinder. Further details on the evaluation of surface stresses can be found in Appendix A.1. As was observed in Fig. 4.3, the cases without curvature corrections give rise to a wake, resulting in an under prediction in pressure coefficient at the downstream stagnation point ($\theta = \pi$). Although the slip condition exhibits improvement over the no-slip treatment, both

cases fail to remain symmetric even at the finest resolution under consideration. Inclusion of the curvature correction terms greatly improves symmetry in the pressure coefficient. With $\epsilon = 0$, the flow remains symmetric at all resolutions. The regularized Heaviside treatment with $\epsilon = 1.5\Delta$, shown in Fig. 4.4(d), exhibits larger errors in the coefficient of pressure at the stagnation points, despite no wake observed in the Mach number contours in Fig. 4.3(d). This is a consequence of gradients in the masking function when $\epsilon > 0$, and thus the target solution does not correctly represent a slip velocity condition. Therefore, without sufficiently fine mesh resolutions, the regularized penalization ($\epsilon > 0$) should not be used for steady inviscid flows with curvature under its current form. This will be further examined in subsequent cases.

Mass conservation is assessed by calculating the the mass flow rate through planes located $5D$ upstream and $5D$ downstream from the center of the immersed cylinder. The results were found to be invariant to the choice in the location of the sampling plane. The error in mass conservation is given by $|1 - \dot{m}_1/\dot{m}_2|$, with $\dot{m}_1$ and $\dot{m}_2$ the average mass flow rate located upstream and downstream from the cylinder, respectively. The error was found to vary between 3.2×10^{-4} and 3.4×10^{-4} for the cases with the curvature corrections applied. Thus, error in mass conservation remains relatively low and is found to be insensitive to the grid resolution and choice in regularization parameter.

4.9.1.3 Oscillating cylinder in an inviscid fluid

The configuration described in the previous section is modified to assess the methodology in an unsteady flow by considering a sinusoidally oscillating cylinder. The cylinder is placed in a quiescent flow ($u_\infty = 0$) with uniform pressure and density. The center position of the cylinder is prescribed according to

$$x_c(t) = a \sin\left(2\pi f t - \frac{\pi}{2}\right), \tag{4.20}$$

where the motion amplitude is set to $a = 0.1$ and f is the forcing oscillation frequency. To ensure the Mach number remains small enough such that compressibility is not important, the maximum velocity of the cylinder is set to $\max(u_c) = 0.1$, where $u_c(t) = \mathrm{d}x_c(t)/\mathrm{d}t$. This is enforced by defining $f = 0.1$. In order to account for the motion of the cylinder in the volume penalization, the normal velocity used in Eq. (4.5) is modified according to $(\boldsymbol{u} - \boldsymbol{u}_c) \cdot \boldsymbol{n}$, with $\boldsymbol{u}_c = [u_c, 0, 0]^\mathsf{T}$. It should be noted that the curvature correction terms take into account the non-homogeneous Neumann condition needed on pressure when the object is moving. Finally, in order to avoid contaminating the exterior flow with the artificial scalar fields created inside the solid body, an additional advection term $\boldsymbol{u}_c \cdot \nabla\rho$ is added to the penalized density equation and $\boldsymbol{u}_c \cdot \nabla(\rho T)/\gamma$ to energy [100].

In the limit of incompressible flow, the drag coefficient can be determined analytically [22], given by

$$C_D(t) = 2a\pi^3 \sin\left(2\pi f t - \frac{\pi}{2}\right). \tag{4.21}$$

As pointed out by Belov et al. [22], Liu et al. [130], this case is particularly useful in assessing the performance of a numerical method since an analytic solution is available and no physical dissipation is present, and thus provides a strict test for artificial dissipation introduced by the method and accuracy of the discretization. Furthermore, this case is useful in assessing the role of the regularization parameter in the proposed approach, which was shown to negatively impact the pressure coefficient in the steady flow configuration presented in the previous section.

Figure 4.5 shows the evolution of the drag coefficient with $\Delta x = D/40$ and $\epsilon = 0$, 1.5Δ, and 3Δ. The pressure drag on the surface of the immersed cylinder is determined according to $C_D = -\oint p\boldsymbol{n}\mathrm{d}s/(0.5\rho_\infty \max(u_c)^2 D)$. Details on the evaluation of pressure at the surface of the immersed boundary are provided in Appendix. A.1. The solution quickly converges to the exact solution after just a few time steps. The time evolution of drag coefficient closely match the analytic solution given by Eq. (4.21)

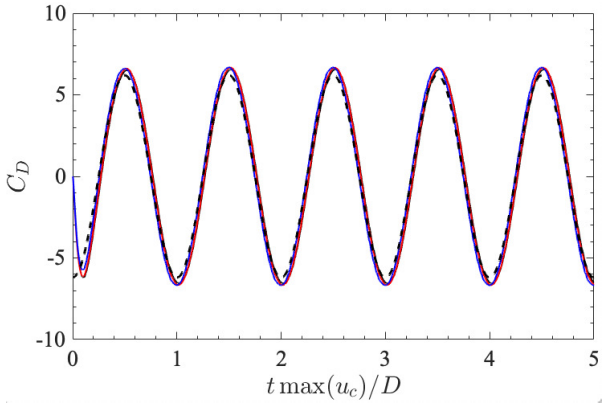

Figure 4.5: Evolution of drag coefficient for an oscillating cylinder in an inviscid fluid with $\Delta x = D/40$ and $\epsilon = 0$ (—), $\epsilon = 1.5\Delta$ (—), $\epsilon = 3\Delta$ (—). Analytic solution given by Eq. (4.21) (- - -).

for each value of ϵ. This demonstrates that unlike with the stationary cylinder that reaches a steady state, the pressure drag is much less sensitive to the regularization parameter when the flow is unsteady. This will be further demonstrated in later sections.

4.9.1.4 Inviscid flow past a wedge

In this case the proposed approach is tested on an inviscid supersonic flow past a wedge. As discussed in [29, 41], oblique shock theory gives rise to the relationship between Mach number Ma_∞, shock wave angle β, and deflection angle θ, given by

$$\tan(\theta) = 2\cot(\beta)\left[\frac{\mathrm{Ma}_\infty^2 \sin^2(\beta) - 1}{\mathrm{Ma}_\infty^2\left(\gamma + \cos(2\beta)\right) + 2}\right]. \tag{4.22}$$

The flow is initialized in a domain of size $L_x \times L_y = 18 \times 12$ with $\mathrm{Ma}_\infty = 2$. A two-dimensional wedge with $\theta = 15°$ and width of $w_t = 2$ is placed $1.75w_t$ downstream from the inlet based on its center position. Uniform grid spacing is chosen such that 100 grid points are distributed across w_t. Farfield boundary conditions and sponge zones are applied at the inflow and outflow and free-slip conditions are employed at the top and bottom of the domain.

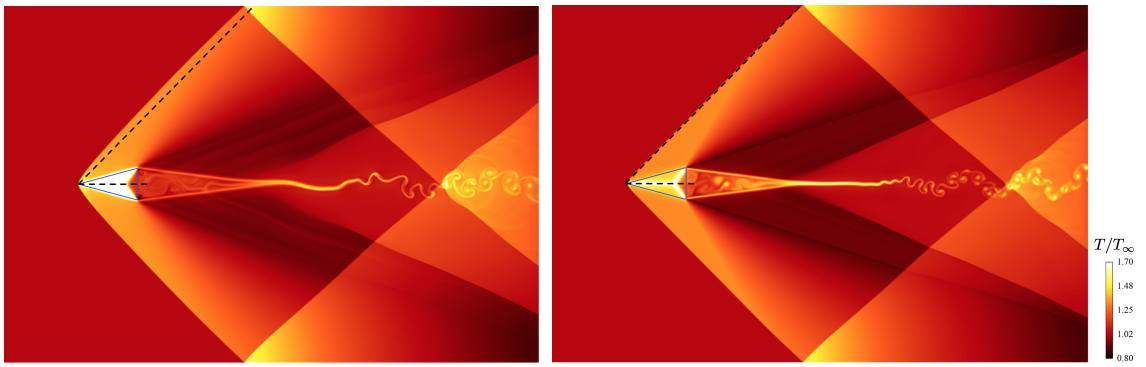

(a) No-slip (b) Slip

Figure 4.6: Instantaneous temperature field for a $\mathrm{Ma}_\infty = 2$ flow past a two-dimensional wedge with $\epsilon = 0$. Theoretical shock wave angle (- - -).

The sharp corners of the wedge can lead to stability issues with the classic CVBP approach due to the advection of information towards intersecting normal vectors. This is addressed here by the application of the regularized Heaviside function and adding localized artificial dissipation in the presence of large discontinuities [45, 136, 26]. Details on the artificial dissipation implementation can be found in [256]. It was found in the present work that using a sharp interface ($\epsilon = 0$) requires a smaller time step due to the generation of large velocity fluctuations. Here, CFL = 0.05 is used for $\epsilon = 0$ while CFL = 0.3 is used for $\epsilon = 1.5\Delta$.

The shock wave angle β is measured by inspection of the resulting temperature field (see Fig. 4.6). According to Eq. (4.22), the shock wave angle for $\mathrm{Ma}_\infty = 2$ and $\theta = 15°$ is $\beta_{theory} = 45.34°$. Both no-slip and slip conditions (with curvature corrections) are considered. Using a free-slip velocity condition with $\epsilon = 0$, the shock wave angle is found to be $\beta_{slip} \approx 45.58°$. The predicted angle is larger when a no-slip condition is employed, yielding $\beta_{no-slip} \approx 48.20°$ (see Fig. 4.6 for a qualitative comparison). Unlike in the steady flow past the stationary cylinder, the regularization does not contaminate the results here due to lack of curvature associated with the wedge surface. With $\epsilon = 1.5\Delta$, the shock wave angle was found to be $\beta_{slip,\epsilon} \approx 45.01°$, which closely matches the theoretical prediction.

4.9.1.5 Inviscid shock past a circular cylinder

In this case, an incident shock wave interacts with a stationary cylinder of diameter D. Post-shock conditions, labeled with a subscript 2, are chosen to satisfy the Rankine-Hugoniot conditions for a shock Mach number $\text{Ma}_s = u_s/c_\infty = 1.3$, where u_s is the shock speed. Pre-shock conditions, labeled with a subscript 1, are given by $(\rho_1,\ u_1,\ P_1 \mid 1.0,\ 0.0,\ 0.714)$. A domain of size $L_x \times L_y = 20D \times 20D$ is considered with the cylinder placed at the center. Farfield conditions with sponge zones are employed at the inflow and outflow boundaries while slip boundary conditions are used at the top and bottom of the domain. Results are compared to data obtained from high-resolution numerical simulations that employ adaptive grid refinement [54, 134] and experimental data from [229]. Note, the experimental data presented in Luo et al. [134] is used herein due to difficulty in obtaining data from [229]. Simulations are assumed to be inviscid and therefore free-slip velocity conditions with curvature corrections are applied to the cylinder. For all cases, a constant time step of $\Delta t = 1\times10^{-3}$ is used to ensure CFL ≤ 0.5.

Results are reported for two resolutions, $\Delta x = D/40$ and $\Delta x = D/80$ with $\epsilon = 0$ and $\epsilon = 1.5\Delta$. The evolution of the coefficient of drag is shown in Fig. 4.7. Convergence in the unsteady drag coefficient towards adaptive grid data reported in [54] is observed for both $\epsilon = 0$ and $\epsilon = 1.5\Delta$. As reported in previous work [228], results are expected to converge towards numerical data instead of the experiment due to uncertainty in experimental measurements associated with the three-dimensional cylinder. Unlike with the potential flow solution in Sec. 4.9.1.3, the regularized Heaviside treatment with $\epsilon = 1.5\Delta$ yields similar results in drag as the sharp interface ($\epsilon = 0$). This is consistent with what was observed with the oscillating cylinder in Sec. 4.9.1.3. This further indicates that the curvature correction terms are not important during the transient period even in the presence of strong discontinuities. Therefore, the added benefits associated with regularization can be exploited for inviscid flows past objects

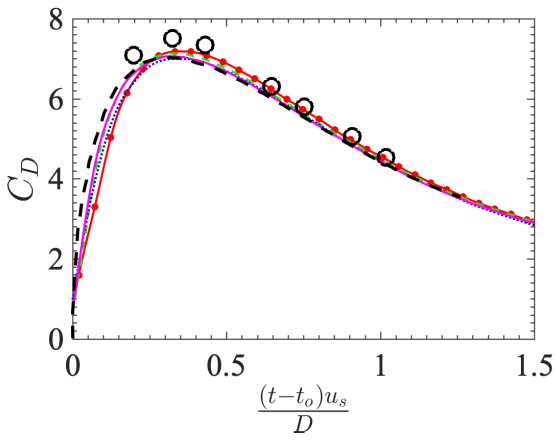

Figure 4.7: Temporal evolution of the coefficient of drag during a shock-cylinder interaction with $\mathrm{Ma}_s = 1.3$. $\Delta x = D/40$ and $\epsilon = 0$ (—●—), $\Delta x = D/80$ and $\epsilon = 0$ (- - -), $\Delta x = D/40$ and $\epsilon = 1.5\Delta$ (····), and $\Delta x = D/80$ and $\epsilon = 1.5\Delta$ (——). Experimental data (○) [229, 134] and numerical data using adaptive grid refinement (▪▪▪) [54, 134]. Here, t_o corresponds to the instant the shock interacts with the cylinder.

with curved surfaces prior to steady state being reached. This will be further justified in the three-dimensional cases reported in later sections.

4.9.1.6 Inviscid shock past a sphere

In this case, an incident shock with Mach number based on the shock speed $\mathrm{Ma}_s = u_s/c_\infty = 1.22$ interacts with a stationary sphere with diameter D in a domain of size $L_x \times L_y \times L_z = 15D \times 15D \times 15D$. The domain is discretized with uniform grid spacing $\Delta x = D/40$. Farfield conditions with sponge zones are applied at the inflow and outflow boundaries of the domain and free-slip conditions are enforced at all other boundaries. The simulations are taken to be inviscid. Results are compared to experimental data with $\mathrm{Re} = 4.9 \times 10^5$ [222].

The temporal evolution of the unsteady drag coefficient is shown in Fig. 4.8 for $\epsilon = 0$ and 1.5Δ. Results from both cases match the experimental data exceptionally well during the initial transient ($t - t_o < 2D/u_s$), with t_o the time at which the shock first interacts with the sphere. At later times, the simulation performed using $\epsilon = 0$

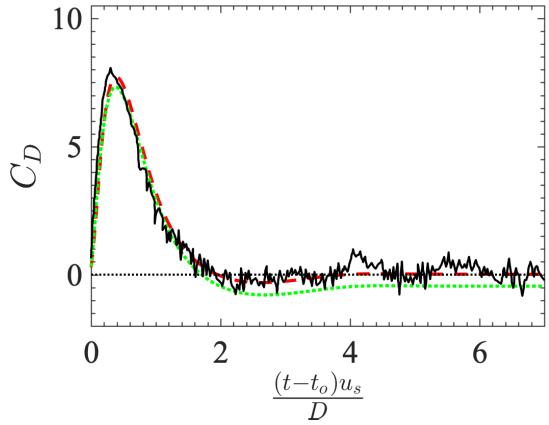

Figure 4.8: Unsteady drag coefficient for a $\mathrm{Ma}_s = 1.22$ shock interacting with a sphere with $\Delta x = D/40$. $\epsilon = 0$ (- - -), $\epsilon = 1.5\Delta$ (····), experimental data [222] (—), and a reference line indicating $C_D = 0$ (·····). Here, $(t - t_o) = 0$ corresponds to the instant the shock begins to interact with the sphere.

correctly predicts a steady drag coefficient that approaches zero. With $\epsilon = 1.5\Delta$, the regularized interface results in negative drag at steady state. This is consistent with what was observed in previous two-dimensional steady inviscid calculations, in which it was found that the curvature correction terms are not properly enforced when $\epsilon > 0$. Consequently, for inviscid flows past objects with curved surfaces, it is recommended that the regularization only be applied for unsteady calculations.

4.9.2 Viscous flows

In this section, the proposed methodology is tested against a suite of cases for two- and three-dimensional viscous flows. The formulation summarized in Sec. 4.7 is used with specific attention paid on the role of resolution and regularization parameter in predicting frictional drag.

4.9.2.1 Viscous subsonic flow past a cylinder

In this case, a background flow is initialized with a subsonic Mach number of $\mathrm{Ma}_\infty = 0.1$ and Reynolds number $\mathrm{Re} = 300$. The flow interacts with a stationary

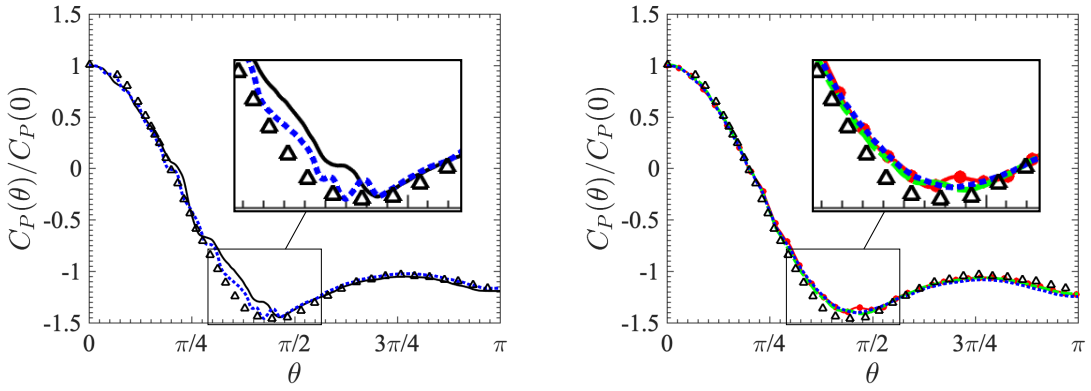

(a) $\epsilon = 0$ (b) $\epsilon > 0$

Figure 4.9: Coefficient of pressure for a steady flow interacting with circular cylinder at $\mathrm{Ma}_\infty = 0.1$ and $\mathrm{Re} = 300$. (a) $\Delta x = D/40$ with $\epsilon = 0$ (—) and $\Delta x = D/80$ with $\epsilon = 0$ (····). (b) $\Delta x = D/40$ with $\epsilon = \Delta$ (—●—), $\epsilon = 1.5\Delta$ (- - -), and $\epsilon = 3\Delta$ (····). Numerical body-fitted data [193] (△).

cylinder of diameter D. A domain of size $L_x \times L_y = 30D \times 10D$ is initialized with the cylinder placed at the centerline at $x = 10$. Farfield conditions with sponge zones are applied at the inflow and outflow boundaries and free-slip conditions are employed at the top and bottom of the domain. Results are compared to body-fitted data presented in Rajani et al. [193], Boukharfane et al. [29].

Simulations are performed using resolutions of $\Delta x = D/40$ and $\Delta x = D/80$. The coefficient of pressure is averaged in time after periodic vortex shedding occurs (see Fig. 4.9). For $\epsilon = 0$, spurious oscillations are observed in the pressure coefficient between $5\pi/18 \leq \theta \leq 5\pi/9$. These errors are still present even when increasing the resolution to $\Delta x = D/80$. Increasing the regularization parameter results in smoother C_p profiles and smaller error. Instantaneous snapshots of the velocity dilatation corresponding to these cases are shown in Fig. 4.10. For $\epsilon = 0$, spurious oscillations can be observed near the surface of the object. These oscillations are removed when increasing the regularization with $\epsilon = 1.5\Delta$.

Results for mean drag coefficient, C_D, root-mean-square (RMS) coefficient of lift, $C_{L,RMS}$, and Strouhal number, Sr, are provided in Table 4.1. With $\epsilon = 0$, over-

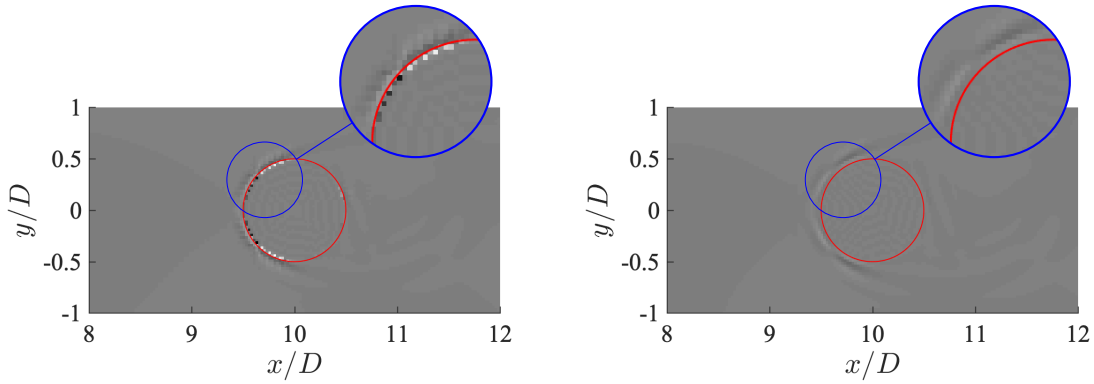

(a) $\epsilon = 0$ (b) $\epsilon = 1.5\Delta$

Figure 4.10: Velocity dilation $(\nabla \cdot \boldsymbol{u})D/u_\infty$ for a viscous subsonic flow past a cylinder with $\Delta x = D/40$ at $(t\,u_\infty)/D = 460$. Dilatation varies between -2.6 (black) and 2.6 (white).

	$\epsilon = 0$	$\epsilon = 0$ ($\Delta x = D/80$)	$\epsilon = \Delta$	$\epsilon = 1.5\Delta$	$\epsilon = 3\Delta$	Rajani et al. [193]
C_D	1.477	1.435	1.419	1.397	1.367	1.367
$C_{L,RMS}$	0.709	0.701	0.705	0.710	0.719	0.602
Sr	0.217	0.217	0.211	0.209	0.200	0.215

Table 4.1: Results for drag coefficient (C_D), RMS coefficient of lift ($C_{L,RMS}$), and Strouhal number (Sr) for subsonic flow past a cylinder with $\Delta x = D/40$, unless otherwise specified, and different values of ϵ.

predictions in the drag coefficient by 8% for $\Delta x = D/40$ and 5% for $\Delta x = D/80$ are observed. Smaller errors are observed when using employing the regularized masking function, with errors remaining below 2% for $\Delta \leq \epsilon \leq 3\Delta$. Regardless of the formulation employed, there are still noticeable over predictions in $C_{L,RMS}$, while good agreement in the Strouhal number compared to body-fitted data is observed.

4.9.2.2 Viscous supersonic flow past a cylinder

The case presented in the previous section is modified such that the background flow is initialized with a uniform Mach number of $\mathrm{Ma}_\infty = 2$ while the Reynolds number is kept at $\mathrm{Re} = 300$. A domain of size $L_x \times L_y = 60D \times 30D$ is considered

with the cylinder placed at the centerline at $x = 20$. As before, the grid resolution is varied between $\Delta x = D/40$ and $D/\Delta x = 80$, and the regularization parameter is varied from $0 \leq \epsilon \leq 3\Delta$. It should be noted that the simulations performed with $\epsilon \leq \Delta$ required the CFL $= 0.3$ due to spurious oscillations at the surface of the cylinder (as was depicted in Fig. 4.10). All other cases are run with CFL $= 0.5$.

Overall good agreement is observed in the surface pressure coefficient with numerical body fitted data from Takahashi et al. [228] (see Fig. 10). However, there are noticeable oscillations in the pressure coefficient at lower resolution that are reduced by increasing ϵ. The resulting drag coefficient C_D, pressure drag $C_{D,p}$, and frictional drag $C_{D,f}$ are reported in Table 4.2. Overall, good agreement is observed in pressure drag for $\epsilon = 0$ and remains relatively unchanged with increasing ϵ. However, noticeable under-predictions in the frictional drag coefficient can be observed. With $\epsilon = 0$, the error in frictional drag decreases with increasing resolution. Meanwhile, the regularization treatment is seen to yield large errors in frictional drag, with $C_{D,f}$ decreasing as ϵ increases. This is not unexpected as the smooth interface treatment reduces velocity gradients at the surface and thus reduces frictional drag. Therefore, while $\epsilon > 0$ helps with stability, it negatively impacts the prediction in frictional drag.

A mass conservation analysis is repeated here for viscous supersonic flow, see Sec. 4.9.1.3 for further details. The mass flow rate upstream of the cylinder is $\dot{m}_1 = 2.00000$ while the downstream value varies between $1.99896 \leq \dot{m}_2 \leq 2.00093$. This yields an error in mass flow rate $|1 - \dot{m}_1/\dot{m}_2| = 4.7 \times 10^{-4}$ and 5.2×10^{-4}. Even for viscous high speed flows, the proposed method exhibits excellent mass conservation properties.

4.9.2.3 Viscous supersonic flow past a sphere

In this final case, a flow is initialized with $\mathrm{Ma}_\infty = 2$ and $\mathrm{Re} = 300$ in a domain of size $L_x \times L_y \times L_z = 80D \times 40D \times 40D$ with a sphere of diameter D placed at the center.

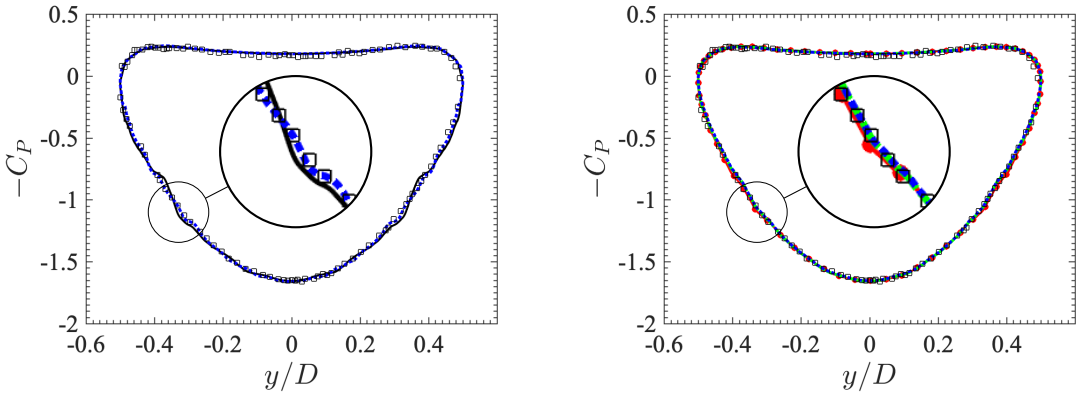

(a) $\epsilon = 0$ (b) $\epsilon > 0$

Figure 4.11: Coefficient of pressure for a steady flow past a circular cylinder at $\mathrm{Ma}_\infty = 2$ and $\mathrm{Re} = 300$. (a) $\Delta x = D/40$ (—) and $\Delta x = D/80$ (····) with $\epsilon = 0$. (b) $\Delta x = D/40$ for $\epsilon = \Delta$ (—●—), $\epsilon = 1.5\Delta$ (- - -), and $\epsilon = 3\Delta$ (····). Numerical body-fitted data [228] (□).

	$\epsilon = 0$	$\epsilon = 0$ ($\Delta x = D/80$)	$\epsilon = \Delta$	$\epsilon = 1.5\Delta$	$\epsilon = 3.0\Delta$	Body-fitted [228]
C_D	1.501	1.524	1.487	1.425	1.386	1.548
$C_{D,p}$	1.398	1.394	1.392	1.382	1.375	1.404
$C_{D,f}$	0.103	0.130	0.095	0.044	0.011	0.144

Table 4.2: Results for drag coefficient (C_D), pressure drag coefficient ($C_{D,p}$), and frictional drag coefficient ($C_{D,f}$) for supersonic flow past a cylinder with $\Delta x = D/40$ unless otherwise labeled and different regularization parameters (ϵ).

	$\epsilon = 0$ ($\Delta x = D/40$)	$\epsilon = 1.5\Delta$ ($\Delta x = D/40$)	Borker et al. [28]	Nagata et al. [167]
C_D	1.270	1.207	-	1.386
$C_{D,p}$	1.080	1.054	-	1.054
$C_{D,f}$	0.190	0.153	-	0.332
L_{shock}/D	0.213	0.237	0.203	0.201

Table 4.3: Drag coefficient (C_D), pressure drag coefficient ($C_{D,p}$), frictional drag coefficient ($C_{D,f}$), and shock standoff distance (L_{shock}) for a viscous supersonic flow past a sphere.

Farfield conditions with sponge zones are applied at the inflow and outflow and free-slip conditions are enforced at all other sides of the domain. Uniform grid spacing of $\Delta x = D/40$ is applied within a $10D \times 10D \times 10D$ box around the sphere. The grid is stretched to a coarser resolution of $\Delta x = D/2$ at the domain boundary. After reaching steady state, results for the shock stand-off distance and drag coefficient are compared to data obtained from numerical simulations performed with adaptive mesh refinement by Borker et al. [28] and body-fitted data from Nagata et al. [167]. It should be noted that the numerical data being compared to were performed using grid resolution near the surface of the sphere of $D/154$, approximately 4 times finer than what is used here.

As seen in Table 4.3, the stand-off distance of the resulting bow shock is predicted within 6% with $\epsilon = 0$ compared to Borker et al. [28], Nagata et al. [167]. The regularized treatment increases the standoff distance, resulting in an error of approximately 17%. Between 8% and 12% error is observed in the total drag coefficient, with the majority of the discrepancy arising from the prediction in frictional drag. As was shown in previous sections, the frictional drag is under-predicted when using $\epsilon > 0$, though these errors are expected to decrease with increasing resolution. Previous work has observed similar under-predictions in frictional drag [228]. In summary, the parameter-free (explicit) formulation of CBVP yields reasonably good predictions in the pressure drag and shock standoff distance. Regularization of the masking functions removes spurious oscillations near the surface, albeit at a cost of under predicting

the frictional drag component.

4.10 Conclusions

In this work, we propose an explicit form of the characteristic-based volume penalization method applied to both the Navier–Stokes and Euler equations. Penalization parameters are chosen based on the limitations of the underlying discretization, namely the simulation time step and sound speed. As a consequence, the resulting method does not rely on tuning parameters and avoids adding strict stability constraints. In addition, the masking function used to distinguish grid points between the interior and exterior of the solid object was replaced with a regularized Heaviside function to provide a smooth transition of the volume penalization terms.

A series of verification and validation cases were performed under both subsonic and supersonic conditions. The regularized masking function systematically reduces spurious oscillations near the immersed interface and allows for larger simulation time steps. However, the regularization was found to generate asymmetric pressure drag under inviscid steady flow conditions that results in unphysical drag at steady state. For unsteady flows or objects with flat surfaces, the regularization treatment yields similar results compared to the sharp interface treatment while reducing grid-to-grid oscillations. When applied to viscous flows, good agreement with numerical body-fitted data is observed without requiring excessively small grid spacing. However, regularization of the masking function systematically reduces the frictional drag contribution.

In summary, the resulting scheme is deemed *simple* as it only requires modifying the right-hand side of the transport equations and not the stencil operators; *efficient* as it does not add further restrictions to the simulation time step for explicit discretizations; and provides accurate predictions in steady and unsteady subsonic and supersonic flows. In addition, the scheme was shown to exhibit excellent mass conser-

vation properties. While the focus here was on stationary objects, modifications to account for moving objects were discussed. Further work is needed to improve frictional drag predictions when a regularized masking function is employed, in addition to curvature corrections for inviscid flows compatible with the regularized interface.

CHAPTER V

Quantification of Unclosed Terms during Shock-Particle Interactions

5.1 Introduction

Over the past several decades, significant progress has been made towards improving the numerical prediction of disperse multiphase flows (e.g., [11, 58, 232], and references therein). Yet, the majority of these efforts have focused on low-speed (incompressible) regimes. Two-phase flows that exhibit strong compressibility play dominant roles in nature, such as during supernovas and volcanic eruptions, in industry (coal dust explosions, shock wave lithotripsy, combustion/detonation, etc.) and space exploration (e.g., fluidization of terrestrial regolith during rocket plume-surface interactions [148, 65, 13]). Compared to their low-speed counterparts, particle-laden compressible flows like the examples listed here typically introduce new length- and time-scales and additional physics that further complicate modeling efforts.

In recent years, significant attention has been made on modeling two-way coupling of finite size particles [34, 81, 93, 12], yet accurate models capable of predicting the scenario illustrated in Fig. 1.4 remain elusive. Some of the challenges are attributed to the large slip velocities between the phases (which can be on the order of the sound speed), unsteadiness of the shockwave dynamics and associated wakes, and

back-coupling from the solid phase to the gas.

In the context of shock-particle interactions for moderately dilute and dense suspensions, small-scale velocity fluctuations are produced in particle interstitial sites and advected downstream with the mean flow [84, 207, 152] (see Fig. 1.4(b)). This results in subgrid-scale (or sub-filtered) velocity fluctuations that contribute to an unclosed term akin to the Reynolds stress that appears in single-phase flow, but here represents unresolved fluctuations due to the presence of particles. Because such fluctuations exist even in laminar flow (e.g., steady wakes), it is often referred to as *pseudo*-turbulent kinetic energy (PTKE). While this term is typically neglected in incompressible flows without significant consequence, recent DNS have shown that PTKE can contribute between 30% and 100% of the resolved kinetic energy in compressible flows [84, 207, 171, 152]. Its strength has been shown to increase as the particle volume fraction and the incident shock Mach number increase [152]. An algebraic model for the PTKE was recently proposed for incompressible homogeneous gas-solid flows [146] and compressible flows [171]. However, such models have only been tested under limited conditions and fail to predict PTKE in regions void of particles. Other models have been proposed based on cloud-in-cell approaches, where the unclosed subgrid-scale stresses are accounted for in the particle momentum balance using the so-called Subgrid Particle-Averaged Reynolds Stress-Equivalent (SPARSE) method [50, 231]. With the increase in available compressible DNS data in recent years [236, 238, 152], new models valid in higher-speed regimes can be developed and tested. The aim of this study is to present a framework for developing and integrating such models.

5.2 *A posteriori* analysis

In this section, we evaluate the relative contributions of the unclosed terms appearing in Sec. 2.3 by spatially filtering a direct solution to the microscale equations.

Numerical simulations of the shock-particle configuration illustrated in Fig. 1.4 are first presented, followed by an *a posteriori* analysis consistent with the filtering operators introduced in Sec. 2.3.1. Details on filtering methodology are provided in B.1. We briefly note that while the present analysis considers collections of monodisperse particles, the same filtering approach can be extended to polydisperse suspensions. In practice, the filter size applied to flows with polydisperse particles is typically chosen to be larger than the maximum particle size (e.g., [35, 20].)

5.2.1 Simulation configuration

The simulations are designed to emulate the multiphase shock tube experiment of Wagner et al. [249] and numerous computational studies since then [126, 195, 238, 84]. A shock wave passes through a suspension of rigid spherical particles distributed over a thickness $L^\star = 2$ mm (as shown in Fig. 5.1). The domain size is $L_x = 7.5$ in the streamwise direction, and $L_y = 1$ in the spanwise direction. All length scales are non-dimensionalized by $L^\star$. The shock is initialized at $x = 2.4$ with a shock Mach number of $\mathrm{Ma}_s = 1.66$. The post-shock (denoted with a subscript '1') and pre-shock (denoted with a subscript '2') conditions are given by $(\rho_1,\ p_1,\ u_1 \mid \rho_2,\ p_2,\ u_2) = (2.131,\ 2.177,\ 0.881 \mid 1,\ 0.714,\ 0)$. The Reynolds number based on $L^\star$ and the sound speed $c^\star_\infty = 343$ m/s is $\mathrm{Re}_c = 45394$.

Particles have density $\rho_p = 2520$ (non-dimensionalized by the gas-phase density) and diameter $d_p = 0.0575$, corresponding to 115 μm soda lime particles in air. A uniform grid of size 5250×700 is employed such that there are approximately 40 grid points across the diameter of each particle. Particles are initially distributed within a length of $L = 1$ starting at $x_0 = 2.5$ with a mean volume fraction within the span of $\varphi_p = 0.04$, 0.21, and 0.44, corresponding to $N_p = 16$, 81, and 169 particles, respectively. For the distribution, particles are initially placed uniformly and then every other column is shifted vertically by a distance equal to one half the mean

inter-particle spacing $\lambda_p/2$. This creates a staggered arrangement of particles. Each particle is then randomly perturbed within a radius less than $(\lambda_p - d_p)/2$ to mimic a random distribution while avoiding overlap with neighbors.

In this section, we consider two-dimensional simulations of stationary particles. With the parameters listed above, the ratio of the non-dimensional particle timescale, $\tau_p = \rho_p d_p^2/(18\mu) \approx 21000$, to the particle acoustic time scale, $\tau_d = d_p/c_\infty = 0.0575$, is large, indicating the particle motion is negligible over the simulation duration considered ($t < 3$). In addition, a recent experimental study suggests that the particle phase does not begin to spread until times corresponding to our non-dimensional time of $t \gtrsim 10$ [53]. Here, $t = 0$ corresponds to the instant the shock interacts with the leading edge of the particle phase. Thus, the assumption of stationary particles is valid over the time durations considered in this *a posteriori* analysis. We briefly note that the dynamics of a shock interacting with a spherical particle in three dimensions and a cylindrical particle in two dimensions are fundamentally different due to the timescales associated with the shock propagation. In addition, the wake structures confined in two dimensions result in larger values of PTKE compared to three dimensional configurations [152]. Despite this, two-dimensional simulations are performed in the present study to avoid the high computational cost associated with a direct solution to the three-dimensional viscous compressible flow equations. Thus, we seek to identify qualitative trends in the sub-filtered terms with mean particle concentration and filter size.

5.2.2 Discretization of the microscale equations

The microscale equations (2.1)–(2.3) are discretized using narrow-stencil high-order finite difference operators that satisfy the summation-by-parts (SBP) property on a structured curvilinear grid [220, 225]. All simulations presented in this study use the sixth-order formulation in the domain interior, and third-order, one-sided

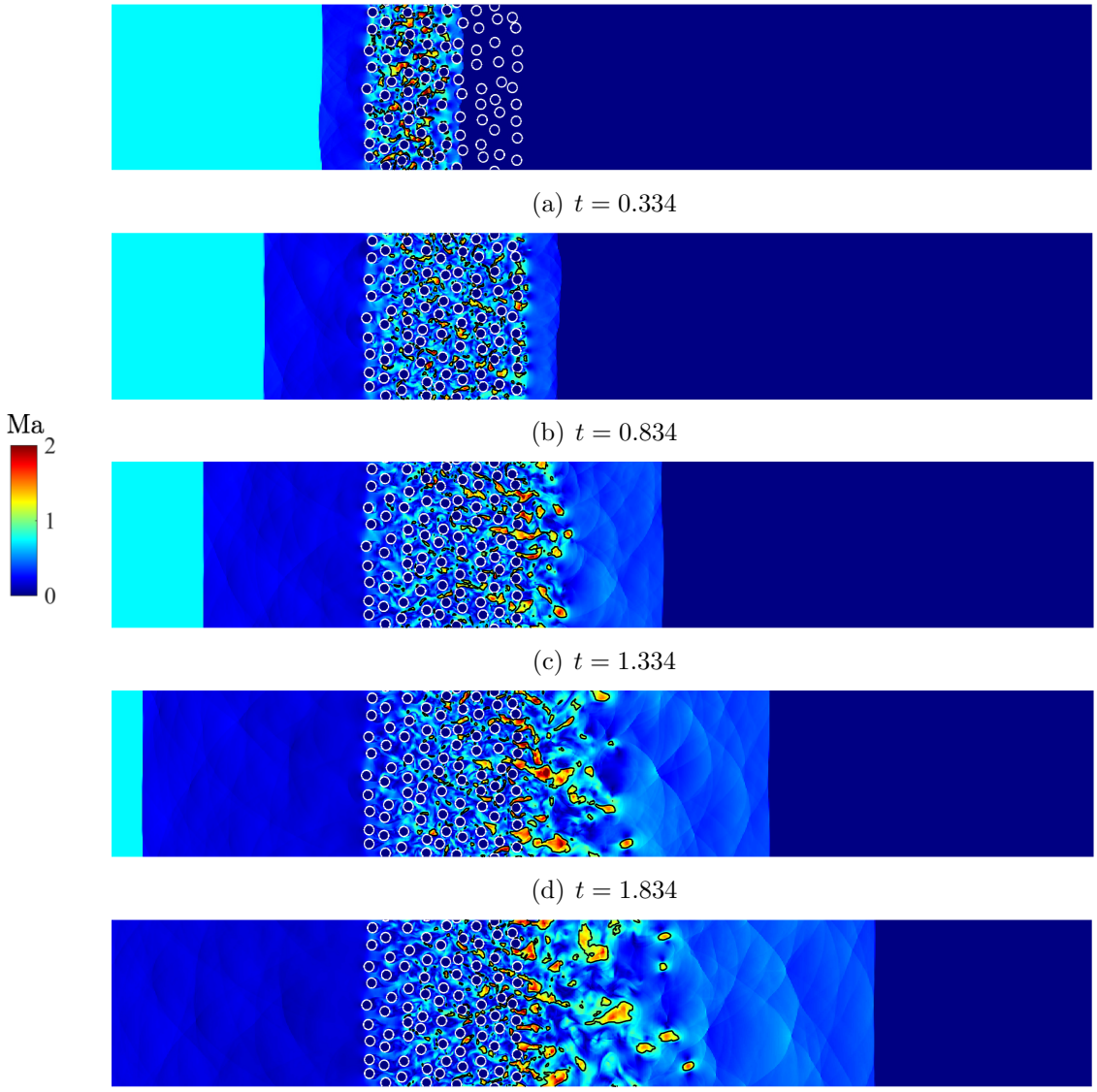

(a) $t = 0.334$

(b) $t = 0.834$

(c) $t = 1.334$

(d) $t = 1.834$

(e) $t = 2.334$

Figure 5.1: Mach number fields (color) for $\varphi_p = 0.21$. Contours of Ma $= 1$ (—).

operators at the boundary, resulting in overall fourth-order accuracy for the fluid-phase equations. To evaluate second and mixed derivatives, first derivative operators are applied consecutively, necessitating the use of artificial dissipation to damp the highest wavenumber components supported by the grid. To this end, high-order accurate SBP dissipation operators are used that provide artificial viscosity based on a sixth-order derivative with a diffusion coefficient that is a function of the local grid resolution [140, 247].

The SBP scheme is combined with the simultaneous approximation term (SAT) boundary treatment [38, 227] to ensure energy stability. This is achieved by enforcing non-reflecting characteristic boundary conditions weakly at the far field [227]. In addition, an absorbing sponge region [60] is applied at the domain boundary to prevent unphysical acoustic reflections by adding a damping term to the right-hand side of the fluid-phase equations. Finally, the equations are advanced in time using a standard fourth-order Runge–Kutta method.

Boundary conditions are enforced at the surface of each particle via a direct-forcing immersed boundary method. In this approach, Lagrangian markers are distributed over the surface of each particle and the gas-phase velocity is interpolated to the location of each to generate a forcing term added to the momentum equation (2.2). The associated work done by the immersed boundary is added to the microscale energy equation (2.3). A signed distance function is used to penalize the flow at grid points located within the solid phase to avoid spurious reflections as shocks pass through the particles. Additional details on this method can be found in Uhlmann [244], Boukharfane et al. [29].

5.2.3 Role of filtering on the Mach number

Instantaneous snapshots of the local Mach number for the $\varphi_p = 0.21$ case are shown in Fig. 5.1. Shortly after the shock interacts with the particles, a reflected

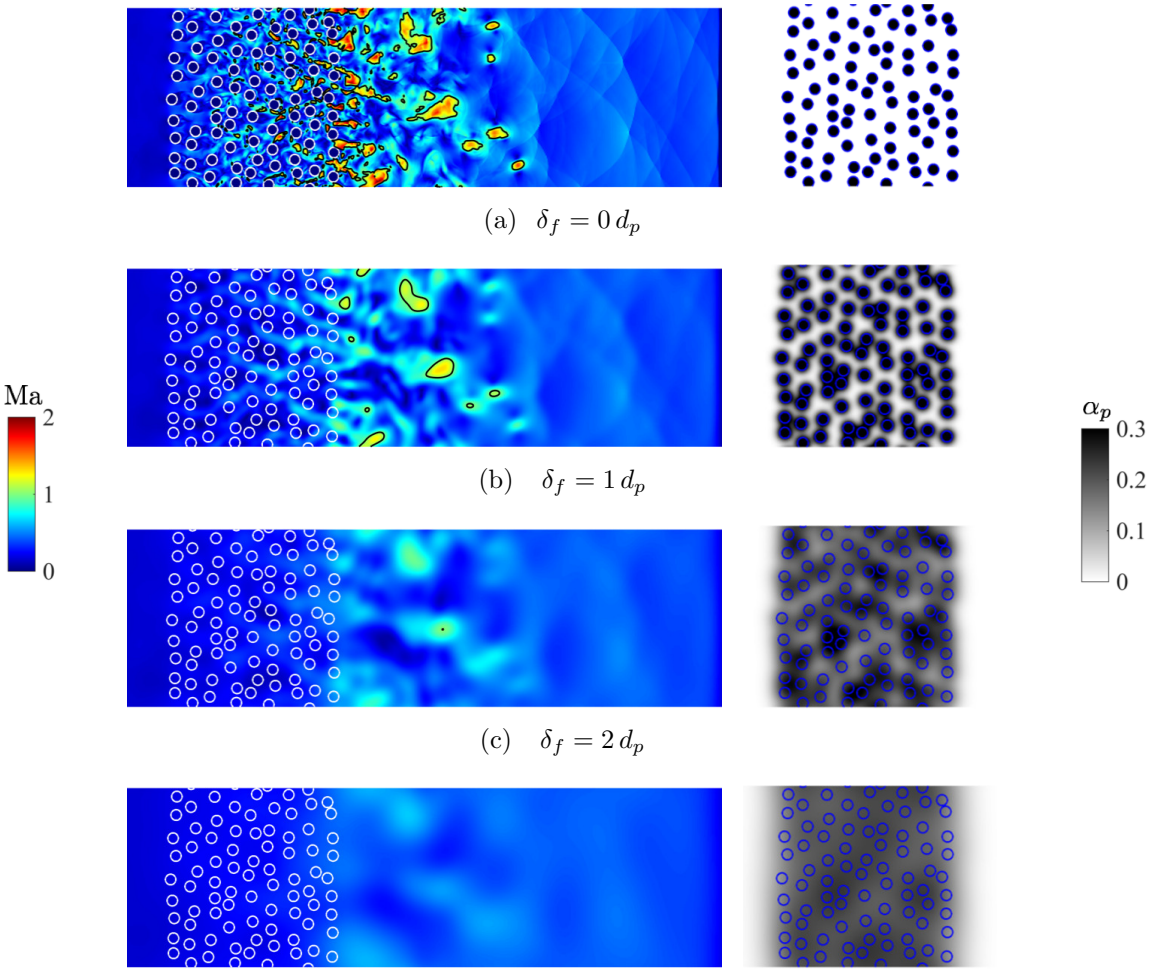

(a) $\delta_f = 0\, d_p$

(b) $\delta_f = 1\, d_p$

(c) $\delta_f = 2\, d_p$

(d) $\delta_f = 4\, d_p$

Figure 5.2: Mach number (left) and particle volume fraction (right) as a function of filter size for $\varphi_p = 0.21$ when $t = 2.334$. Contours of Ma $= 1$ (—).

shock propagates upstream while a transmitted shock travels through the particle suspension. The particles act to restrict the area of the transmitted shock, causing the gas phase to choke near the downstream edge due to the immediate change in volume fraction, followed by supersonic expansion. This rapid increase in gas-phase velocity at the downstream edge was found to significantly increase the particle acceleration in three-dimensional simulations of freely-evolving shock-particle interactions [238]. As discussed in Theofanous et al. [238], modeling approaches based on spatially averaged fields (e.g., Eulerian–Eulerian and Eulerian–Lagrangian methods) fail to predict this choking behavior, and are thus unable to accurately predict particle dispersion.

To explore this concept further, the local Mach number is shown in Fig. 5.2(a) computed using filtered quantities according to $\mathrm{Ma} = |\widetilde{\boldsymbol{u}}|/\sqrt{(\gamma-1)\widetilde{T}}$ shortly after the shock has passed through the particle suspension. The flow field obtained from particle-resolved DNS is spatially filtered using the operators defined in Sec. 2.3.1 for filter sizes ranging between $0 \leq \delta_f \leq 4d_p$. The local volume fraction is also plotted by filtering the indicator function defined in Eq. (2.8). Details on the implementation of the filtering procedure can be found in B.1. Filtering (or locally averaging) the flow field systematically acts to reduce the extent to which the gas phase accelerates at the downstream edge of the particles. In addition, the filter acts to 'smear' the volume fraction, and consequently the nozzle-like flow contraction would be less significant when solving the volume-filtered equations. Here, we argue that with proper treatment of the sub-filtered terms, the correct level of particle acceleration can be recovered.

5.2.4 Role of filtering on the velocity fluctuations

As shown in Sec. 2.3, one consequence of volume filtering is the appearance of sub-filtered velocity fluctuations in the Reynolds stress-like term $\boldsymbol{R}_u$, pseudo-turbulent diffusion $\boldsymbol{R}_{uu}$, and PTKE k. From Fig. 5.2, it can be seen that the majority of the

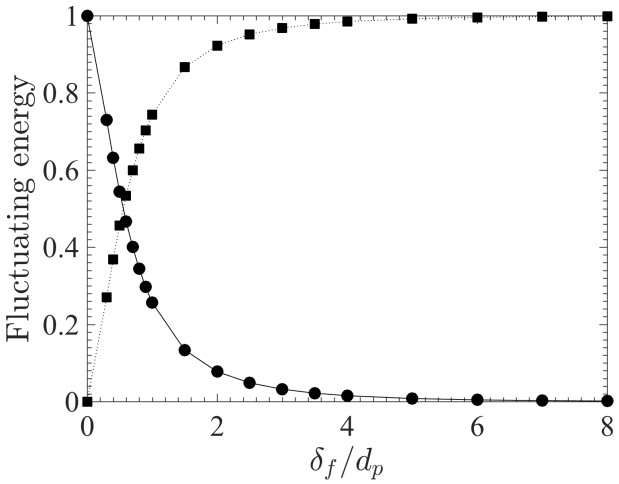

Figure 5.3: Relative contributions of the fluctuating kinetic energy averaged across the entire domain. Filtered fluctuations, $\langle\widetilde{\boldsymbol{u}}\cdot\widetilde{\boldsymbol{u}}\rangle_{xy}-\langle\widetilde{\boldsymbol{u}}\rangle_{xy}\cdot\langle\widetilde{\boldsymbol{u}}\rangle_{xy}$ (-●-), and sub-filtered fluctuations, $\langle\boldsymbol{u}\cdot\boldsymbol{u}\rangle_{xy}-\langle\widetilde{\boldsymbol{u}}\cdot\widetilde{\boldsymbol{u}}\rangle_{xy}$ (··■··), as a function of filter size for $\varphi_p = 0.21$ when $t = 2.334$, normalized by the total fluctuating energy.

velocity fluctuations contained in the filtered field are suppressed when $\delta_f \gtrapprox 4d_p$. To quantify the relative contributions of the filtered and sub-filtered fluctuations, the velocity field is decomposed into $\boldsymbol{u} = \widetilde{\boldsymbol{u}} + \boldsymbol{u}''$, and then averaged across the x- (streamwise) and y- (spanwise) directions. In this work, angled brackets denote Favre averaging, and the subscript denotes the direction in which averaging is performed. For example, averaging across y is given by $\langle A\rangle_y = \int_0^{L_y}(\alpha\overline{\rho}A)\ \mathrm{d}y/\int_0^{L_y}(\alpha\overline{\rho})\ \mathrm{d}y$, for an arbitrary quantity A. With this, the domain-average filtered velocity is defined as $\langle\widetilde{\boldsymbol{u}}\rangle_{xy}$, which can be used to construct the total fluctuating kinetic energy as $\langle\boldsymbol{u}\cdot\boldsymbol{u}\rangle_{xy} - \langle\widetilde{\boldsymbol{u}}\rangle_{xy}\cdot\langle\widetilde{\boldsymbol{u}}\rangle_{xy}$. The portion of this energy containing only filtered terms is $\langle\widetilde{\boldsymbol{u}}\cdot\widetilde{\boldsymbol{u}}\rangle_{xy} - \langle\widetilde{\boldsymbol{u}}\rangle_{xy}\cdot\langle\widetilde{\boldsymbol{u}}\rangle_{xy}$, and the residual contributions contain only sub-filtered terms, i.e. $\langle\boldsymbol{u}\cdot\boldsymbol{u}\rangle_{xy} - \langle\widetilde{\boldsymbol{u}}\cdot\widetilde{\boldsymbol{u}}\rangle_{xy}$. In the limit $\delta_f \to \infty$, $\widetilde{\boldsymbol{u}} \to \langle\widetilde{\boldsymbol{u}}\rangle_{xy}$, and all of the fluctuations reside at the sub-filter scale.

As seen in Fig. 5.3, the filtered and sub-filtered components of the fluctuating energy have equal contributions when $\delta_f \approx d_p$, and the majority of energy resides at

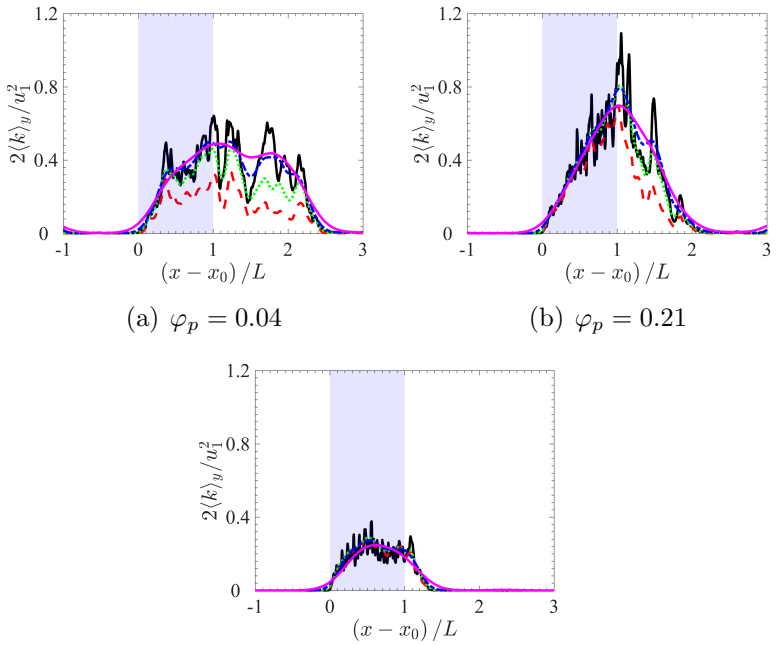

(a) $\varphi_p = 0.04$ (b) $\varphi_p = 0.21$

(c) $\varphi_p = 0.44$

Figure 5.4: Comparison of PTKE obtained from ensemble averaging (—) and volume filtering with $\delta_f = d_p$ (- - -), $\delta_f = 2d_p$ (····), $\delta_f = 4d_p$ (-·-), and $\delta_f = 8d_p$ (—) at $t = 2.334$. The shaded region (▒) indicates particle location.

the sub-filter scale when $\delta_f \gtrapprox 4d_p$. In practice, the gas phase is typically discretized on a mesh with grid spacing larger than the particle diameter. If δ_f is interpreted as the grid spacing, this would suggest the subgrid-scale velocity fluctuations always contribute significantly to the total fluctuating kinetic energy. In addition, any model for the subgrid-scale velocity fluctuations under these conditions should be aware of the portion of energy being resolved when δ_f is not significantly larger than the particle diameter.

Figure 5.4 shows streamwise profiles of the averaged PTKE as a function of filter size and mean particle volume fraction. The PTKE obtained using sub-filtered velocity fluctuations is compared to the result obtained from ensemble averaging the microscale velocity in the y-direction. Ensemble averaging is typically employed when extracting statistics from particle-resolved simulations of similar configurations [195, 84, 152, 171]. Except for the most dilute case ($\varphi_p = 0.04$), PTKE ob-

tained from ensemble averaging exhibits qualitatively similar trends. For the most dilute case, the magnitude of PTKE increases as the filter size increases, approaching the solution obtained from ensemble averaging when $\delta_f \gtrapprox 4d_p$. For each case, PTKE based on ensemble averaging is significantly more noisy than its filtered counterpart due to the lack of averaging in the x-direction.

In general, PTKE is seen to depend on both δ_f and φ_p. A key trend observed in Fig. 5.4 is that the PTKE dependence on δ_f only occurs when the volume fraction is sufficiently small. The simulation results reveal that the PTKE dependence can be collapsed to a Knudsen number based on the mean inter-particle spacing, λ_p, given by

$$\mathrm{Kn}_\delta = \frac{\lambda_p}{\delta_f}. \tag{5.1}$$

When $\mathrm{Kn}_\delta < 1$, the majority of the velocity fluctuations generated in particle interstitial sites reside within the support of the filter kernel. As seen in Fig. 5.5, the cases with $\varphi_p = 0.21$ and 0.44 correspond to $\mathrm{Kn}_\delta < 1$, and thus PTKE is not seen to vary with δ_f in Figs. 5.4(b)–5.4(c). When $\delta_f = d_p$, $\mathrm{Kn}_\delta > 1$ across all possible volume fractions (dilute to close-packing). In summary, models attempting to predict PTKE need not take into consideration both the local volume fraction and filter size, but instead this dependency can be captured via Kn_δ. For freely-evolving particle suspensions, Kn_δ will vary in space and time.

5.2.5 Assessment of the unclosed terms

The magnitude of the unclosed stresses appearing in the volume-filtered energy equation (2.30) are provided in Fig. 5.6 for $\delta_f = d_p$ and $4d_p$ and compared against the resolved (filtered) pressure work term $\overline{p}\widetilde{\boldsymbol{u}}$. The larger filter size acts to smooth out the profiles, without noticeable change to their magnitude. Owing to the effect of Kn_δ as previously discussed, the dependence of the sub-filtered stresses on δ_f is only seen for the most dilute case. Perhaps not unexpectedly, the sub-filtered correlation

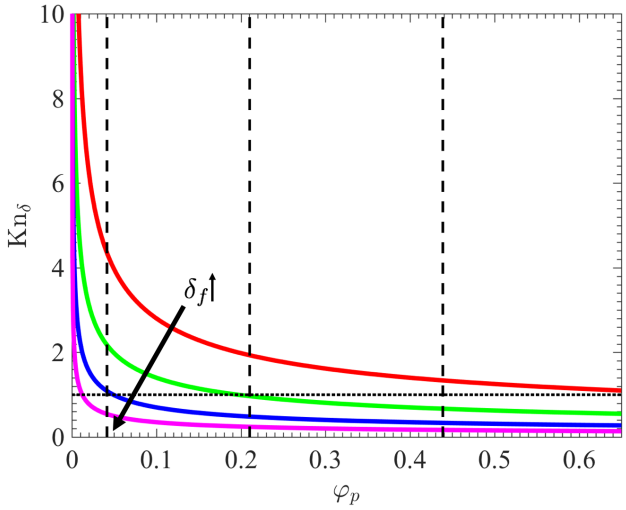

Figure 5.5: Filter size dependent Knudsen number as a function of φ_p with $\delta_f = d_p$, (—), $\delta_f = 2d_p$ (—), $\delta_f = 4d_p$ (—), and $\delta_f = 8d_p$ (—). Reference lines are also shown for $\mathrm{Kn}_\delta = 1$ ($\cdots$) and the three volume fractions under consideration (- - -).

between the viscous stress and velocity, $\boldsymbol{R}_{\tau u}$, is negligible owing to the large Reynolds numbers under consideration. The pseudo-turbulent heat flux, $\boldsymbol{R}_{Tu}$, is also relatively small. While this has not been tested, $\boldsymbol{R}_{Tu}$ may be important for reacting flows or cases involving large temperature gradients and should be evaluated in future work. The pseudo-turbulent diffusion, $\boldsymbol{R}_{uu}$, is seen to be the dominating sub-filtered stress. This term contains triple products of sub-filtered velocity fluctuations, which could be challenging to develop models for. This term is sometimes expressed as a product of the filtered velocity and Reynolds stress. It can be seen in Fig. 5.6 that $\boldsymbol{R}_{uu} \approx 2\boldsymbol{R}_u \cdot \widetilde{\boldsymbol{u}}$ yields overall good agreement for small and large filter sizes as well as a range of mean particle volume fractions. In summary, $\boldsymbol{R}_{uu}$ is the only non-negligible sub-filtered stress appearing in Eq. (2.30), which can be closed provided a model for $\boldsymbol{R}_u$.

In Sec. 2.3.4.1, we showed that filtering the equation of state results in an additional contribution by the PTKE when computing pressure. From Eq. (2.33), it can be seen that the PTKE systematically acts to reduce the local pressure, which could

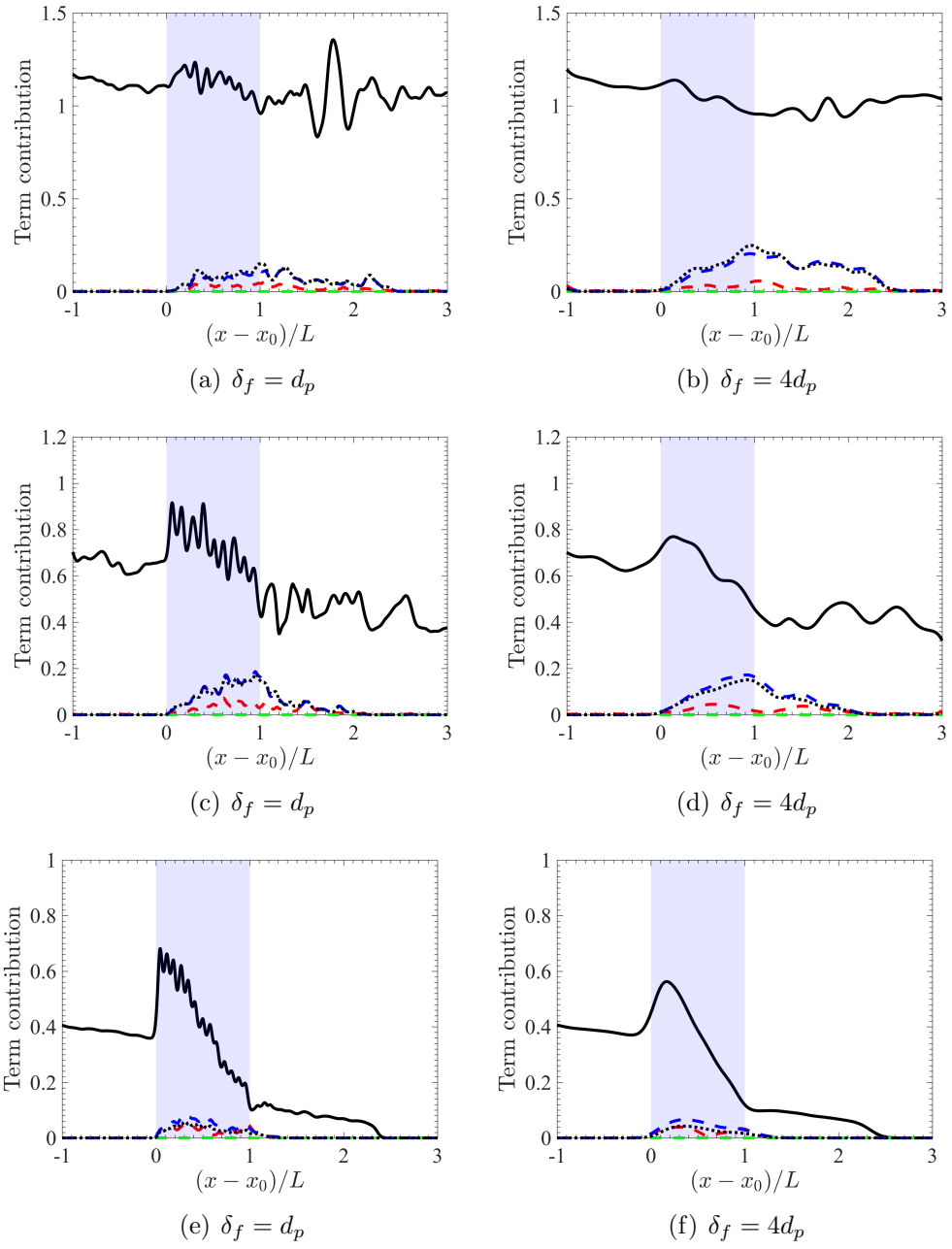

Figure 5.6: Magnitude of the Favre averaged sub-filtered stresses appearing in Eq. (2.30) as a function of filter size for $(a)-(b)$ $\varphi_p = 0.04$, $(c)-(d)$ $\varphi_p = 0.21$, and $(e)-(f)$ $\varphi_p = 0.44$ when $t = 2.334$. $\langle|\overline{p}\widetilde{\boldsymbol{u}}|\rangle_y$ (—), $\langle|\boldsymbol{R}_{Tu}|\rangle_y$ (- - -), $\langle|\boldsymbol{R}_{\tau u}|\rangle_y$ (- - -), $1/2\langle|\boldsymbol{R}_{uu}|\rangle_y$ (·····), and $\langle|\boldsymbol{R}_u \cdot \widetilde{\boldsymbol{u}}|\rangle_y$ (- - -) normalized by $\rho_1 u_1^3$. The shaded region ( ) indicates particle location.

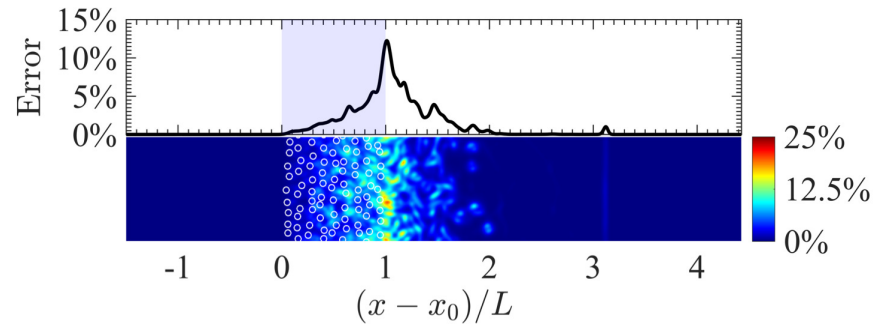

(a) $\delta_f = d_p$

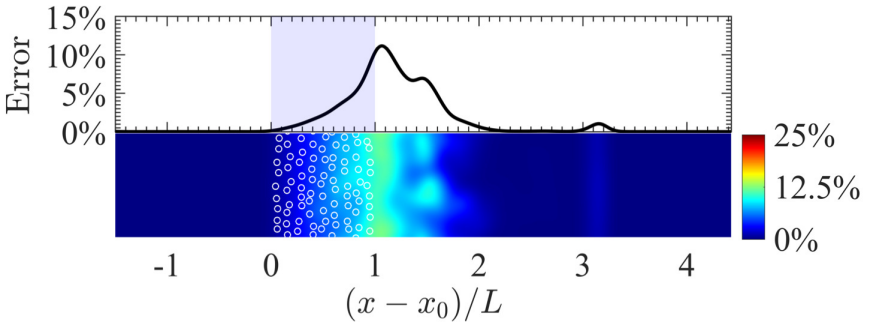

(b) $\delta_f = 4d_p$

Figure 5.7: Error in the pressure field as a consequence of excluding PTKE in Eq. 2.33 for $\varphi_p = 0.21$ when $t = 2.334$. Averaged error (—) and local error (color). The shaded region (▪) indicates particle location.

result in underpredictions of the local Mach number if not accounted for properly. This could be especially important in regions of large volume fraction gradients that were demonstrated to choke the flow and lead to supersonic expansion. To quantify this error, we compare the pressure obtained using only filtered quantities (i.e., neglecting PTKE), as is typically done in coarse-grained simulations of gas-solid flows, with the true filtered pressure that contains this contribution. From Fig. 5.7, it can be seen that errors in the pressure field are maximum near the downstream edge of the particle suspension where the gas phase accelerates to supersonic speeds. As much as 25% discrepancy is observed in the pressure field when neglecting PTKE with $\delta_f = d_p$. The maximum local error is not as significant for $\delta_f = 4d_p$, but still results in approximately 15% relative error. Because $\mathrm{Ma} \propto \sqrt{\overline{p}}$, the errors in Mach number are even more significant.

5.3 Coarse-grained modeling

In this section, we present a volume-filtered Eulerian–Lagrangian (VF-EL) approach for simulating particle-laden compressible flows. First, a model is proposed for transporting PTKE and reconstructing the pseudo-turbulent Reynolds stress tensor. Details on the numerical discretization of the volume-filtered equations are then presented, followed by verification and validation against existing data. For clarity of presentation, the $\overline{(\cdot)}$ and $\widetilde{(\cdot)}$ notation will be dropped in the remainder of this chapter.

5.3.1 Modeling PTKE and the pseudo-turbulent Reynolds stresses

The *a posteriori* analysis performed in Sec. 5.2 demonstrated the PKTE, k, in compressible gas-solid flows. While algebraic models for this term have been proposed in the past [146, 171], a key feature of pseudo-turbulence in the flows considered here is that it gets advected with the mean flow downstream from the particles (see Fig. 5.4). Therefore, models for k based on the local volume fraction will fail to accurately predict important wake structures in regions void of particles. To this end, a transport equation for the PTKE was derived in Sec. 2.3.4.2 using a consistent set of volume filtering operators.

Starting from Eq. (2.34), replacing $\boldsymbol{R}_{uu} = 2\boldsymbol{u} \cdot \boldsymbol{R}_u$ (as justified in Sec. 5.2.5), and rearranging and consolidating terms yields

$$\frac{\partial \alpha \rho k}{\partial t} + \nabla \cdot (\alpha \rho \boldsymbol{u} k) + \alpha \boldsymbol{R}_u : \nabla \boldsymbol{u} = (\boldsymbol{u}_p - \boldsymbol{u}) \cdot \boldsymbol{\mathcal{F}} - \alpha \rho \varepsilon_{PT}, \tag{5.2}$$

where the viscous and sub-filtered contributions have been absorbed into ε_{PT}, which represents dissipation of PTKE. Note that the terms involving resolved pressure and viscous stresses appearing on the second line of Eq. (2.34) contribute to the generation of internal energy and thus are not included in Eq. (5.2).

Following what is typically done in turbulence modeling [246], the dissipation rate

is modeled as $\varepsilon_{PT} \propto k/\tau_\varepsilon$, where τ_ε is a dissipation time scale that requires modeling. A common approach is to assume the sub-filtered velocity fluctuations are dissipated on a time scale $\tau_1 = \mathcal{L}/\sqrt{k}$, with $\mathcal{L}$ an integral length scale that is anticipated to be on the order of d_p. Another candidate time scale for multiphase flows is $\tau_2 = \mathcal{L}/|\boldsymbol{u}_f - \boldsymbol{u}_p|$. In the present study, it was found that both definitions predict similar distributions of PTKE but τ_2 yields better magnitudes. However, the slip velocity is ill-defined in regions void of particles. To this end, we propose to blend the two time scales according to

$$\varepsilon_{PT} = (1 - f_\alpha)\frac{C_f k}{\tau_1} + f_\alpha \frac{C_f k}{\tau_2}, \tag{5.3}$$

where C_f is a constant that requires closure and f_α is a blending function. The function f_α takes the following form to ensure the time scale based on the slip velocity is only used in the presence of particles

$$f_\alpha = \tanh\left(\frac{50}{\max(\alpha_p)}\alpha_p\right). \tag{5.4}$$

Based on the work of Mehrabadi et al. [146], the pseudo-turbulent Reynolds stress tensor is reconstructed from the PTKE according to

$$\boldsymbol{R}'_u = 2\rho k\left(\boldsymbol{b} + \frac{1}{3}\mathbb{I}\right), \tag{5.5}$$

where $\boldsymbol{R}'_u$ is the Reynolds stress aligned with the local slip velocity and $\boldsymbol{b}$ is the anisotropic stress tensor defined as

$$\boldsymbol{b} = f_\alpha \begin{bmatrix} b_{||} & 0 & 0 \\ 0 & b_\perp & 0 \\ 0 & 0 & b_\perp \end{bmatrix}. \tag{5.6}$$

The component parallel to the slip velocity is given by

$$b_{||} = \frac{a}{1 + b\exp(-c\mathrm{Re}_p)} \exp\left(\frac{d\ \alpha_p}{1 + e\exp(-f\mathrm{Re}_p)}\right), \tag{5.7}$$

and $b_\perp = -b_{||}/2$ is the perpendicular component such that $\mathrm{tr}(\boldsymbol{b}) = 0$. The pseudo-turbulent Reynolds stress tensor must be rotated to align with the Cartesian coordinate system. Details on the implementation of the rotation matrix can be found in [181]. For homogeneous, statistically stationary, incompressible gas-solid flows, the model constants are [146] $a = 0.523,\ b = 0.305,\ c = 0.114,\ d = 3.511,\ e = 1.801,$ and $f = 0.005$. In Eq. (5.7), Re_p is the particle Reynolds number, which is first computed at the location of each particle then projected to the Eulerian grid. The Reynolds number at the i-th particle is defined as $\mathrm{Re}_p^{(i)} = \alpha\rho|\boldsymbol{u} - \boldsymbol{v}_p^{(i)}|d_p/\mu$. Details on the projection method are provided in Sec. 3.2.1.

It is important to note that the model for the anisotropic stress tensor was originally developed for Eulerian–Eulerian methods. A correction needs to be applied to handle anisotropy in regions void of particles where Re_p is undefined. One choice is to set $\mathrm{Re}_p = 0$ away from particles. However, by inspection of Eq. (5.7), in the limit of zero Reynolds number, the parallel component of the aligned tensor approaches $b_{||} \to a/(1 + b)$. In this work, the anisotropic stress tensor is multiplied by f_α such that it smoothly approaches zero away from particles. Thus when $\alpha_p \to 0$, $\boldsymbol{b} = 0$ and the pseudo-turbulent Reynolds stress becomes isotropic.

In summary, a transport equation is introduced for the PTKE, and an algebraic model is employed to reconstruct $\boldsymbol{R}_u$. As a consequence, anisotropy is only predicted in the vicinity of particles, though finite PTKE can exist away from particles. Drag acts to produce PTKE in regions of finite slip velocity according to $(\boldsymbol{u}_p - \boldsymbol{u}) \cdot \boldsymbol{\mathcal{F}}$, and ε_{PT} dictates its magnitude. A key aspect of the proposed PTKE modeling approach is that it is agnostic to the drag model employed. A natural choice is to use the drag

Conservation of mass

$$\frac{\partial \alpha\rho}{\partial t} + \nabla \cdot (\alpha\rho\boldsymbol{u}) = 0$$

Conservation of momentum

$$\frac{\partial \alpha\rho\boldsymbol{u}}{\partial t} + \nabla \cdot (\alpha \{\rho\boldsymbol{u} \otimes \boldsymbol{u} + \boldsymbol{R}_u\}) = \alpha\nabla \cdot (\boldsymbol{\tau} - p\mathbb{I}) + \boldsymbol{\mathcal{F}}$$

Conservation of energy

$$\begin{aligned}\frac{\partial \alpha\rho E}{\partial t} &+ \nabla \cdot (\alpha\boldsymbol{u} \{\rho E + p\} + \alpha\boldsymbol{u} \cdot \{\boldsymbol{R}_u - \boldsymbol{\tau}\}) \\ &= -\alpha\nabla \cdot \boldsymbol{q} - (p\mathbb{I} - \boldsymbol{\tau}) : \nabla (\alpha_p \boldsymbol{u}_p) + \boldsymbol{u}_p \cdot \boldsymbol{\mathcal{F}} + \mathcal{Q}\end{aligned}$$

Pseudo-turbulent kinetic energy

$$\frac{\partial \alpha\rho k}{\partial t} + \nabla \cdot (\alpha\rho\boldsymbol{u}k) + \alpha\boldsymbol{R}_u : \nabla\boldsymbol{u} = (\boldsymbol{u}_p - \boldsymbol{u}) \cdot \boldsymbol{\mathcal{F}} - \alpha\rho\varepsilon_{PT}$$

Table 5.1: A summary of gas-phase volume filtered equations of motion.

correlation proposed by Tenneti et al. [233] to close $\boldsymbol{\mathcal{F}}$, since it is based on the the same DNS data used to develop the anisotropic stress model in [146]. However, the drag model of Tenneti et al. [233] is only valid when $\mathrm{Re}_p \lessapprox 300$. For the shock particle interactions considered here, Re_p is found to exceed 1000. In our previous work [211], we showed that the drag correlation of Gidaspow [69] yields the best results during shock-particle interactions of moderately dense systems due to the volume fraction and high Reynolds number corrections. While new Mach number-dependent drag laws valid in high volume fraction regimes are needed, the drag model proposed by Gidaspow [69] is adopted in the present study. Details on the drag implementation will be provided in Sec. 3.1.2.

5.3.2 Discretization of the volume-filtered equations

5.3.2.1 Gas-phase description

The volume-filtered equations of motion summarized in Table 5.1 are discretized using the same high-order, energy-stable methods presented in Sec. 5.2.2. To avoid spurious oscillations near particles that may arise even when the flow field is at rest, the volume fraction must be removed from the conserved variables prior to adding dissipation, i.e., the SBP dissipation is based on high-order derivatives of $\vec{Q}/\alpha$. Here, $\vec{Q} = [\alpha\rho,\ \alpha\rho\boldsymbol{u},\ \alpha\rho E]^{\mathsf{T}}$ is the vector of conserved gas-phase variables.

5.3.3 Verification – a converging-diverging nozzle

Verification of the VF-EL framework is conducted in the context of a one-dimensional converging-diverging nozzle. In this example, the area change is a consequence of the local change in volume fraction. Particles are placed within a length L with varying spacing such that the area change due to the corresponding volume fraction distribution is approximately Gaussian. The volume fraction distribution is centered in a domain of size $L_x = 5.12L$. The gas-phase density, velocity, and pressure are initialized with post-shock conditions for a shock Mach number of $\mathrm{Ma}_s = 1.66$, given by $(\rho,\ u,\ p) = (2.131,\ 0.881,\ 2.177)$. An analytic solution for the resulting pressure profile can be found in Liepmann and Roshko [123].

Two methods are employed to define the volume fraction field. First, the volume fraction is prescribed analytically as a smoothly varying Gaussian function with a standard deviation of $L/4$ and maximum value of 0.08. (see Fig. 5.8(a)). These parameters were chosen such that the minimum nozzle area is below the critical area for a choked flow. In the second approach, Lagrangian particles are used to generate the volume fraction field according to Eq. (3.15) to test the convergence of the two-way coupling scheme. In this approach, particles with diameters $d_p = 1.0 \times 10^{-3} L$ are

spaced such that the volume fraction distribution resembles the Gaussian distribution employed in the first approach. Two interphase filter sizes are considered for this example, $\delta_f = 0.1L$ and $\delta_f = 0.2L$.

A grid refinement study is performed by varying the grid spacing $0.3 \leq \Delta x/d_p \leq 40$ and the simulations are run until they reach steady state. As shown in Fig. 5.8(b), convergence of the steady-state pressure field towards the analytic solution is achieved in both approaches. When the volume fraction is prescribed, the L_2 error norm converges with 5-th order accuracy, consistent with the SBP-SAT discretization described in Sec. 5.2.2. Although lower convergence is observed when the volume fraction is generated from the two-way coupling scheme, the two-step filter ensures the solution converges to the analytic result even when $\Delta x < d_p$. The reduction in convergence when Lagrangian particles are considered is a consequence of the ADI scheme used in the implicit filtering operation. The convergence rate also depends on the smoothness of the volume fraction field, as seen when the value of δ_f is varied. Employing higher-order filters or mollification kernels can be used to improve the convergence rate, albeit at a higher cost.

5.3.4 Modeling PTKE in a two-dimensional shock-particle configuration

In this section, VF-EL simulations are compared against the two-dimensional particle-resolved simulations reported in Sec. 5.2. A shock with a Mach number $\mathrm{Ma}_s = 1.66$ interacts with stationary particles using the same particle distribution employed in the DNS. The ratio of particle-to-fluid heat capacity is $C_{p,p} = 0.8375$, corresponding to soda-lime particles in air. The integral length scale appearing in the dissipation model (5.3) is taken to be $\mathcal{L} = d_p$. A domain is discretized using a uniform grid of size 263×36–approximately 20 times smaller in each direction compared to the DNS–such that there are approximately two points across the diameter of each Lagrangian particle. The filter size is taken to be $\delta_f = 4d_p$, however, the

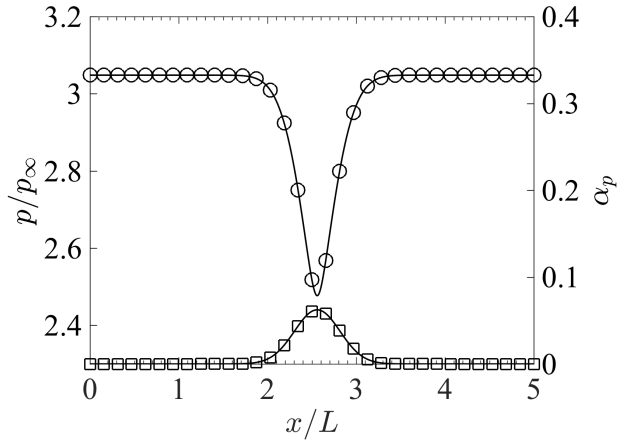

(a) Numerical solution of the gas-phase pressure at steady state normalized by the ambient pressure p_∞ (○) with a prescribed volume fraction (□). Analytic solutions (—).

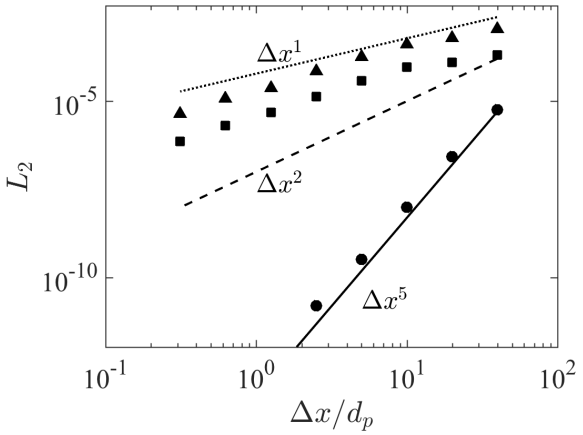

(b) L_2 error of the pressure profile at steady state during grid refinement using a filter size of $\delta_f = 0.1L$ (▲), $\delta_f = 0.2L$ (■), and a prescribed volume fraction field (●).

Figure 5.8: Verification of a converging-diverging nozzle.

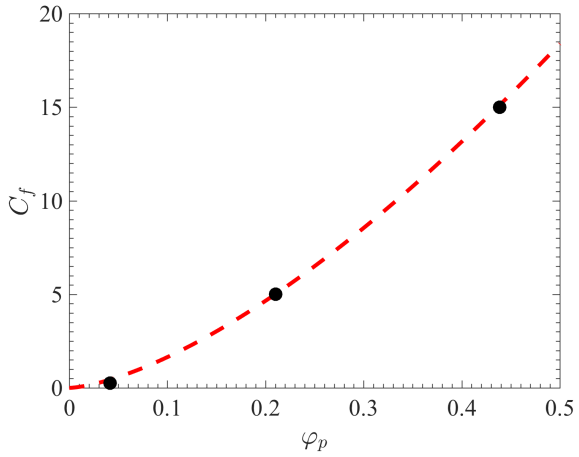

Figure 5.9: Power-law fit of the coefficient appearing in the dissipation model (5.3) to the two-dimensional simulations. Values extracted from DNS (•) and $C_f = 52\varphi_p^{1.5}$ (- - -).

results reported here remain relatively unchanged for $2 \leq \delta_f/d_p \leq 8$. Finally, we note that the coefficients used in the anisotropy model (5.5)–(5.7) were derived for three-dimensional flows. Using this model in two dimensions yields negative normal components of the Reynolds stress tensor. Thus, in this section, $\boldsymbol{R}_u$ is taken to be isotropic. The efficacy of the anisotropic model will be assessed in the following section.

A key parameter appearing in the coupled set of volume filtered equations (summarized in Table 5.1) is C_f from the PTKE dissipation model (5.3). It was found that $C_f = 0.25,\ 5.0,$ and 15.0 yields the best agreement in PTKE for $\varphi_p = 0.04$, 0.21, and 0.44, respectively. This dependence on volume fraction is expected, since wakes interact more strongly with each other and the particles as φ_p increases. Based on these results, a power-law fit was obtained for C_f (see Fig. 5.9) according to

$$C_f \approx 52\varphi_p^{1.5}. \tag{5.8}$$

This dependency will change in three dimensions, and also depend on the shock

Mach number and drag model employed (see Sec. 5.3.5). We note that coarser grid resolutions and larger filter sizes were found to have negligible effects on the values of C_f.

Overall good agreement can be observed in the prediction of PTKE between the model and DNS (see Fig. 5.10). For a fixed value of C_f, VF-EL captures the magnitude and distribution of PTKE over the time horizon considered. It should be noted that the bi-modal behavior observed in the DNS at early times is a result of the transmitted and reflected shocks. Because this sub-filtered contribution is purely hydrodynamics, i.e., it would appear even in the absence of particles, it should not be expected to be captured by the PTKE model. It is notable that the model is capable of predicting PTKE within the particle curtain as well as downstream in regions void of particles.

A comparison between the spatial distribution of PTKE is shown in Fig. 5.11 corresponding to the conditions reported in Fig. 5.10(e). Despite a factor of approximately 400 reduction in grid resolution, VF-EL captures the main features of the spatial distribution exceptionally well. Any discrepancy seen between DNS data and VF-EL can be attributed to the unresolved contributions of sub-filtered terms, which were lumped into ε_{PT}, and by neglecting anisotropy.

As mentioned in Sec 5.2.5, neglecting the effect of PTKE will systematically act to over-predict the local pressure and as a consequence may result in errors in the local Mach number. As shown in Fig. 5.12, the instantaneous fields reveal under-predictions in Mach number when VF-EL is performed without the PTKE model. The maximum local Mach number is located near the downstream edge of the particles with a value of approximately Ma = 0.63 when PTKE is accounted for and Ma = 0.61 when PTKE is neglected. While the magnitudes are relatively close, the distribution of Mach number differs, namely at the downstream edge of the particles where choking followed by supersonic expansion was observed in the DNS.

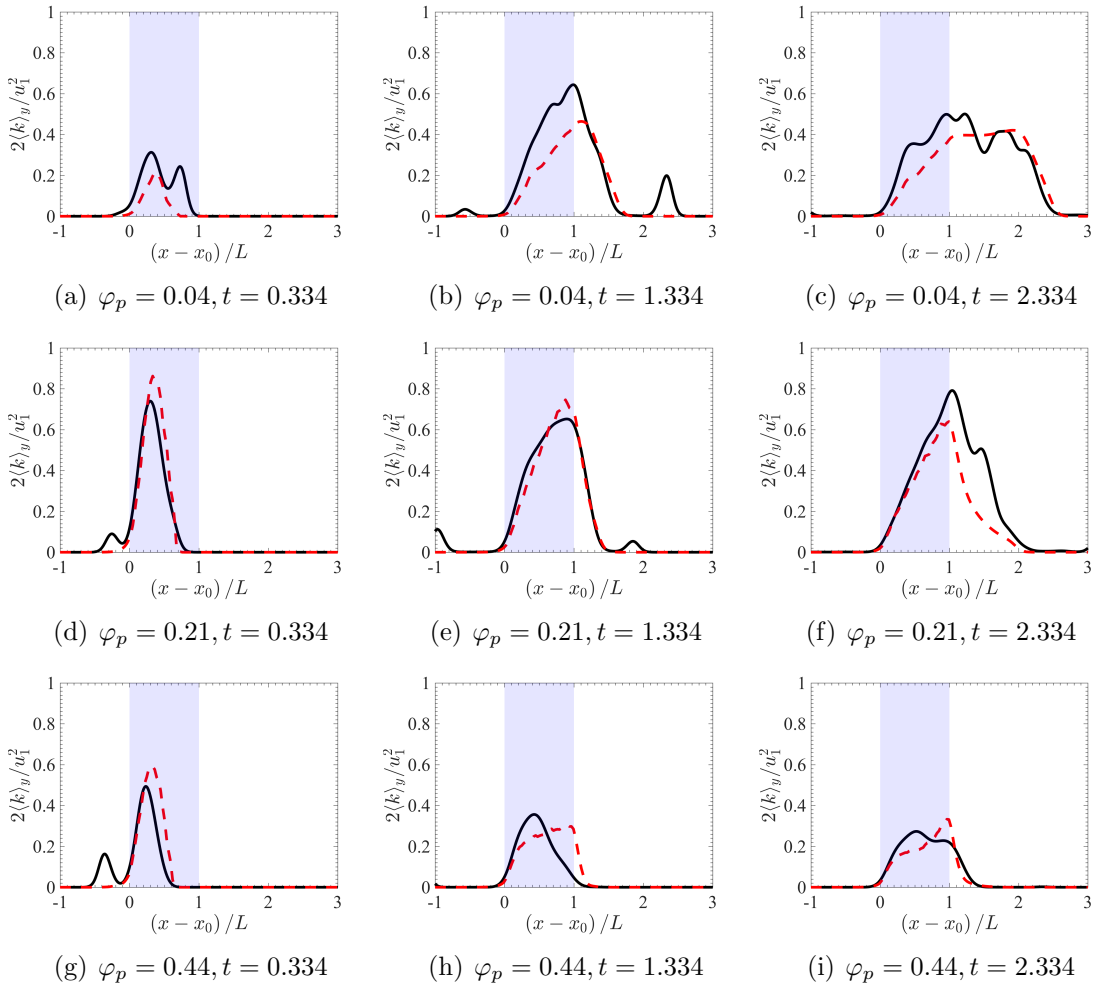

(a) $\varphi_p = 0.04, t = 0.334$ (b) $\varphi_p = 0.04, t = 1.334$ (c) $\varphi_p = 0.04, t = 2.334$

(d) $\varphi_p = 0.21, t = 0.334$ (e) $\varphi_p = 0.21, t = 1.334$ (f) $\varphi_p = 0.21, t = 2.334$

(g) $\varphi_p = 0.44, t = 0.334$ (h) $\varphi_p = 0.44, t = 1.334$ (i) $\varphi_p = 0.44, t = 2.334$

Figure 5.10: Comparison of PTKE from filtered DNS (—) and VF-EL (- - -) with $\delta_f = 4d_p$. Coefficients of $C_f = 0.25$, 5.0, and 15.0 were used for $\varphi_p = 0.04$, 0.21, and 0.44, respectively. The shaded region (▯) indicates particle location.

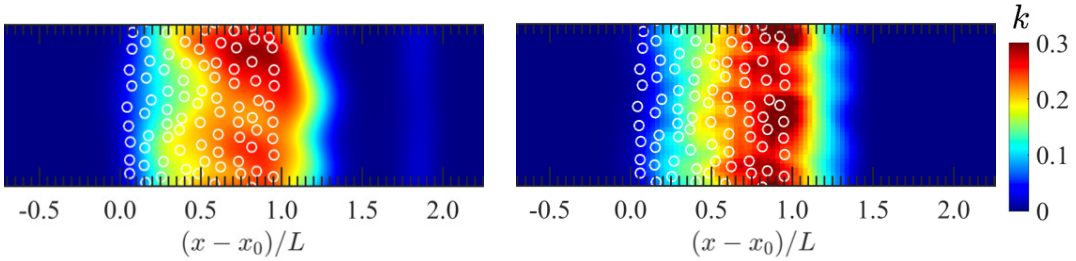

(a) Filtered DNS (b) VF-EL

Figure 5.11: Instantaneous snapshot of PTKE from the two-dimensional VF-EL with $\varphi_p = 0.21$ at $t = 1.334$.

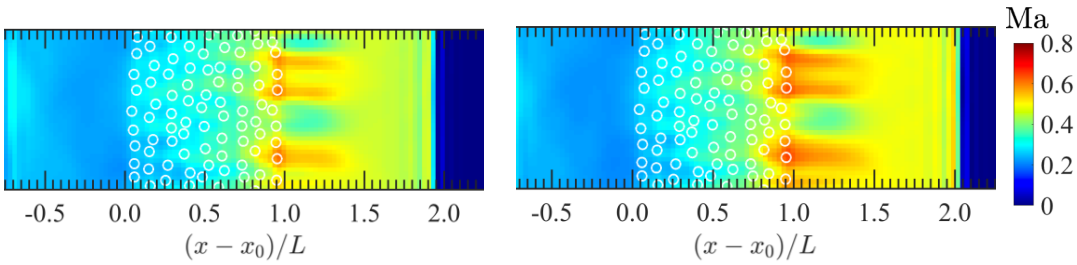

(a) VF-EL without PTKE

(b) VF-EL with PTKE

Figure 5.12: Instantaneous snapshot of local Mach number from the two-dimensional VF-EL with $\varphi_p = 0.21$ at $t = 1.334$.

Ma_s	Shock Mach number	1.22	1.66	3.00
ρ_1	Post-shock density	1.376	2.131	3.857
p_1	Post-shock pressure	1.121	2.177	7.381
u_1	Post-shock velocity	0.334	0.881	2.222
φ_p	Mean volume fraction	0.10	0.19	
N_p	Number of particles	200	400	
		DNS [152]	VF-EL	
	Grid Resolution	$\sim 16 - 18 \times 10^6$ tetrahedral cells	$131 \times 10 \times 10$	

Table 5.2: Parameters used in the three-dimensional shock-particle simulations. All simulations are performed with pre-shock conditions of $\rho_2 = 1$, $p_2 = 0.714$, and $u_2 = 0$. VF-EL is performed with $\delta_f = 4d_p$ and $\Delta x = d_p$. Further details on the DNS can be found in Mehta et al. [150, 151, 153, 152].

5.3.5 Modeling PTKE in a three-dimensional shock-particle configuration

In this section, the results obtained from VF-EL are compared against the three-dimensional particle-resolved simulations of Mehta et al. [152]. Simulations are performed for three shock Mach numbers: $\mathrm{Ma}_s = 1.22$, 1.66, and 3.00, and two mean particle volume fractions: $\varphi_p = 0.10$ and 0.19. Particles of size $d_p^\star = 100$ µm are randomly distributed over a length of $L^* = 1.7\,\mathrm{mm}$ in a shock tube with a cross section of $L_y^\star \times L_z^\star = 0.8\,\mathrm{mm} \times 0.8\,\mathrm{mm}$. Particles are taken to be stationary with the same

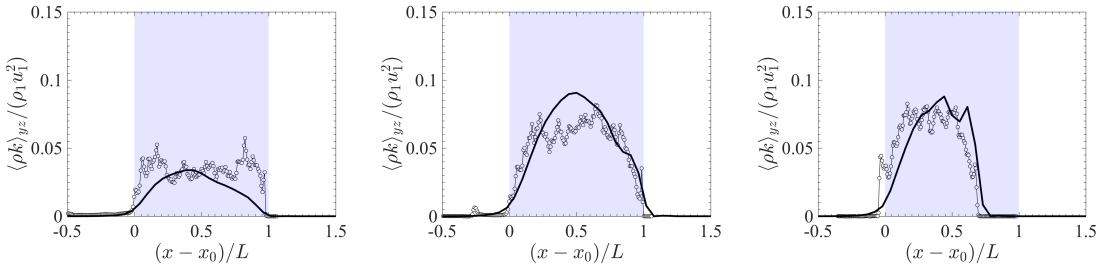

(a) $\varphi_p = 0.10$, $\mathrm{Ma}_s = 1.22$ (b) $\varphi_p = 0.10$, $\mathrm{Ma}_s = 1.66$ (c) $\varphi_p = 0.10$, $\mathrm{Ma}_s = 3.00$

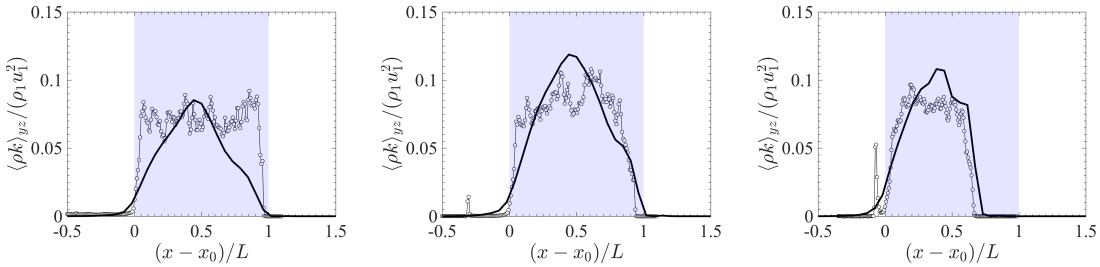

(d) $\varphi_p = 0.19$, $\mathrm{Ma}_s = 1.22$ (e) $\varphi_p = 0.19$, $\mathrm{Ma}_s = 1.66$ (f) $\varphi_p = 0.19$, $\mathrm{Ma}_s = 3.00$

Figure 5.13: Averaged $\rho k = \mathrm{tr}(\boldsymbol{R}_u)/2$ obtained from DNS [152] (-o-) and VF-EL (—) as a function of Mach number and volume fraction. $\mathrm{Ma}_s = 1.22$ evaluated at $t = 0.818$, $\mathrm{Ma}_s = 1.66$ at $t = 0.620$, and $\mathrm{Ma}_s = 3.00$ at $t = 0.237$. The shaded region ( ) indicates particle location.

material properties described in the previous section. A uniform grid is employed in VF-EL such that $\Delta x = d_p$ with $\delta_f = 4d_p$. The integral length scale appearing in the dissipation model (5.3) is taken to be $\mathcal{L} = d_p$. A summary of the simulation parameters can be found in Table 5.2. It should be noted that the plots are normalized by post-shock conditions, which vary for different shock Mach numbers. Due to the availability of DNS data, comparisons are only performed at early times prior the transmitted shock passing through the particle suspension.

In order to accurately predict the distribution of pseudo-turbulent Reynolds stresses, appropriate values of C_f must be chosen. The values of C_f are determined by finding the best fit for $\rho k = \mathrm{tr}(\boldsymbol{R}_u)/2$ (see Fig. 5.13). Even with $\mathcal{O}(10^3)$ reduction in resolution compared to the DNS, the PTKE predicted by VF-EL exhibits overall excellent agreement with the DNS for the range of shock Mach numbers and volume fractions

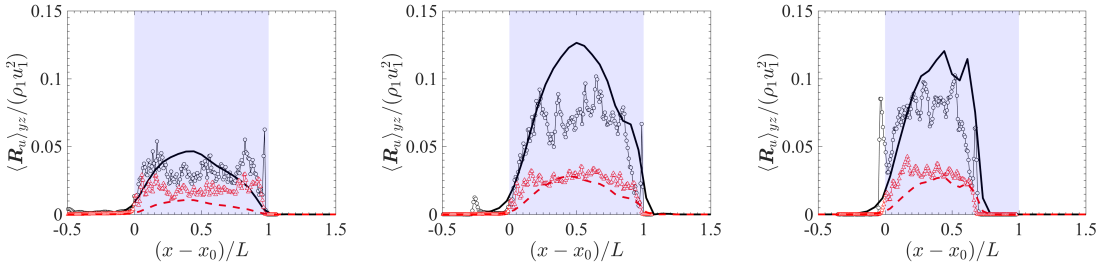

(a) $\varphi_p = 0.10$, $\mathrm{Ma}_s = 1.22$ (b) $\varphi_p = 0.10$, $\mathrm{Ma}_s = 1.66$ (c) $\varphi_p = 0.10$, $\mathrm{Ma}_s = 3.00$

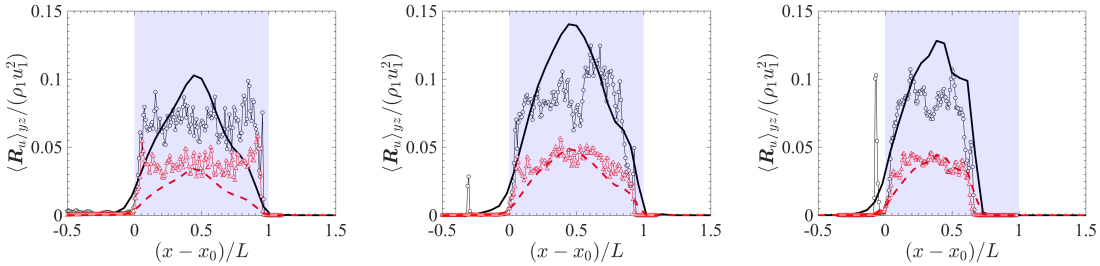

(d) $\varphi_p = 0.19$, $\mathrm{Ma}_s = 1.22$ (e) $\varphi_p = 0.19$, $\mathrm{Ma}_s = 1.66$ (f) $\varphi_p = 0.19$, $\mathrm{Ma}_s = 3.00$

Figure 5.14: Components of the pseudo-turbulent Reynolds stress obtained from DNS [152] (symbols) and VF-EL (lines) as a function of Mach number and volume fraction. $\mathrm{Ma}_s = 1.22$ evaluated at $t = 0.818$, $\mathrm{Ma}_s = 1.66$ at $t = 0.620$, and $\mathrm{Ma}_s = 3.00$ at $t = 0.237$. DNS $R_u(1,1)$ (-○-), DNS $(R_u(2,2) + R_u(3,3))/2$ (-△-), VF-EL $R_u(1,1)$ (—), and VF-EL $(R_u(2,2) + R_u(3,3))/2$ (- - -). The shaded region (▪) indicates particle location.

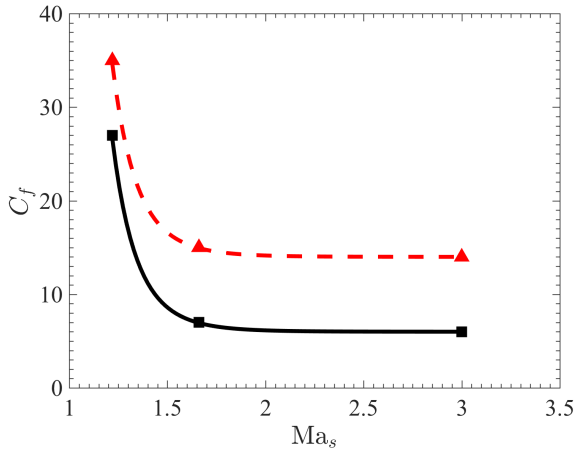

Figure 5.15: Coefficient appearing in the dissipation model (5.3) for three-dimensional simulations. Values extracted from $\varphi_p = 0.10$ (■) and $\varphi_p = 0.20$ (▲). Power-law fits for $\varphi_p = 0.10$ (—) and $\varphi_p = 0.19$ (- - -) given by $C_f = 150\mathrm{Ma}_s^{-10} + 83\varphi_p - 2$.

under consideration. Perhaps surprisingly, the largest discrepancies are observed in the lowest Mach number case. In addition, the algebraic model used to reconstruct the separate components of the pseudo-turbulent Reynolds stress is able to predict the level of anisotropy reasonably well, despite it being developed for incompressible flows (see Fig. 5.14). In general, the Reynolds stresses increase with increasing volume fraction and shock Mach number.

As was seen in the two-dimensional simulations, C_f increases with increasing volume fraction. The magnitude of the Reynolds stresses were found to be smaller in three dimensions, consistent with previous work [152], and consequently the magnitude of C_f is larger. Here, it was found that C_f increases with decreasing shock Mach number according to $C_f = 150\mathrm{Ma}_s^{-10} + 83\varphi_p - 2$. (see Fig. 5.15). This could indicate that contributions that are lumped into the dissipation model are more significant at lower shock Mach numbers relative to the drag production term.

As noted earlier, the drag correlation of Gidaspow [69] was used due to its applicability at high Reynolds numbers and volume fractions. The effect of different

drag correlations on the pseudo-Reynolds stresses are reported in B.3. It is found that the modeling coefficient, C_f, changes with drag law; however, the distribution of Reynolds stresses remain unchanged. Further analysis is required to model C_f over a wider range of conditions. For example, based on the work of Osnes et al. [171], C_f will also likely depend on d_p. In conclusion, given an adequate model for C_f, the transport equation proposed here is capable of accurately predicting the distribution of PTKE (irrespective of the drag law employed). In the present work, C_f was fit to particle-resolved simulations of stationary particles, and is thus limited to applications of fixed particles under the volume fractions and Mach numbers considered here. Future work is needed to extend this approach to include a physics-based model for dissipation.

5.4 Conclusions

In this work, we extend the volume-filtered formulation of Anderson and Jackson [6] to compressible two-phase flows. It was demonstrated that the energy equation requires special consideration. In particular, it is shown that alternative approaches can be taken during the derivation, resulting in different closure problems. A key outcome of the volume-filtered formulation is the appearance of the pseudo-turbulent kinetic energy (PTKE) in the state equation for pressure. It was shown that PTKE acts to systematically reduce the gas-phase pressure, and consequently increase the local Mach number.

Particle-resolved simulations of shock-particle interactions were performed to quantify the relative importance of unclosed terms via an *a posteriori* filtering approach consistent with the volume-filtered formulation. The relative importance of the unclosed terms appearing in the equations were shown to depend on the discretization employed, quantified by varying the filter size, δ_f. For sufficiently large filter sizes, ($\delta_f > 4d_p$), the majority of velocity fluctuations reside at the sub-filter scale. In

general, PTKE was seen to depends on both δ_f and volume fraction. It was demonstrated that the PTKE dependence can be collapsed to a Knudsen number based on the mean inter-particle spacing.

A transport equation for the PTKE was then derived, which contains a production term proportional to the local drag force and slip velocity magnitude, and a dissipation rate that requires closure. Dissipation was modeled using an integral length scale proportional to the particle diameter in addition to a velocity scale that depends on the local slip velocity when particles are present and the square of PTKE in regions void of particles. An algebraic model was employed to reconstruct the components of the pseudo-turbulent Reynolds stress.

The volume-filtered equations of motion were implemented within a high-order Eulerian–Lagrangian framework that admits convergence under grid refinement. A constant appearing in the dissipation rate was fit over a range of volume fractions and Mach numbers in both two-dimensional and three-dimensional shock-particle configurations. The Eulerian–Lagrangian approach was shown to be capable of predicting the distribution of pseudo-turbulent Reynolds stresses with the correct level of anisotropy.

In summary, the present study provides a framework to develop new models, beyond traditional ensemble averaging. While the present work focused on stationary particles, new models are needed to incorporate the effect of PTKE on particle dispersion. With the increasing availability of particle-resolved simulation data coming online (e.g., [238, 152, 171]), further improvements to the model can be made.

CHAPTER VI

Eulerian–Lagrangian Simulations of Plume-Surface Interactions

6.1 Introduction

The ejection of granular matter by rocket plumes during planetary landing poses serious challenges to future space missions. During landing, rocket exhaust can interact with a planetary surface, otherwise known as plume-surface interactions (PSI). These events lead to flow induced stresses which lift and eject loose granular matter [148]. Subsequent particle ejections can result in serious damage by colliding with the spacecraft, inhibit visibility, and spoof sensors during landing [24, 166]. To characterize and model this phenomenon, experimental and numerical studies have been performed on granular beds. See Chapter I for details and findings related to PSI.

Over the years, a myriad of studies have been performed for single-phase compressible jet impingement [216, 37, 101, 116, 112, 77, 253, 139]. These works typically involve sonic and supersonic jets impinging on a flat surfaces; however, other geometries for the impinging wall are also considered. This includes but is not limited to concave and convex surfaces [216, 139], inclined planes [216, 116], wedges [115], and conical shapes [96]. These studies are performed to determine the effect of surface geometry during impingement such as variations flow structures and changes in

surface pressure distributions. Generally, it is found that coherent near nozzle structures can be described by inviscid flow behavior [96]; however, near wall variations are influenced by boundary layer development [115] and the presence of geometric obstacles [216].

Visualization, methods like shadowgraph and Schlieren imaging are typically used to provide information on the presence of compressible flow structures. For detailed flow analysis, particle image velocimetry (PIV) [112, 77] has been used to capture velocity fluctuations for different impingement heights. When combined with acoustic measurements, it is found that coherent tone production is dependent on impingement height and nozzle conditions. Other methods like planar laser-induced florescence (PLIF) [253] are used to capture compressible flow structures in vacuum conditions. This technique provides clarity regarding variations in surface pressure measurements during impingement where distribution variations, or lack thereof, depend on jet conditions and impingement height. While out of the scope of this work, high quality reviews also exist for incompressible gas phase [138, 95, 248] and fluid phase [252] impingement for the interested reader.

In this chapter, simulations are performed for jet impingement on flat surfaces and a granular bed. To start, the numerical methods are introduced. This includes references to the immersed boundary method as well as guidance to set up initial conditions for the nozzle geometry. Following, numerical simulations of single-phase jet impingement are performed. Comparisons are made against experimental setups with different impingement heights and nozzle pressure ratios (NPR), defined as the ratio between stagnation pressure and ambient pressure. First, comparisons are made against the digital particle image velocimetry (DPIV) data presented in [77]. This includes information on centerline velocity as well as mean velocity magnitudes of the impinging jet. Second, surface pressure values are compared to the results from Snedeker et al. [216]. After performing validation, preliminary work for jet

impingement on granular beds is shown using the Eulerian–Lagrangian framework presented in Chapter III.

6.2 Governing equations

6.2.1 Fluid-phase equations

The fluid phase equations of motion for conservation of mass, momentum, and energy are as follows,

$$\frac{\partial \alpha\rho}{\partial t} + \nabla \cdot (\alpha\rho \boldsymbol{u}) = 0, \tag{6.1}$$

$$\frac{\partial \alpha\rho \boldsymbol{u}}{\partial t} + \nabla \cdot (\alpha\rho \boldsymbol{u} \otimes \boldsymbol{u}) = \alpha\nabla \cdot (\boldsymbol{\tau} - p\mathbb{I}) + \boldsymbol{\mathcal{F}} - \frac{\rho \boldsymbol{\delta}_g}{\mathrm{Fr}_c}, \tag{6.2}$$

$$\begin{aligned} \frac{\partial \alpha\rho E}{\partial t} + \nabla \cdot (\alpha \boldsymbol{u} \{\rho E + p\} - \alpha \boldsymbol{u} \cdot \boldsymbol{\tau}) = &- \alpha\nabla \cdot \boldsymbol{q} - (p\mathbb{I} - \boldsymbol{\tau}) : \nabla (\alpha_p \boldsymbol{u}_p) \\ &+ \boldsymbol{u}_p \cdot \boldsymbol{\mathcal{F}} + \mathcal{Q} - \frac{\rho \boldsymbol{\delta}_g \cdot \boldsymbol{u}}{\mathrm{Fr}_c} \end{aligned} \tag{6.3}$$

where the equation of state is given by,

$$T = \frac{\gamma p}{(\gamma - 1)\rho} \quad \text{and} \quad p = (\gamma - 1)\left(\rho E - \frac{1}{2}\rho \boldsymbol{u} \cdot \boldsymbol{u}\right). \tag{6.4}$$

Due to non-dimensionalization, the effects of gravitational acceleration is implemented in terms of Froude number based off of the reference speed of sound, given by $\mathrm{Fr}_c = c_\infty^{\star 2}/(g^\star L^\star)$, where $g^\star$ is the dimensional acceleration due to gravity. The direction of gravity is defined by $\boldsymbol{\delta}_g$ which acts in the positive x-direction, or $\boldsymbol{\delta}_g = [1\ 0\ 0]^\intercal$. Gravitational effects are neglected for single-phase jet impingement cases.

6.2.2 Particle-phase description

The complete description and implementation of the particle phase transport equations can be found in Section 3.1.2. For the described particle simulation, the implementation has been extended to account for additional particle forces and rotation.

The particle equations of motion are given by

$$\frac{\mathrm{d}\boldsymbol{x}_p^{(i)}}{\mathrm{d}t} = \boldsymbol{v}_p^{(i)}, \tag{6.5}$$

$$m_p \frac{\mathrm{d}\boldsymbol{v}_p^{(i)}}{\mathrm{d}t} = \mathcal{V}_p \nabla \cdot (-p\mathbb{I} + \boldsymbol{\tau}) + \boldsymbol{f}_{\mathrm{drag}}^{(i)} + \boldsymbol{f}_{\mathrm{col}}^{(i)} + \boldsymbol{f}_g^{(i)} + \boldsymbol{f}_{\mathrm{lift}}^{(i)}, \tag{6.6}$$

and

$$I_p \frac{\mathrm{d}\boldsymbol{\omega}_p^{(i)}}{\mathrm{d}t} = \sum_j \frac{d_p}{2} \boldsymbol{n}_{ij} \times \boldsymbol{f}_{t,j\to i}^{\mathrm{col}}, \tag{6.7}$$

where $\boldsymbol{x}_p^{(i)}$, $\boldsymbol{v}_p^{(i)}$, and $\boldsymbol{\omega}_p^{(i)}$ are the i-th particle position, velocity, and angular velocity respectively. Other quantities include the particle mass m_p, the moment of inertia for a sphere given by $I_p = m_p d_p^2/10$, and $\boldsymbol{n}_{ij}$ the outward normal vector from particle i to particle j.

In Eq. (6.6), force contributions include resolved stresses, drag $\boldsymbol{f}_{\mathrm{drag}}^{(i)}$ given by Eq. (3.7), collisions $\boldsymbol{f}_{\mathrm{col}}^{(i)}$, the force of gravity, $\boldsymbol{f}_g^{(i)}$, and lift, $\boldsymbol{f}_{\mathrm{lift}}^{(i)}$. The force due to gravitational effects is given by $\boldsymbol{f}_g^{(i)} = m_p^{(i)} \rho \boldsymbol{\delta}_g / \mathrm{Fr}_c$. Lift contributions are modeled using an extension to the traditional Saffman lift [200], proposed by McLaughlin et al. [145]. This is given by

$$\boldsymbol{f}_{\mathrm{lift}}^{(i)} = \frac{9.69\sqrt{\rho\mu}}{\pi \rho_p d_p} \frac{(\boldsymbol{u} - \boldsymbol{v}_p^{(i)}) \times \boldsymbol{\omega}}{\sqrt{|\boldsymbol{\omega}|}}, \tag{6.8}$$

where $\boldsymbol{\omega} = \nabla \times \boldsymbol{u}$ is the vorticity. As was previously mentioned in Section 3.1.2, the particle equations are non-dimensionalized using the same reference quantities for in Eqs. (2.1)–(6.4). Note that the additional lift force leads to a modification to the projection of interphase momentum exchange, $\boldsymbol{\mathcal{F}}$, from Eq. (6.9) and work due to interphase momentum exchange, $\boldsymbol{u}_p \cdot \boldsymbol{\mathcal{F}}$, from Eq. (6.10). These modified expressions are given by,

$$\boldsymbol{\mathcal{F}} = -\sum_{i=1}^{N_p} \mathcal{G}\big(|\boldsymbol{x} - \boldsymbol{x}_p^{(i)}|\big) \left(\boldsymbol{f}_{\mathrm{drag}}^{(i)} + \boldsymbol{f}_{\mathrm{lift}}^{(i)} \right) \tag{6.9}$$

and

$$\boldsymbol{u}_p \cdot \boldsymbol{\mathcal{F}} = -\sum_{i=1}^{N_p} \mathcal{G}\left(|\boldsymbol{x} - \boldsymbol{x}_p^{(i)}|\right) \boldsymbol{v}_p^{(i)} \cdot \left(\boldsymbol{f}_{\text{drag}}^{(i)} + \boldsymbol{f}_{\text{lift}}^{(i)}\right). \tag{6.10}$$

Normal and tangential collisions are treated using the soft-sphere model proposed by Cundall and Strack [47] and expanded for high speed collisions in Capecelatro and Desjardins [34]. For notation, see Fig. 6.1. As two particles come in contact a force is created given by,

$$\boldsymbol{f}_{n,j\to i}^{\text{col}} = \begin{cases} -k\delta_{ij}\boldsymbol{n}_{ij} - \zeta \boldsymbol{v}_{ij,n} & \text{if } \ s < 0, \\ 0 \quad \text{else}, \end{cases} \tag{6.11}$$

where s is the distance between the particle surfaces, δ_{ij} is the overlap between the particles, $\boldsymbol{n}_{ij}$ is the unit normal vector from particle i to particle j and $\boldsymbol{v}_{ij,n}$ is the normal relative velocity between particles i and j. The spring stiffness and damping parameter are given by k and ζ, respectively. A model for the damping parameter [47] uses a coefficient of restitution $0 < \text{e} < 1$ such that

$$\zeta = -2\ln \text{e} \frac{\sqrt{km_p/2}}{\sqrt{\pi^2 + (\ln \text{e})^2}}. \tag{6.12}$$

The spring stiffness is related to the collision time, τ_{col}, according to

$$k = m_p/2\tau_{\text{col}}^2 \left(\pi^2 + (\ln \text{e})^2\right). \tag{6.13}$$

For the purposes of this work a coefficient of restitution of e=0.85 is used. To resolve the collisions, τ_{col} is set to be 30 times the simulation time step Δt for the presented simulation.

The rotation of each and every particle is tracked using Eq. (6.7) and is a consequence of tangential collisional forces, $\boldsymbol{f}_{t,j\to i}^{\text{col}}$. To account for friction between particles, a static frictional model for the tangential component of the collision force is

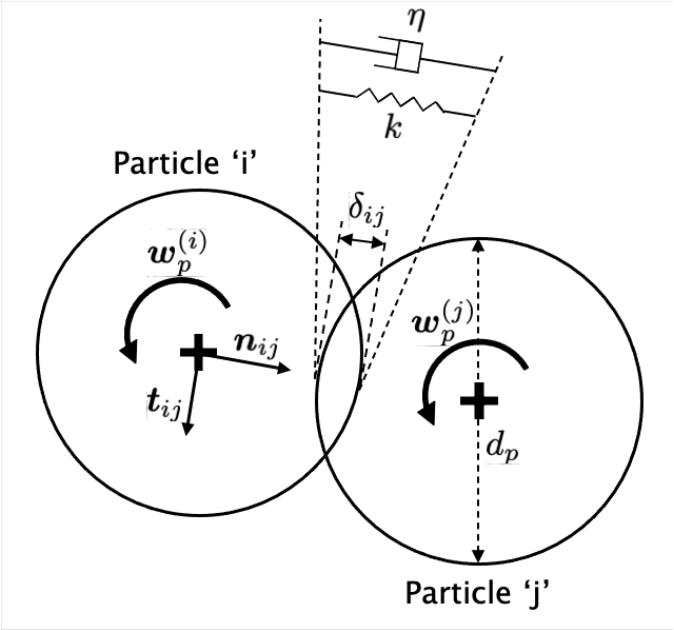

Figure 6.1: Diagram of inter-particle collisions. Image was adapted from Capecelatro and Desjardins [34] and modified for the presented notation.

employed,

$$\boldsymbol{f}^{\text{col}}_{t,j\to i} = -\mu_f \left|\boldsymbol{f}^{\text{col}}_{n,j\to i}\right| \boldsymbol{t}_{ij}, \tag{6.14}$$

where $\mu_f = 0.1$ is the coefficient of friction and $\boldsymbol{t}_{ij}$ is the tangential unit vector. Once each individual collision force is computed, the full collision force that particle i experiences can be expressed as

$$\boldsymbol{f}^{(i)}_{\text{col}} = \sum_{j\neq i} \left(\boldsymbol{f}^{\text{col}}_{n,j\to i} + \boldsymbol{f}^{\text{col}}_{t,j\to i}\right). \tag{6.15}$$

For additional details on the equations and implementation for inter-particle collisions, refer to Capecelatro and Desjardins [34].

6.3 System description

See Fig. 6.2 for an example of the simulation setup. For all cases, domain size is varied by the impingement height whereby $L_x \times L_y \times L_z = (h_x + h) \times 40D_N \times 40D_N$,

where h and h_x are the total nozzle length and impingement height respectively. Grid stretching is used such that a uniform resolution of $D_N/\Delta x = 40$ is present in a region of $x \times y \times z = (h_x + h) \times 10D_N \times 10D_N$ surrounding the nozzle. Past this region, the grid resolution in the y- and z-directions slowly transitions to $D_N/\Delta x = 4$. Simulations are performed in air, whereby the ratio of specific heats is $\gamma = 1.4$.

The impinging surface for single-phase studies is simulated using an immersed boundary with no-slip, no-penetration boundary conditions on velocity and Neumann conditions on scalars. Farfield conditions with sponge zones are applied at the remaining the boundaries.

For jet impingement on a granular bed, a slip-boundary condition is used for the impinging surface while farfield conditions with sponge zones are applied to remaining boundaries. For the disperse phase, $d_p = 0.015748$ monodisperse particles, corresponding to a dimensional diameter of $400\,\mu\text{m}$, are used. These particles have a density ratio of $\rho_p/\rho = 2520$ with a filter size of $\delta_f = 4\,d_p$. Interphase heat transfer is used, whereby $C_{p,p} = 0.8375$. Drag is modeled using the Gidaspow correlation with the corresponding volume fraction correction [69].

To generate the granular bed, particles are uniformly distributed in a domain with a mean volume fraction of $\phi_p = 0.40$. After settling under gravity, with $\text{Fr}_c = 472448$, which corresponds to the gravitation on Earth, the particles reach closed packing with a volume fraction of $\phi_p = 0.63$ and a bed height of $h_b/D_N \approx 1$. At this point, the ~ 27.6 million particle bed is used in the simulation.

6.4 Numerics

To simulate the single-phase impinging jet and multi-phase PSI, a fourth order centered finite difference scheme is used in combination with SAT boundary conditions. A description of the implementation is included in Section 3.2 and further comments on the scheme can be found in Vishnampet Ganapathi Subramanian [247].

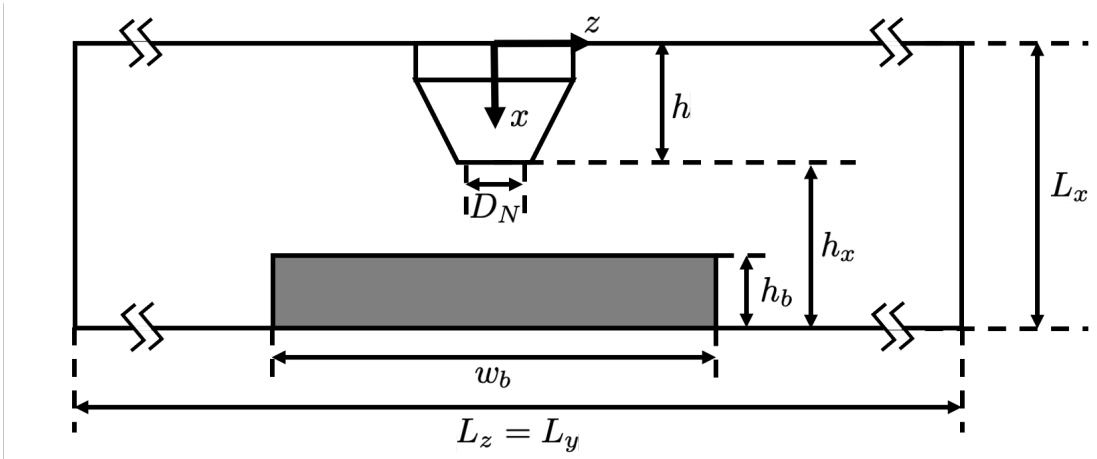

Figure 6.2: Nozzle configuration for jet impingement.

For added nonlinear stability under low Mach number regimes and local kinetic energy preservation, a skew-symmetric-type splitting scheme is applied to the inviscid flux. Details can be found in Pirozzoli [188]. Here, this splitting method is extended to particle-laden flows through the addition of volume fraction, given by

$$\nabla \cdot (\alpha\rho\boldsymbol{u}\varphi) = \frac{1}{2}\nabla \cdot (\alpha\rho\boldsymbol{u}\varphi) + \frac{1}{2}\varphi_s \nabla \cdot (\alpha\rho\boldsymbol{u}) + \frac{1}{2}\alpha\rho\boldsymbol{u} \cdot \nabla\varphi, \tag{6.16}$$

where φ is a general scalar which is equal to unity for the continuity equation, $\boldsymbol{u}$ for the momentum equation, and $H = E + p/\rho$ for the energy equation. To account for large discontinuities, i.e. in the presence of shocks, localized artificial dissipation is added [45, 136, 26]. Details on the artificial dissipation implementation can be found in Yao et al. [256].

6.4.1 Nozzle geometry and initial conditions

To simulate the nozzle geometry, the CBVP approach proposed in Chapter IV is used. See Eqs. (4.8) - (4.10) for the equations of motion for the described method. These equations allow for the application of no-slip and no-penetration conditions on velocity and Neumann conditions on scalars. Here all contributions apart from the

unsteady term in Eqs. (6.1) - (6.3), account for the RHS terms. For this study a sharp immersed boundary interface, with $\epsilon = 0$, is used.

Figure 6.3 shows a schematic of the converging nozzle considered in the present work. The nozzle shape is analytically defined using a levelset function. This provides information of the nozzle's surface, the local unit normal vector field, and surface curvature required for the described immersed boundary method. Additional details can be found in Section 4.3. Initial conditions for the interior of the nozzle are calculated based on the area relations for Mach number and pressure ratio given by,

$$\left(\frac{A_{in}}{A^*}\right)^2 = \frac{1}{\mathrm{Ma_{in}}^2}\left[\frac{2}{\gamma+1}\left(1+\frac{\gamma-1}{2}\mathrm{Ma_{in}}^2\right)\right]^{(\gamma+1)/(\gamma-1)}, \tag{6.17}$$

and

$$\frac{A^*}{A_{in}} = \frac{\left[1-\left(\frac{p_{in}}{p_o}\right)^{(\gamma-1)/\gamma}\right]^{1/2}\left(\frac{p_{in}}{p_o}\right)^{1/\gamma}}{\left(\frac{\gamma-1}{2}\right)^{1/2}\left(\frac{2}{\gamma+1}\right)^{(1/2)(\gamma+1)/(\gamma-1)}}. \tag{6.18}$$

Here, the subscripts 'o' and 'in' indicate stagnation and inlet conditions respectively while the superscript '$*$' indicates exit conditions for a critical choked area. Using the described nozzle geometry, where the the inlet ($A_{in} = \pi D_{in}^2/4$) and exit ($A^* = \pi D_N^2/4$) cross sectional areas are known, one can solve for the corresponding inlet Mach number, $\mathrm{Ma_{in}}$, and pressure ratio, p_{in}/p_o. The associated temperature, pressure, and density for the inlet are found using isentropic relations. The inlet velocity is then calculated via Mach number given by,

$$u_{in} = \sqrt{\frac{\gamma p_{in}}{\rho_{in}}}\mathrm{Ma}_{in}. \tag{6.19}$$

The flow quantities for the inlet are initialized on the interior bore of the nozzle from $x = 0$ to $x = h_s$, where h_s is the straight length of the nozzle, and radially from $r = 0$ to $r = \pm D_{in}/2$. Upon starting a simulation, these conditions are allowed to develop

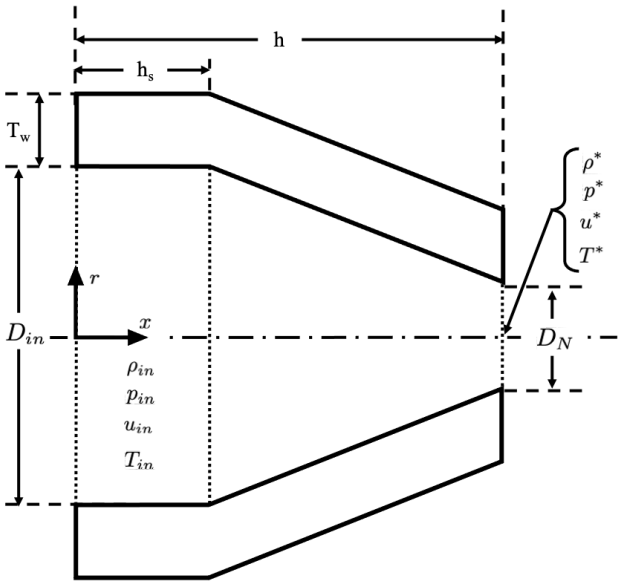

Figure 6.3: Nozzle geometry used for analytical levelset information.

in the nozzle leading to a sonic exit condition.

6.5 Single-phase jet impingement validation

In this section numerical simulations of under-expanded jet impingement are performed on flat plates for different NPR and impingement heights. Simulation results are compared to data in literature for validation purposes. This includes comparisons against mean velocity magnitude and centerline velocity data from Henderson et al. [77] and impingement surface pressure measurements from Snedeker et al. [216]. A constant CFL = 0.5 is used to govern the timestep size for the following cases.

6.5.1 Mean velocity magnitude and centerline velocity comparison

In Henderson et al. [77], digital particle imaging velocimetry (DPIV) and shadowgraph imaging are used to study jet impingement. For all cases, a nozzle with a 30° converging section and a dimensional exit diameter of $D_N^* = 25.4\,\text{mm}$ is used. This

exit diameter is taken as the reference length scale, resulting in non-dimensional exit diameter equal to unity. For simulations, the following nozzle geometry parameters are used; $D_{in} = 2.2547$, $D_N = 1.0$, $h = 1.5$, $h_s = 0.5$, and $T_w = 0.5$. See Fig. 6.3 for a reference nozzle geometry. Three impingement heights are considered in this exercise; $h_x/D_N = 2.08$, $h_x/D_N = 3.65$, and $h_x/D_N = 4.16$. Using the equations described in Section 6.4.1, the non-dimensional exit pressure, temperature, and velocity for a NPR = 4.03 sonic nozzle are given by $p^* = 1.5207$, $T^* = 2.0833$, and $u^* = 0.9129$ respectively. Under the described conditions, the reference Reynolds number is $\mathrm{Re}_c = 577003$. Simulations are run until steady state, approximately 20 flow through times. Following, data is averaged to compare against experimental results.

For an impingement height of $h_x/D_N = 2.08$, contours of mean velocity magnitudes are shown in Fig. 6.4(a). Results match well when compared to experimental data with minor differences emerging at Mach disk and near-wall region. For the corresponding centerline velocity plots, shown in Fig. 6.4, results agree from $x/D_N = 0$ to $x/D_N = 1$. Following the formation of the Mach disk at $x/D_N = 1$, there are noticeable over- and under-predictions in velocity which persist for long time averages. This leads to the lack of the recirculation behavior that is described in Henderson et al. [77]. A similar trend exists for larger impingement heights. The velocity magnitude plots, shown in Figs. 6.4(b) and 6.4(c), match experimental data for near nozzle behavior; however, differences in contours emerge near the impinging surface. The same holds for the mean centerline velocity plots for the larger impingement heights, shown in Figs. 6.5(b) and 6.5(c).

Compared to $h_x/D_N = 2.08$, numerical simulations with $h_x/D_N = 3.65$ and $h_x/D_N = 4.16$ are extremely oscillatory. This behavior leads to errors associated with velocity measurements and the absence of recirculation for all simulations. That being said, all cases apart from $h_x/D_N = 4.16$ were described to be "unsteady" in Henderson

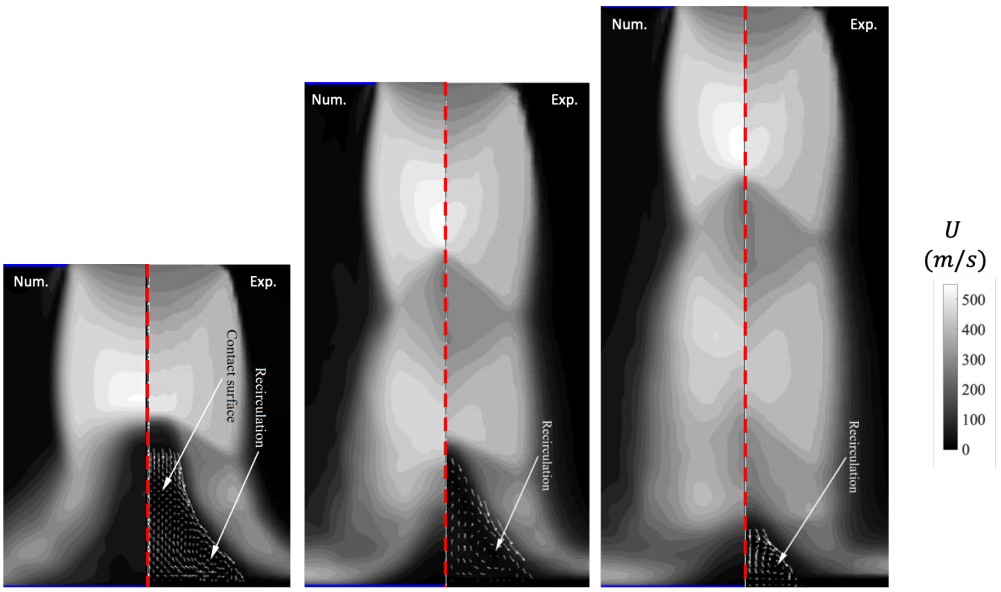

(a) $h_x/D_N = 2.08$ (b) $h_x/D_N = 3.65$ (c) $h_x/D_N = 4.16$

Figure 6.4: Mean velocity magnitude contours for (a) $h_x/D_N = 2.08$, (b) $h_x/D_N = 3.65$, and (c) $h_x/D_N = 4.16$ with $NPR = 4.03$, $D/\Delta x = 40$, and a lip thickness of $0.5\,D$. Results on the left of each image are the time-averaged numerical results while results on the right are images courtesy of Henderson et al. [77].

et al. [77]. Because there is a large emphasis on acoustic analysis in Henderson et al. [77], this distinction is believed to be linked to the radiated pressure waves and not necessarily the oscillatory nature of the flow itself. As a result, additional cases are required to evaluate the behavior of the jet for future work.

6.5.2 Surface pressure comparison

In Snedeker et al. [216], Schlieren imaging and impingement surface pressure measurements are analyzed for a wide range of NPR and impingement heights. For this case, a converging nozzle with a dimensional exit diameter of $D_N^* = 0.511\,\text{in}$ is used. As previously described, this dimensional exit diameter is used as the reference length scale resulting in a reference non-dimensional exit diameter equal to unity. The nozzle is simulated using the following nozzle geometry parameters; $D_N = 1.0$, $D_{in} = 3.333$,

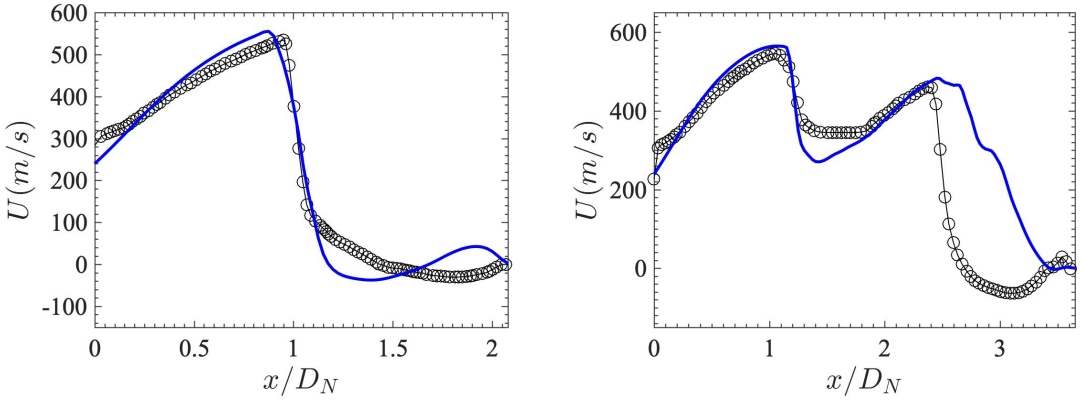

(a) $h_x/D_N = 2.08$

(b) $h_x/D_N = 3.65$

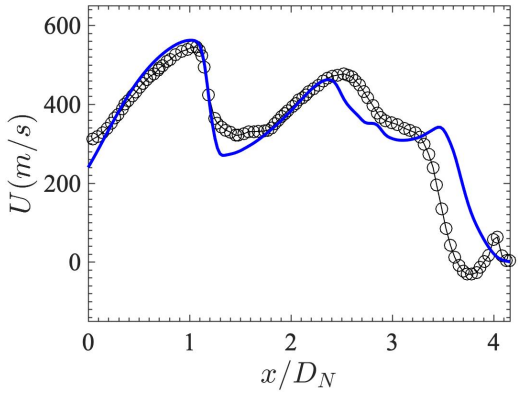

(c) $h_x/D_N = 4.16$

Figure 6.5: Mean centerline velocity plots for (a) $h_x/D_N = 2.08$, (b) $h_x/D_N = 3.65$, and (c) $h_x/D_N = 4.16$ with $NPR = 4.03$. Numerical data is indicated by (—) while experimental data from Henderson et al. [77] is indicated by (-o-).

$h = 1.5$, $h_s = 0.5$, and $T_w = 0.5$. See Fig. 6.3 for a reference nozzle geometry. For this work, normalized surface pressure measurements are compared to experimental data for NPR = 2.69 and impingement height of $h_x/D_N = 1.96$. For a pressure ratio of NPR = 2.69, the non-dimensional exit pressure, temperature, and velocity conditions for a sonic nozzle are given by $p^* = 1.0144$, $T^* = 2.0833$, and $u^* = 0.9129$ respectively. Given the described parameters, the reference Reynolds number is $\mathrm{Re}_c = 294849$. Simulations are run until steady state, approximately 20 flow through times. Following, average radial statistics compare against experimental data.

Mean radial pressure statistics are included in Fig. 6.6. The normalized pressure profiles for $r/r_N < 2$ match well with results presented in Snedeker et al. [216]. For larger radii, predictions agree with experimental measurements; however, slight oscillations are observed between $r/r_N = 2$ and $r/r_N = 4$. This is believed to be due to radiated pressure waves during the time averaging procedure. Compared to the study from Section 6.5.1, the flow is not observed to be as oscillatory. Overall, these simulation results are promising and reveal that near-wall pressure behavior is captured for lower pressure ratios.

6.6 Multi-phase PSI

In this section, a numerical simulation of multiphase PSI is performed to demonstrate the capabilities of the described framework. See Fig. 6.7 for an example visualization of the case being considered. A domain of $L_x \times L_y \times L_z = 4.65D_N \times 40D_N \times 40D_N$ is used with an impingement height of $(h_x - h_b)/D_N = 3.65$ and a pressure ratio of NPR = 4.03. The ambient gas is assumed to be air where the ratio of specific heats is $\gamma = 1.4$. The simulation setup and flow conditions are consistent with those described Section 6.5.1. To ensure particle collisions are properly resolved, a constant timestep size of $\Delta t = 0.003$ is used which leads to a CFL condition of CFL ≈ 0.5.

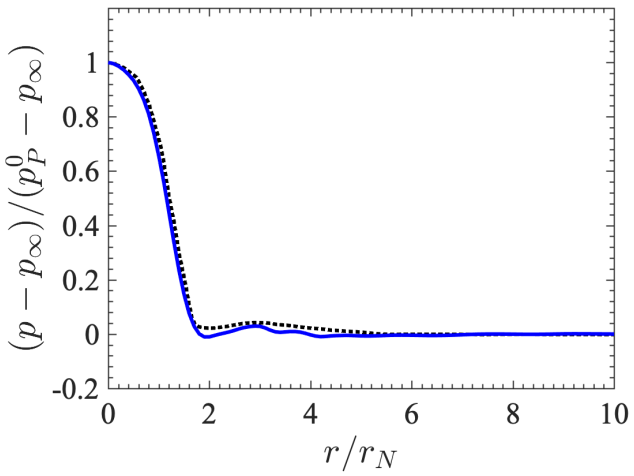

Figure 6.6: Mean noramlized surface pressure plot for $h_x/D_N = 1.96$ and NPR $= 2.69$ for normalized radius, where r_N is the nozzle radius. Numerical data is indicated by (—) while experimental data from Snedeker et al. [216] is indicated by (····).

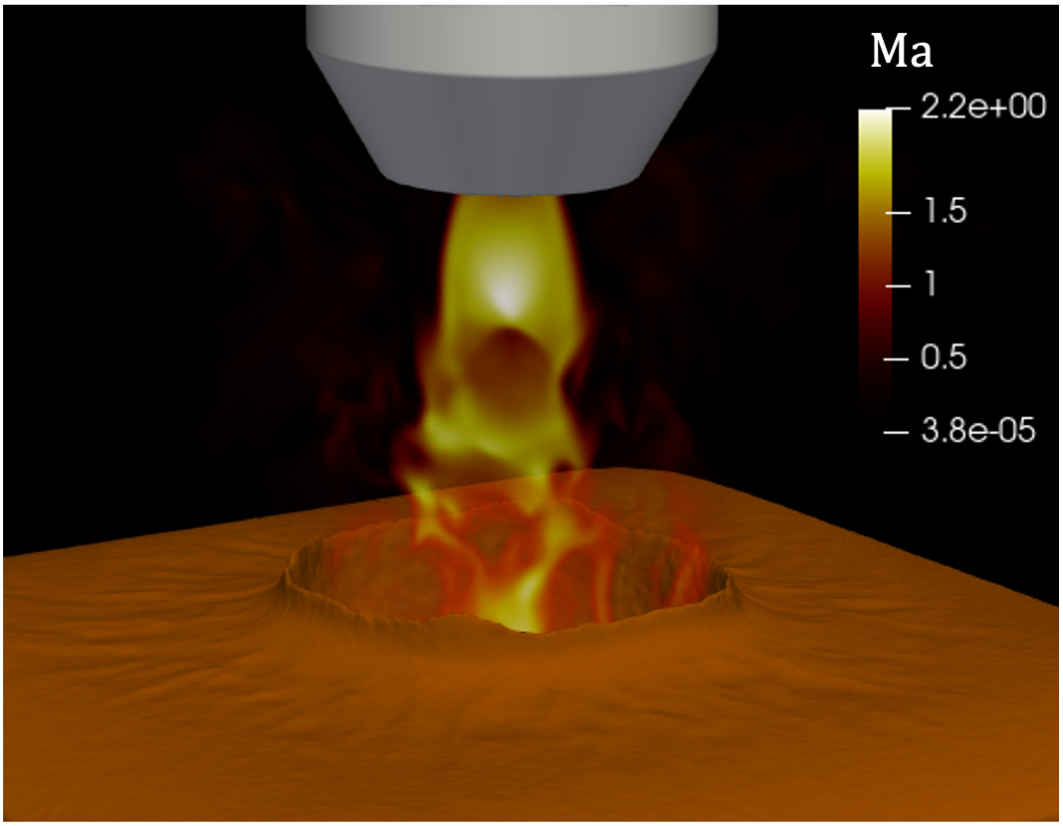

Figure 6.7: Sonic jet impingement on a granular bed with NPR $= 4.03$, $(h_x - h_b)/D_N = 3.65$, and $h_b = 1$ at time, $tD_N/u^* = 55.32$. The flow is colored by local Mach number while an iso-surface of volume fraction is included for $\alpha = 0.6$ to show the presence of the granular bed.

6.6.1 Joint probability density functions of particle volume fraction versus Mach and Reynolds number

Regimes of particle motion can be defined by particle Mach number, particle Reynolds number, and particle volume fraction. The particle Mach and Reynolds number based on the virtual slip velocity are given by, $\mathrm{Ma}_p = \alpha^{(i)}|v_p^{(i)} - \boldsymbol{u}^{(i)}|/c$, and Reynolds number, $\mathrm{Re}_p = \rho^{(i)}\alpha^{(i)}|v_p^{(i)} - \boldsymbol{u}^{(i)}|d_p/\mu$ where $\alpha^{(i)}$, $\rho^{(i)}$, and $\boldsymbol{u}^{(i)}$ are the fluid volume fraction, density, and velocity interpolated to the i-th particle. By using a joint probability density function (jPDF), it is possible to show the regimes that dominate PSI events [16]. Here the procedure described by Balakrishnan and Bellan [16] to calculate jPDF's is extended to individual particle motion. In this study the quantities of interest, including particle Mach number, Reynolds number, and volume fraction are stored at the Lagrangian particle position for a single time instant and are used to in the jPDF algorithm. For plotting purposes the log of the jPDF field is taken, given by $\log(\mathrm{jPDF} + \epsilon_m)$ where ϵ_m is machine epsilon. Data is plotted at a non-dimensional time of $tD_N/u^* = 55.32$. Regions of red show high probability while regions of blue show low probability.

The jPDF of particle Mach number versus particle volume fraction is shown in Fig. 6.8(a). The regions of high probability exist for large particle volume fractions, around $\alpha_p = 0.6$ with $\mathrm{Ma}_p < 0.1$, and $\alpha_p < 0.5$ around $\mathrm{Ma}_p = 0.2$. This shows that particles that are in denser concentrations or closed packing experience lower Mach numbers or remain stationary in the bed. Alternatively there are rare occurrences when particles are in the presence of lower volume fractions at higher Mach numbers, which are likely ejection events. For these instances, particles can be traveling in excess of $\mathrm{Ma}_p = 1$. A similar trend exists for both the jPDF's of particle Reynolds number versus volume fraction, see Figs. 6.8(b). There are a wide range of Reynolds numbers experienced at lower particle volume fractions; however, higher probabilities occur around the closed packing region of $\alpha_p \approx 0.6$, where $\mathrm{Re}_p \leq 1000$. The presented

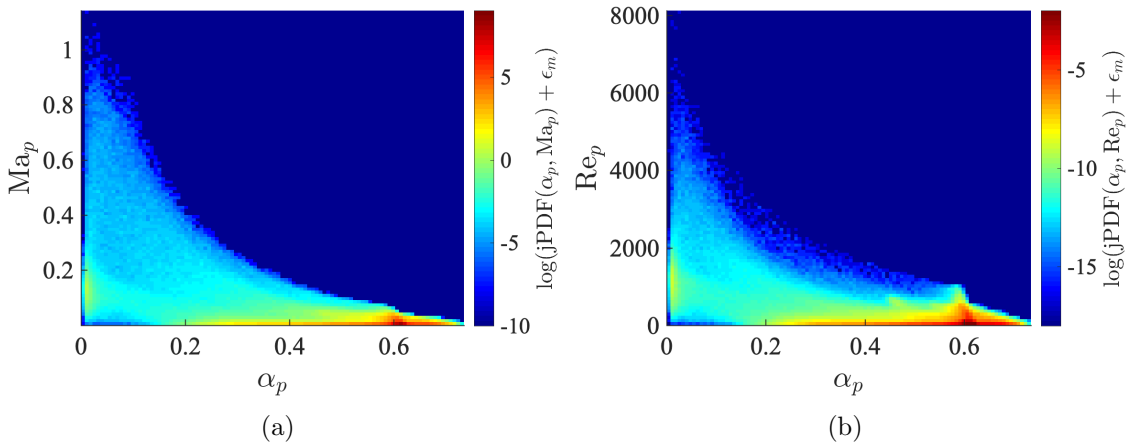

Figure 6.8: (a) Maximum particle Mach number and (b) maximum particle Reynolds number versus non-dimensional time during PSI at time $tD_N/u^* = 55.32$.

results are consistent with those described in Balakrishnan and Bellan [16]; whereby, the majority of particles during crater formation experience subsonic flow regimes.

The jPDF's indicate regions where modeling efforts should be focused. Here, the majority of the bed is at rest while high speed ejecta events occur at low particle volume fractions, see Fig. 6.8. Models are relatively accurate for these cases. The intermediate region, where $0.1 < \phi_p < 0.4$ and $0.2 < \mathrm{Ma}_p < 0.8$ requires further attention. Simulations of canonical flows, like shock-particle interactions from Chapter V, can be used to target modeling efforts for particle motion and sub-filtered fluid quantities under these regimes. It is important to note that these jPDF's were extracted from one simulation at an instant in time. Studies for different NPR and impingement heights are required to characterize the range of operating conditions and their temporal evolution for future modeling efforts.

6.6.2 Granular temperature

Granular temperature, Θ_p, represents the random uncorrelated motion of the particle phase and is an important quantity that describes fluctuation in motion. This has applications to macroscale formulations and can be used in model fluctuations in ve-

locity for particle forcing or as part of a closure for constitutive relations [59, 16]. Here, the granular temperature is extracted for instances of the Eulerian–Lagrangian simulation of PSI for demonstration purposes. Since this quantity is normally discussed and defined in terms of two-fluid formulations, care must be taken when extracting Θ_p from Eulerian-Lagrangian data. First, the particle velocity data is projected to the mesh using the same procedure described in Section 3.2.1,

$$\overline{\alpha \boldsymbol{u}_p} = \sum_{i=1}^{N_p} \mathcal{G}\left(|\boldsymbol{x} - \boldsymbol{x}_p^{(i)}|\right) \mathcal{V}_p^{(i)} \boldsymbol{v}_p^{(i)}, \tag{6.20}$$

Here, $\boldsymbol{u}_p$ is the Eulerian particle velocity, N_p is the number of particles, $\mathcal{G}$ is a filtering kernel, and $\mathcal{V}_p$ is the volume of the i-th particle. The local fluctuation in particle velocity, $\boldsymbol{v}_p^{'(i)}$, can then be defined in terms of the phase average given by,

$$\boldsymbol{v}_p^{'(i)} = \boldsymbol{v}_p^{(i)} - \frac{\overline{\alpha \boldsymbol{u}_p}}{\overline{\alpha}}. \tag{6.21}$$

Using this quantity, the Lagrangian representation of granular temperature is given by,

$$\Theta_p^{(i)} = \frac{1}{3} \boldsymbol{v}_p^{'(i)} \cdot \boldsymbol{v}_p^{'(i)}. \tag{6.22}$$

The same filtering procedure can be applied, providing and Eulerian representation of granular temperature,

$$\alpha \overline{\Theta_p}(\boldsymbol{x}, t) = \sum_{i=1}^{N_p} \mathcal{G}\left(|\boldsymbol{x} - \boldsymbol{x}_p^{(i)}|\right) \mathcal{V}_p^{(i)} \Theta_p^{(i)}. \tag{6.23}$$

Granular temperature is calculated and its evolution is visualized for the plume impinging on a granular surface, see Fig. 6.9 for reference. In this visualization the granular temperature for early and late stage impingement occurs at the surface of the granular bed. Here, particles begin to fluidize and are radially expelled from the crater. During this process, particles in regions of high shear, where $\phi_p < 0.6$,

regularly collide with one another causing fluctuations in velocity. These particle fluctuations lead to induced kinetic energy and thus granular temperature as described above. Meanwhile, particles that are in submerged in the bed are stationary and experience little to no effect from the impinging jet and therefore granular temperature is smaller.

To comment on the contribution of granular temperature, the average speed of particles conditioned by particle volume fraction is plotted for $tD_N/u^* = 55.32$ in Fig. 6.10. The magnitude of granular temperature, compared to the square of particle speed, is significant for particles at smaller volume fractions where the velocity magnitude is $O(10^{-2})$ for the time shown. In comparison, granular temperature is relatively small compared to ejected particles that can reach sonic speeds, as seen in 6.8(a). Overall, additional studies must be performed to look at the relative contribution of this quantity for different flow configurations, pressure ratios, and particle densities. When significant, such data can directly inform two-fluid modeling approaches for PSI studies and other simulations involving highly collisional flows.

In summary, local granular temperature was extracted from the PSI simulations using the same filtering operations employed for two-way coupling. This represents the first glimpse into the local granular temperature during cratering of granular media, and provides useful insight for Eulerian-based two-fluid models that require models for this quantity.

6.6.3 Vertical particle motion in the granular bed

As the jet interacts with the granular bed, particle matter is displaced during crater formation. This can be represented by the vertical motion of the particle phase as the crater grows larger. The described particle motion is shown through a plot of the average vertical particle velocity versus radial position for vertical cross sections of the domain, see Fig. 6.11. This is calculated by binning vertical and radial particle

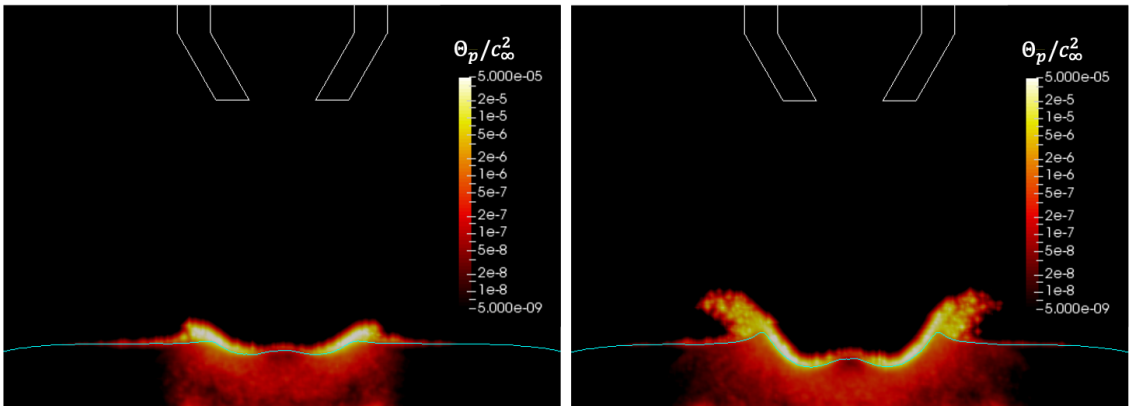

(a) $tD_N/u^* = 22.46$ (b) $tD_N/u^* = 33.41$

(c) $tD_N/u^* = 44.36$ (d) $tD_N/u^* = 55.32$

Figure 6.9: Granular temperature (Θ_p) visualized in log scale for different times. The nozzle outline is shown in white and corresponds to the levelset $\phi = 0$. A volume fraction contour for $\alpha = 0.6$ (teal) is also shown.

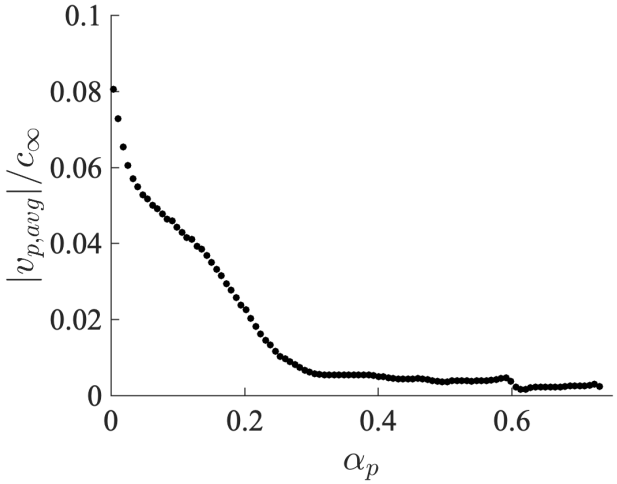

Figure 6.10: Average Lagrangian particle velocity magnitude, conditioned by volume fraction, at $tD_N/u^* = 55.32$.

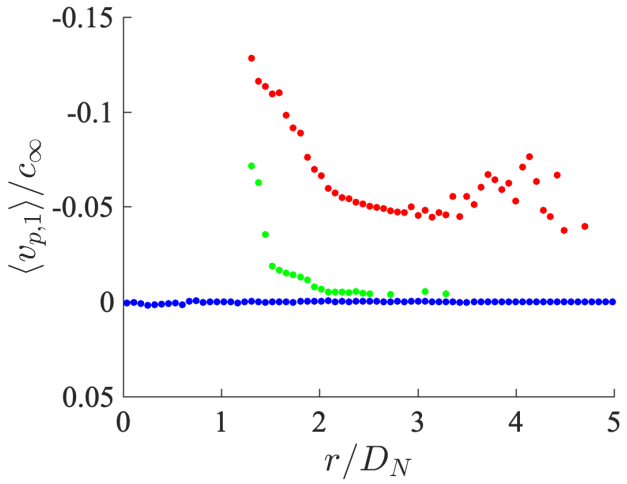

Figure 6.11: Average particle velocity in the x direction versus normalized radius in the particle bed at $tD_N/u^* = 55.32$. The particle velocity is averaged across cross sections in the x-direction for $x/D_N = 3.66$ (●), $x/D_N = 4.90$ (●), and $x/D_N = 6.13$ (●).

positions for sampling purposes. Following, the average vertical particle velocity is calculated for respective bins. Plots are shown for vertical positions of $x/D_N = 3.66$, $x/D_N = 4.90$, and $x/D_N = 6.13$ at an instant in time, $tD_N/u^* = 55.32$. The position $x/D_N = 6.13$ is located at the bottom of the bed where particles are stationary and therefore have not interacted with the impinging jet. As a result, vertical velocity is close to zero for all particles in this region. By decreasing x/D_N the magnitude of the vertical particle velocity increases. This trend shows that particles at the surface of the bed are traveling at higher speeds which can lead to fluidization and potential ejection events as the jet burrows into the granular matter. The described data can be used to characterize the flux of particles during jet impingement. Experimentally, this directly related to the qualitative data for particle mixing and motion during jet impingement in Metzger et al. [155]; however, the present numerical technique provides instantaneous information on particle motion in the crater as opposed to using post-PSI measurements.

6.7 Conclusions

In this work, validation was shown for single-phase jet impingement on flat surfaces for different NPR and impingement heights. Reasonable agreement was observed for averaged velocity profiles and surface pressure measurements. While errors were observed in near-wall velocity estimations, it was deemed reasonable to perform a proof-of-concept simulation of plume impingement on a granular surface. It was demonstrated that the volume-filtered formulation, compressible Eulerian–Lagrangian method, and CBVP immersed boundary method can be used in conjunction to simulate plume impingement on a granular bed with individual particle tracking for the first time. Results of this study show the presence of crater formation and ejecta phenomena during sonic jet impingement on a collection of monodisperse particles. The jPDF's of the Lagrangian particle information revealed that the majority of particles experience subsonic speeds in the granular bed, while ejected particles can exceed sonic speeds at high Reynolds numbers. Granular temperature was quantified for crater formation for the first time. This was found to be most active, and relatively significant, in the vicinity of the crater in regions of high shear where particles are highly collisional. Finally, particle velocity distributions were calculated. It was observed that vertical velocity of the particle phase tends to increase with decreasing x/D_N, indicating the presence of particle fluidization and ejection at the surface of the crater. While intuitive, temporally varying distributions can provide information on particle fluxes which indicate the amount of granular material being ejected during crater formation,.

This work can be extended to higher Mach flows and deeper granular beds where violent granular erosion phenomena have been observed, see Section 1.2. In addition, the effect of NPR on crater morphology remains an open question. Before these future studies, modifications are required for the equations of motion and the implemented numerical scheme.

In summary this is an under-resolved problem. Numerically, it is not feasible to resolve all scales associated with such high Reynolds numbers which leads to very turbulent behavior. This combined with the highly compressible nature of the flow leads to the formation of large discontinuities and oscillations in space. With the described high-order centered finite difference scheme, these oscillations can grow in time leading to the errors observed in Section 6.5.1. To make matters worse, localized shock capturing schemes, like the one used for these studies, are not capable of mitigating this behavior. Fixing this would require a reformulation of the energy equation in combination with other schemes and/or corrections to account for higher order conservation properties for quantities like entropy [98]. Further discussions and corrections have been proposed for such issues [94, 215, 257]. That being said, implementation and testing of additional formulations, numerical schemes, and corrections is considered to be future work.

CHAPTER VII

Conclusions

7.1 Summary of achievements

The significant contribution of this work is the extension of Eulerian–Lagrangian method to compressible flows. Particles are common in a variety of compressible flow applications and it is intractable to resolve small scale flow structures in the presence of dense particle concentrations. This volume filtering procedure provides a framework grounded in first principles that extends to scales significantly larger than the size of an individual particle. By treating particles in a deterministic manner (i.e., each particle represents a physical particle), the compressible volume-filtered Eulerian–Lagrangian framework can be used capture collective particle motion for complex problems like PSI.

This work began with the derivation of the compressible form of the volume-filtered equations of motion from first principles which revealed unclosed term contribution yet to be modeled in literature. To supplement the new formulation, a framework is provided to develop improved models. This includes an improved explicit CBVP method to develop high resolution data for compressible flows past complex geometries as well as an *a posteriori* filtering procedure allowing for the generation of data consistent with the volume-filtered formulation. Using this framework, it was demonstrated that unclosed quantities from the volume filtered formulation, includ-

ing *pseudo*-turbulent kinetic energy and the *pseudo*-turbulent Reynolds stresses, have non-negligible contributions in high-speed particle-laden compressible flows. Following, a new transport equation and model for *pseudo*-turbulent kinetic energy is proposed and demonstrated for shock-particle interactions. To conclude this work, the CBVP immersed boundary method was combined with the compressible Eulerian–Lagrangian method to simulate jet impingement on flat surfaces and a granular bed. Additional details on specific achievements are provided below.

1. In Chapter I, a summary of PSI is presented along with applicable experimental and numerical studies.

    1.1. The physics of PSI is introduced along with conditions relevant for different landing environments.

    1.2. Experimental studies are discussed along with difficulties regarding measurements.

    1.3. Numerical methods for a various simulation methodologies, including microscale, mesoscale, and macroscale approaches, are presented in the context of simulating PSI and regimes applicable to landing conditions.

2. In Chapter II, a thorough derivation of volume-filtered equations of motions is presented for particle-laden compressible flows.

    2.1. The volume-filtered equations reveal a series of unclosed terms that have yet to be modeled in literature.

    2.2. This set of equations provides a framework to develop models for future works.

3. In Chapter III, the derived volume-filtered equations of motion are evaluated in an Eulerian-Lagrangian method for compressible flows.

3.1. A parametric study is shown for two-dimensional shock particle interactions, revealing reasonable agreement when compared to experimental data.

3.2. Expanding this study to three-dimensions reveals that results heavily depend on the implemented drag correlation. In addition, particle collisions are shown to be prominent when predicting the motion of dense particle concentrations in compressible flows.

3.3. The results reveal that improved models are required for accurate predictions of particle motion in compressible flows.

4. In Chapter IV, an explicit form of the CBVP immersed boundary method is proposed for both the Navier–Stokes and Euler equations.

4.1. As opposed to previous forms of CBVP which requires tuning parameters, this form applies limitations to key parameters based on the underlying discretization, such as the sound speed and time step size.

4.2. A series of verification and validation cases are performed for one-, two-, and tree-dimensional subsonic and supersonic flows pasted immersed objects.

4.3. The resulting scheme is simple to implement in that it only requires modifications to the right-hand side of the governing equations, efficient in that it does not restrict the time step size for explicit discretizations, and is accurate as shown through testing under steady and unsteady subsonic and supersonic flows.

5. In Chapter V, highly-resolved data of shock-particle cloud interactions is used to evaluate contributions of unclosed terms in the compressible volume-filtered equations of motion.

5.1. An *a posteriori* filtering approach is presented to quantify terms consistent with the volume-filtered formulation.

5.2. The importance of the unclosed terms were shown to be dependent on the underlying discretization employed, quantified by varying the filter size, δ_f.

5.3. A constant appearing in the dissipation rate was fit over a range of volume fractions and Mach numbers in both two-dimensional and three-dimensional shock-particle configurations.

5.4. The Eulerian–Lagrangian approach was shown to be capable of predicting the distribution of pseudo-turbulent Reynolds stresses with the correct level of anisotropy.

6. In Chapter VI, initial work for single- and multi-phase PSI simulations is shown.

6.1. Validation is performed for two different single-phase jet impingement configurations. This includes (1) An NPR = 4.03 jet with impingement heights of $h_x/D_N = 2.08$, $h_x/D_N = 3.65$, and $h_x/D_N = 4.16$ to centerline velocity and cross sectional velocity magnitudes and (2) a NPR = 2.69 jet with an impingement height of $h_x/D_N = 1.96$ to measure mean surface pressure profiles.

6.2. A proof of concept case for a NPR = 4.03 jet impinging on a granular bed of discrete particles is shown for the first time.

6.3. Data is extracted from jet impingement including jPDF's of particle Mach and Reynolds number versus particle volume fraction, revealing that the majority of the particle bed experiences subsonic flow conditions at low Reynolds numbers while ejected particles can exceed sonic Mach numbers.

6.4. Additional quantities, including granular temperature and vertical particle

motion, are extracted from the simulation of jet impingement on a granular bed which have direct applications to modeling for future PSI studies.

7.2 Prospectives on Future work

7.2.1 Modeling particle forces in compressible flows

In this work, significant attention was spent on formulating equations of motion in Chapter II and modeling sub-filtered quantities in Chapter V. That being said, particle force modeling was largely neglected due to the already vast scope of the presented work. For accurate predictions of multi-particle motion, improved particle force models are required for improved simulations of plume surface interactions (PSI) described in Chapter VI.

While models for particle force, such as those presented in the BBO equation [18, 30, 170] have been used for decades, their form can introduce errors. For example, drag laws are commonly developed using the concept of an undisturbed velocity field. This is a remnant from the derivation of Stokes drag whereby the slip velocity is defined in terms of the oncoming "undisturbed" velocity and the velocity of the spherical particle. From a Lagrangian standpoint, the undisturbed velocity is not normally known for two-way coupled simulations. This is a limitation of most drag laws. It is common to interpolate the fluid velocity at the particle positions and acknowledge the error associated with using disturbed fluid velocity. Methods do exist to reconstruct the undisturbed fluid velocity from a point-particle perspective [63, 64, 71, 82, 83, 93, 12]. While useful, these methods can be limited to certain flow regimes whereby extensions to compressible flows (e.g. standing bow shocks upstream of particles) do not yet exist.

When considering force contributions on collections of particles, modeling becomes more challenging. For these cases, particles not only feel the influence of the oncoming

flow but also experience fluctuations in the flow due to interactions with wakes of other particles. For subsonic flows, PR-DNS has been performed for triply periodic systems of particles [79, 21, 233] leading to improved mean drag estimations on collections of spheres that are volume fraction dependent. These works are limited to subsonic flows at low to moderate Reynolds numbers. From a compressible-flow perspective modeling homogenous, triply periodic systems of particles is not necessarily straight forward. Alternatively, there has been increasing interest in simulating fully resolve shock particle interactions [236, 238, 151, 153, 152, 172, 173] that in some cases have been used to look at mean and fluctuation forces on particles. That being said, these studies have not resulted in improved force models for collections of particles.

Overall, improvements need to be made when modeling forces for multi-particle systems in compressible flows. Many existing models are not consistent with the formulation used during simulations (i.e. using the disturbed versus undisturbed velocity for force estimations on particles). Considering the formulation presented in Chapter II, improved models can be created by applying the *a posteriori* filtering procedure on highly resolved compressible flows past collections of particles, presented in Chapter V. This not only provides local particle volume fraction information but also the filtered local velocity, pressure, and viscous stress information. Using this information, models can be created based on local filtered information as opposed to mean quantities across the domain allowing for extraction of not only mean but variance of forces on collections of particles. While this would be expensive and would require multiple realizations, to account for random particle arrangements, it would lead to robust particle force models.

7.2.1.1 Stochastic extensions to particle motion

As mentioned in Chapter I, systems of particles experience a variance of force as they interact with surrounding particles. These effects are largely neglected when

modeling particle forces; however, are vital to capture the motion of collections of particles.

There are a couple of prominent approaches that can be taken to account for the variance of drag in a particle-laden flow. One such approach is the pairwise interaction extended point-particle (PIEP) method proposed and expanded by Akiki et al. [2, 3], Moore et al. [165]. For this approach, the forces due to neighboring particles in Eulerian-Lagrangian methods are accounted for by the superimposition of the influence from surrounding particles. As a result, particles not only feel an influence from some standard mean drag, typically derived from averaged DNS data, but also some variance due to disturbances caused by surrounding particles. Extensions of this method are also being proposed for compressible flows [86]. While promising, this method can be rather expensive due to the computational cost associated with nearest neighbor search algorithms. In addition the described implementations appear to be limited to stationary particles [2, 3, 165].

Another option is to use stochastic methods, which are the most promising approach from a personal perspective. Here, a stochastic differential equation can be used to govern particle motion by introducing an appropriate random component, typically through position or velocity, to account for some unresolved contribution. From small particle motion, this was originally used to account for Brownian motion [243], typically referred to as a Langevin equation. Extensions have also been proposed for applications in single phase compressible turbulence [190, 51]. Recently, these methods have also been used to modify particle motion of incompressible two-phase flows [158, 159, 191, 160]. Some of these models are limited to certain flow configurations (e.g. homogeneous isotropic turbulence) and heavily rely on scaling laws from Kolmogorov's hypotheses [109]. That being said, improvements have been made to these methods, such as account for higher order forcing contributions, that show extreme promise for future estimations in unresolved drag contributions while

using Eulerian-Lagrangian modeling approaches [235, 118].

These stochastic models, and their potential expansions to compressible flows, are likely the future of modeling particle-laden flows. They do not require searching for surrounding particle locations or make assumptions about the superposition of flow structures. With that being said, modeling will be challenging considering the fluctuations in flow generated by multi-particle systems and the uncertainties in drag when considering variations in Mach number, as observed for single particle force estimations Nagata et al. [167, 168].

7.2.2 Modeling unresolved contributions in particle-laden compressible flows

By performing the volume filtering procedure on the compressible Navier–Stokes equations, many unclosed contributions arise in conservation of momentum, conservation of energy, and the equation of state. See Chapter II for the full forms of these equations. While these contributions are normally neglected for particle-laden compressible flow simulations, it was shown in Chapter V and by Mehta et al. [152], Osnes et al. [171], using filtering and averaging procedures respectively, that PTKE and *pseudo*-turbulent Reynolds stresses possess some finite contribution for under-resolved simulations. To make matters worse, there are very few models in literature to capture these contributions, and those that exist are typically algebraic in nature and limited to certain flow regimes [146, 171, 214].

The formulation in Chapter II and framework presented in Chapter V provides a means to quantify contributions and generate models for future simulations. While a model for PTKE and the *pseudo*-turbulent Reynolds stresses is proposed in Section 5.3.1, it is based off of an empirical algebraic closure for dissipation. For broader application, a dissipation transport equation, similar to PTKE transport equation, must be derived. Dissipation transport equations exist for single-phase tur-

bulence [189]; however, additional source and work terms may arise in the presence of particles and interphase coupling.

While it was shown that the PTKE and *pseudo*-turbulent Reynolds stress terms were dominant for shock-particle interactions, this does not justify that other unclosed terms should be neglected. Other canonical flows should be studied to determine the relative contributions of the remaining terms. This could include studies involving heat transfer or reactions, where temperature gradients could increase the relative contribution of the *pseudo*-turbulent heat flux. Creating improved models would be expensive; however, it is necessary to capture physics while simulating larger scale particle-laden compressible flows like PSI.

7.2.3 Multiphase PSI studies

To reiterate, PSI events can lead to damage during landing maneuvers due to the fluidization and ejection of granular matter. As highlighted in Chapter I, this phenomenon will continue to be a challenge for future exploratory missions to planetary and satellite bodies. This has led to a multitude of experimental and numerical studies to analyze the effects of PSI under various landing conditions. One common theme in these studies is the emphasis on the unknown physics of PSI. This includes but is not limited to uncertainties in particle forcing and trajectories under landing conditions [156] and behavior of fluidization and its relation to jet configurations and exhaust [148].

While additional experiments and simulations are required to characterize PSI, care must be taken when planning future work. This was a major point highlighted by Metzger et al. [156] when performing PSI experiments for lunar landing. From an experimental perspective, studies under modified environmental and gravitation conditions, like those performed in Kuhns et al. [113], will provide insight into general crater formation without relying on observational methods during landing events.

These accurate studies can be bolstered by investing into high-resolution imaging and non-intrusive measurement techniques to improve characterization of crater formation. That being said, there are limitations to the data that can be collected for these studies. Simplified flow configurations, such as those highlighted in Section 1.6, can help characterize the fundamental physics of PSI, such as particle forcing and flow dynamics of jet impingement during landing. These experimental studies can be used in conjunction numerical methods to validate and create improved models that capture the physics of PSI.

From a numerical perspective, improved models and methods are required before extensively performing simulations of PSI and other applicable flow configurations. Models for particle motion in compressible flows, as discussed in Sections 7.2.1 and 7.2.1.1, and unresolved flow contributions, highlighted in Chapter II, are short of what is needed to guarantee accurate simulations of these phenomena. Using models that were not designed for the flows of interest can be potentially hazardous for any engineering application. One of the major purpose of this work was to create a framework under which improved models for particle-laden compressible flows can be created. In practice, highly resolved data from microscale and mesoscale simulations can inform models for macroscale approaches in a manner that is consistent with the governing equations of motion. As a result, it will be possible to create accurate simulations of large scale PSI, albeit with significant investments in time and effort.

Throughout this work and other applicable studies, it is typically assumed that simulations involve inert flows. Given that rocket propulsion involves a series of chemical reactions and exhausted products, this is a very strong assumption that has implications for future missions. In recent years, plans have been proposed for Mars Sample Return, whereby "*Martian rocks, soils, and atmosphere*" will be collected and sent back to Earth for analysis [97]. During landing, there are concerns that jet exhaust is capable of altering biological matter on a planetary surface or introduce new

contaminants to collected samples [88, 39]. Numerically, this can include additional transport equations for species of jet exhaust and other physics, like charged particle deposition [255], onto impinging surfaces. Experimentally, this can involve highly sensitive measurements of biological matter and contaminants in arbitrary samples, unlike those collected during missions [88, 39]. Overall, this is a significantly difficult topic and requires attention for success in future planetary exploration.

APPENDICES

APPENDIX A

Additional Information on CBVP Method

A.1 Details on evaluating surface quantities

Special care needs to be taken when evaluating fluid stresses acting on the surface of an immersed object. The force can be calculated by integrating the divergence of the stress throughout the volume of the object, i.e.,

$$\boldsymbol{F} = -\int_{\Omega_{ib}} \nabla \cdot (p\mathbb{I} - \boldsymbol{\tau}) \, \mathrm{d}V \approx \sum_{k \in \Omega_{ib}} \nabla \cdot (p\mathbb{I} - \boldsymbol{\tau})_k \, \Delta V_k, \tag{A.1}$$

where $\mathrm{d}V$ is an infinitesimal volume element within the region occupied by the immersed object, Ω_{ib}, which is approximated as a summation over grid points $k \in \Omega_{ib}$ with volume ΔV_k. While this provides an accurate estimate of the force without adding excessive computational cost [84], it does not provide access to the distribution of stress along the surface, which is needed when evaluating the pressure coefficient $C_p(\theta)$ in Sec. 4.9. Using the divergence theorem, the force can be evaluated by

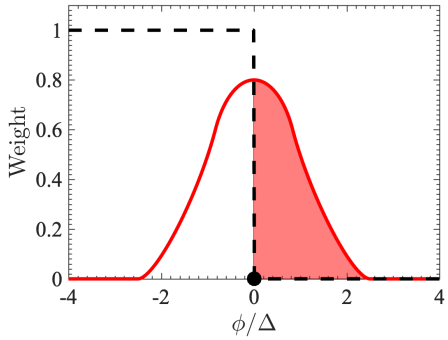

Figure A.1: Illustration of the interpolation procedure used in this work. Masking function used in the volume penalization $\mathcal{X}$ (- - -) and modified Roma kernel (—). The red shading indicates the area of integration at a marker located at the surface of the immersed boundary (●).

integrating the stress along its surface, given by

$$\boldsymbol{F} = -\int_{\Gamma_{ib}} (p\mathbb{I} - \boldsymbol{\tau}) \cdot \boldsymbol{n} \, \mathrm{d}S \approx \sum_{k=1}^{N_m} (\hat{p}_k \mathbb{I} - \hat{\boldsymbol{\tau}}_k) \cdot \boldsymbol{n}_k \, \Delta S_k, \tag{A.2}$$

where $\boldsymbol{n}$ is the outward unit normal vector and $\mathrm{d}S$ is an infinitesimal surface element along the surface of the immersed boundary, Γ_{ib}. This can be approximated discretely by summing over the fluid stress interpolated to a set of N_m Lagrangian markers. Here, $\hat{p}_k$ and $\hat{\boldsymbol{\tau}}_k$ are the pressure and viscous stress interpolated to the k-th marker, respectively, ΔS_k is the surface area element associated with the marker and $\boldsymbol{n}_k$ is its outward normal vector. In two dimensions, markers are evenly distributed over the surface of the object analytically, therefore the surface element is defined as $\Delta S_k = S/N_m$, where S is the perimeter associated with the object. In three dimensions, markers are distributed over the surface of the object by placing them at the centroid of triangular planes obtained by a stereolithography (STL) representation. In this case, the surface element is defined as the area of the corresponding triangle.

Interpolation techniques typically employed in immersed boundary methods, such as the inverse distance function [41], may introduce perceived boundary oscillations on

coarse grids. Alternatively, regularized Dirac delta functions are commonly employed (e.g., [198, 244]). Interpolation of a quantity $a(\boldsymbol{x})$, which may be a scalar-, vector-, or tensor-value within the computational domain, Ω, to a marker located at $\boldsymbol{y} \in \Gamma_{ib}$, is performed via convolution with a compact, regularized Dirac delta function $\delta_L(\boldsymbol{x}, \boldsymbol{y}, \Delta\boldsymbol{x})$, according to

$$\hat{a}(\boldsymbol{y}) = \sum_{\boldsymbol{x}\in\Omega} a(\boldsymbol{x})\delta_L(\boldsymbol{x}, \boldsymbol{y}, \Delta\boldsymbol{x}). \tag{A.3}$$

The delta function proposed by Roma et al. [198] has been widely adopted for immersed boundary methods, given by

$$\psi(r) = \begin{cases} \frac{1}{3}\left(1 + \sqrt{-3|r|^2 + 1}\right), & |r| < 0.5 \\ \frac{1}{6}\left(5 - 3|r| - \sqrt{-3(1-|r|)^2 + 1}\right), & 0.5 \leq |r| \leq 1.5 \\ 0, & |r| > 1.5 \end{cases}, \tag{A.4}$$

where r is the normalized Euclidean distance from a grid point to a marker. Here, we make several modifications to the original interpolation scheme proposed by Roma et al. [198]. First, the radius of extent of the scalar function ψ is increased. This is done by applying a scaling factor, β, to the Euclidian distance. Second, only quantities exterior to the object are used during interpolation. This is done by applying a masking function, α, to the scalar function ψ. For our purposes, $\alpha = 1$ on the exterior of the object ($\phi > 0$), and $\alpha = 0$ on the interior of the object ($\phi \leq 0$). Finally, to ensure the kernel integrates to unity, a normalization step is performed. For an N_d-dimensional problem, the regularized delta function is given by

$$\delta_L(\boldsymbol{x}, \boldsymbol{y}, \Delta\boldsymbol{x}) = \frac{\alpha \prod_{i=1}^{N_d} \psi\left(\beta|x_i - y_i|/\Delta x_i\right) \Delta x_i^{-1}}{\sum_{\boldsymbol{x}\in\Omega} \alpha \prod_{i=1}^{N_d} \psi\left(\beta|x_i - y_i|/\Delta x_i\right) \Delta x_i^{-1}}. \tag{A.5}$$

In the present formulation, we employ a scalar factor of $\beta = 0.6$, which yields a

maximum radius of extent of $R_m = 2.5\Delta x$. Figure A.1 shows a one-dimensional illustration of these modifications. It should be noted that choosing $\alpha = \beta = 1$ resorts back to the original definition of the delta function by Roma et al. [198], which has a radius of extent $R_m = 1.5\Delta x$.

To demonstrate the error associated with sampling quantities at the surface of immersed boundaries, the steady supersonic flow past a cylinder introduced in Sec. 4.9.2.2 is further evaluated here. The drag coefficient is evaluated using a sharp interface ($\epsilon = 0$) with $\Delta x = D/80$ and compared to numerical body fitted data of Takahashi et al. [228]. Table A.1 shows the corresponding total drag and contributions from pressure and frictional stresses computed using surface integration given by Eq. (A.2) with the original interpolation scheme of Roma et al. [198] and the modified interpolation scheme, and using volume integration given by Eq. (A.1). Because the traditional interpolation scheme uses quantities located on the interior and exterior of the object, the velocity gradient is systematically under-predicted, resulting in low values of frictional drag. Pressure drag is less affected due to the Neumann condition imposed on pressure. Drag evaluated using surface integration with the modified interpolation scheme yields similar results as volume integration and the data by Takahashi et al. [228]. For consistency, surface integration with the modified interpolation scheme is used when evaluating drag and pressure coefficients throughout this work.

	Surface integration (A.2) Roma et al. [198]	Surface integration (A.2) Modified scheme	Volume integration (A.1)	Takahashi et al. [228]
C_D	1.479	1.524	1.521	1.548
$C_{D,p}$	1.394	1.394	1.401	1.404
$C_{D,f}$	0.085	0.130	0.120	0.144

Table A.1: Results for drag coefficient (C_D), pressure drag coefficient ($C_{D,p}$), and frictional drag coefficient ($C_{D,f}$) for supersonic flow past a cylinder with $\Delta x = D/80$ and $\epsilon = 0$ using surface integration Eq. (A.2) with the delta function proposed by Roma et al. [198] and the modified interpolation scheme, and volume integration Eq. (A.1). Results are compared to numerical body-fitted data [228].

APPENDIX B

Additional Information on Volume-filter Formulation Analysis

B.1 Methodology for *a posteriori* filtering

The method presented here is used for *a posteriori* filtering of DNS data in Sec. 5.2. An arbitrary quantity A computed using DNS on a mesh with resolution $\Delta x \ll d_p$ is separated into spatially filtered and residual contributions $A = \overline{A} + A'$ according to

$$\alpha\overline{A} = (\mathcal{I}A) \star \mathcal{G}, \tag{B.1}$$

where $\mathcal{I}$ is an indicator function that is 0 inside a particle and 1 in the fluid and $\mathcal{G}$ is a filter kernel. A direct solution to (B.1) is computationally expensive, and in general not tractable when working on large-scale DNS data. Consequently, the convolution integral is recast in Fourier space as

$$\widehat{\alpha\overline{A}} = \widehat{\mathcal{I}wA} \cdot \widehat{\mathcal{G}}, \tag{B.2}$$

where $\widehat{(\cdot)}$ indicates a quantity subject to a Fourier transform. Because the simulations performed in this study are not periodic in the x-direction, a windowing function, w, is applied to the quantity of interest prior to filtering. In this work, a Tukey window [242] is employed, defined as

$$w(i) = \begin{cases} \frac{1}{2}\left[1 + \cos\left(\frac{2\pi i}{r(N_x-1)} - \pi\right)\right] & 0 \leq i < \frac{r(N_x-1)}{2} \\ 1 & \frac{r(N_x-1)}{2} \leq i < (N_x-1)\left(1-\frac{r}{2}\right) \\ \frac{1}{2}\left[1 + \cos\left(\frac{2\pi i}{r(N_x-1)} - \frac{2\pi}{r} + \pi\right)\right] & (N_x-1)\left(1-\frac{r}{2}\right) < i \leq (N_x-1) \end{cases}, \quad \text{(B.3)}$$

where $r = 0.05$ is the cosine tapering parameter, i is the grid point it is being applied to, and N_x is the total number of grid points in the x-direction. The cosine tapering parameter is selected such that that the windowing function does not interfere with the flow field, such as the transmitted and reflected shocks as well as the wake downstream of the particles.

B.2 Term reconstruction through approximate deconvolution

In this appendix we assess the accuracy of reconstructing the sub-filtered terms via a deconvolution procedure. While direct deconvolution is not possible due to the sparse nature of the filtering kernel, a common alternative is to use the approximate deconvolution method (ADM) [219, 251, 176, 204, 205]. This can be accomplished by convolving the approximate inverse of the filtering kernel

$$\hat{\mathcal{G}}^{-1} \approx \sum_{\nu=0}^{N} (1 - \hat{\mathcal{G}})^{\nu} \quad \text{(B.4)}$$

with filtered quantities in Fourier space and then performing an inverse Fourier transform to get an approximation of the flow fields prior to filtering. Here, N is the desired

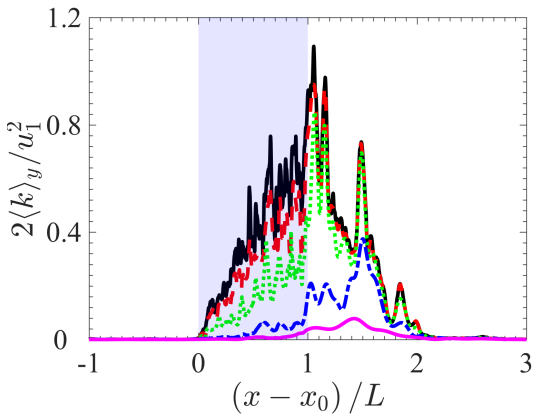

Figure B.1: Ensemble averaged PTKE obtained from DNS (—) and recovered from deconvolution with $\delta_f = d_p$ (- - -), $\delta_f = 2d_p$ (·····), $\delta_f = 4d_p$ (-·-), and $\delta_f = 8d_p$ (—). Quantities are calculated for $\varphi_p = 0.21$ when $t = 2.334$. The shaded region ( ) indicates particle location.

truncation of the series expansion, set to $N = 100$ for this work, and $(\hat{\cdot})$ denotes that the quantity is in Fourier space.

Reconstruction of ensemble averaged PTKE through deconvolution is shown in Fig. B.1. For a filter size of $\delta_f = d_p$, the deconvolution provides a good approximation of PTKE compared to ensemble averaging the DNS data. As the filter size increases, the PTKE calculated from deconvolution continues to decrease. As shown in Fig. 5.4, the unresolved PTKE should either increase or asymptote to some maximum unresolved quantity. While using ADM to approximate the unresolved quantities, it becomes more difficult to recover fluctuations for larger filter sizes and therefore unresolved stresses will be under predicted around the particle phase. While this method is limited to recovering stresses for smaller filter widths, it still has its utility. Other possible uses include the approximation of the unfiltered velocity to improve drag estimations and partial recovery of microscale flow fields during post-processing.

B.3 Drag dependence on PTKE

The PTKE model proposed in Sec. 5.3.1 is expressed for an arbitrary drag law. In this section, we extend the three-dimensional shock-particle analysis presented in Sec. 5.3.5 to evaluate the effect of drag laws on PTKE. Three additional drag laws are considered, each of which are valid under different flow conditions. We consider the Schiller-Naumann drag correlation [44] that depends on Reynolds number, the correlations proposed by Loth [133] and Henderson [78] that take into account Mach number effects, in addition to the drag correlation of Gidaspow [69] used throughout the present study that accounts for volume fraction effects and high Reynolds numbers.

As shown in Fig. B.2, the parameter C_f appearing in the dissipation rate are smaller for Schiller-Naumann, Loth, and Henderson compared to Gidaspow. This indicates that the relative drag production is lower under the same conditions. In this case, the lower drag will result in noticeably faster transmitted shocks and slower reflected shocks compared to the DNS. Regardless of the different behaviors in drag, the distributions of pseudo-turbulent Reynolds stresses are remarkably similar. The results suggest that similar trends in PTKE can be achieved for any of the drag laws used here, provided a reasonable value of C_f.

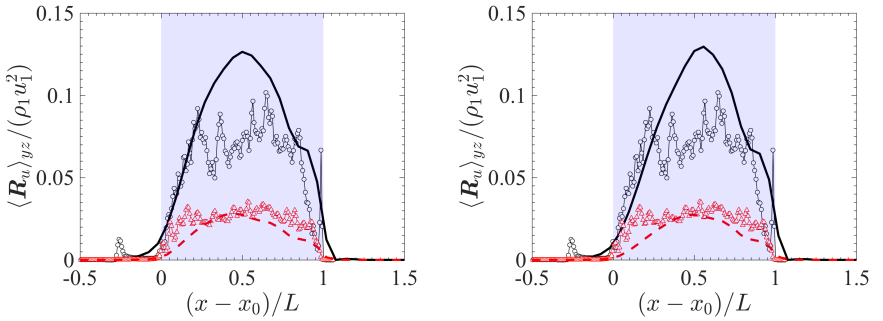

(a) Gidaspow [69], $C_f = 7$

(b) Schiller-Naumann [44], $C_f = 3$

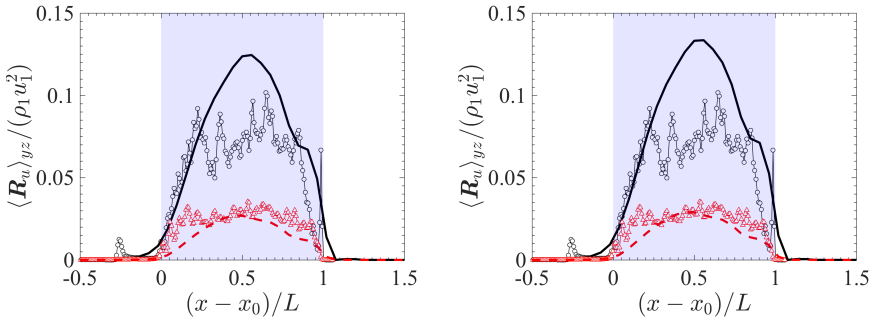

(c) Loth [133], $C_f = 5$

(d) Henderson [78], $C_f = 5$

Figure B.2: Effect of drag law on the components of the pseudo-turbulent Reynolds stress for $\varphi_p = 0.1$ and $\mathrm{Ma}_s = 1.66$ at $t = 0.62$. Same line types as in Fig. 5.14.

BIBLIOGRAPHY

BIBLIOGRAPHY

[1] G. Akiki, T. Jackson, and S. Balachandar. Force variation within arrays of monodisperse spherical particles. *Physical Review Fluids*, 1(4):044202, 2016.

[2] G. Akiki, T. Jackson, and S. Balachandar. Pairwise interaction extended point-particle model for a random array of monodisperse spheres. *Journal of Fluid Mechanics*, 813:882–928, 2017.

[3] G. Akiki, W. Moore, and S. Balachandar. Pairwise-interaction extended point-particle model for particle-laden flows. *Journal of Computational Physics*, 351: 329–357, 2017.

[4] J. Alexander, W. Roberds, and R. Scott. Soil erosion by landing rockets final report. 1966.

[5] J. Amos. Mars rover: Wind sensor damaged on NASA's Curiosity. *BBC News*, 2012. URL `https://www.bbc.com/news/science-environment-19338870`.

[6] T. B. Anderson and R. Jackson. Fluid mechanical description of fluidized beds. Equations of motion. *Industrial & Engineering Chemistry Research*, 6(4):527–539, 1967.

[7] P. Angot, C.-H. Bruneau, and P. Fabrie. A penalization method to take into account obstacles in incompressible viscous flows. *Numerische Mathematik*, 81 (4):497–520, 1999.

[8] E. Arquis and J. P. Caltagirone. Sur les conditions hydrodynamiques au voisinage dune interface milieu fluide-milieu poreux: applicationa la convection naturelle. *CR Acad. Sci. Paris II*, 299:1–4, 1984.

[9] Y. Bae and Y. J. Moon. On the use of Brinkman penalization method for computation of acoustic scattering from complex boundaries. *Computers & Fluids*, 55:48–56, 2012.

[10] A. Bailey and J. Hiatt. Sphere drag coefficients for a broad range of Mach and Reynolds numbers. *AIAA Journal*, 10(11):1436–1440, 1972.

[11] S. Balachandar and J. Eaton. Turbulent dispersed multiphase flow. *Annual Review of Fluid Mechanics*, 42:111–133, 2010.

[12] S. Balachandar, K. Liu, and M. Lakhote. Self-induced velocity correction for improved drag estimation in Euler–Lagrange point-particle simulations. *Journal of Computational Physics*, 376:160–185, 2019.

[13] K. Balakrishnan and J. Bellan. High-fidelity modeling and numerical simulation of cratering induced by the interaction of a supersonic jet with a granular bed of solid particles. *International Journal of Multiphase Flow*, 99:1–29, 2018.

[14] K. Balakrishnan and J. Bellan. A multi-species modeling framework for describing supersonic jet-induced cratering in a granular bed: Cratering on Titan case study. *International Journal of Multiphase Flow*, 118:205–241, 2019.

[15] K. Balakrishnan and J. Bellan. Fluid density effects in supersonic jet-induced cratering in a granular bed on a planetary body having an atmosphere in the continuum regime. *Journal of Fluid Mechanics*, 915, 2021.

[16] K. Balakrishnan and J. Bellan. Ejecta formed during supersonic jet-induced cratering in a granular medium as a function of the atmospheric density in the continuum regime. *AIAA Journal*, in press.

[17] K. Balakrishnan and J. R. Bellan. Cratering in a granular bed due to an impinging supersonic jet penetrating a planetary atmosphere in the continuum regime. In *AIAA Scitech 2021 Forum*, page 0752, 2021.

[18] A. B. Basset. *A treatise on hydrodynamics: with numerous examples*, volume 2. Deighton, Bell and Company, 1888.

[19] F. Bassi and S. Rebay. High-order accurate discontinuous finite element solution of the 2D Euler equations. *Journal of Computational Physics*, 138(2):251–285, 1997.

[20] S. Beetham and J. Capecelatro. Biomass pyrolysis in fully-developed turbulent riser flow. *Renewable Energy*, 140:751–760, 2019.

[21] R. Beetstra, M. A. van der Hoef, and J. Kuipers. Drag force of intermediate Reynolds number flow past mono-and bidisperse arrays of spheres. *AIChE journal*, 53(2):489–501, 2007.

[22] A. Belov, L. Martinelli, and A. Jameson. A new implicit algorithm with multigrid for unsteady incompressible flow calculations. In *33rd Aerospace Sciences Meeting and Exhibit*, page 49, 1995.

[23] H. Benaroya. *Lunar Settlements*. CRC Press, 2010.

[24] K. J. Berger, A. Anand, P. T. Metzger, and C. M. Hrenya. Role of collisions in erosion of regolith during a lunar landing. *Physical Review E*, 87(2):022205, 2013.

[25] P. A. Berthelsen and O. M. Faltinsen. A local directional ghost cell approach for incompressible viscous flow problems with irregular boundaries. *Journal of Computational Physics*, 227(9):4354–4397, 2008.

[26] A. Bhagatwala and S. K. Lele. A modified artificial viscosity approach for compressible turbulence simulations. *Journal of Computational Physics*, 228 (14):4965–4969, 2009.

[27] D. J. Bodony. Accuracy of the simultaneous-approximation-term boundary condition for time-dependent problems. *Journal of Scientific Computing*, 43 (1):118–133, 2010.

[28] R. Borker, D. Huang, S. Grimberg, C. Farhat, P. Avery, and J. Rabinovitch. Mesh adaptation framework for embedded boundary methods for computational fluid dynamics and fluid-structure interaction. *International Journal for Numerical Methods in Fluids*, 90(8):389–424, 2019.

[29] R. Boukharfane, F. H. E. Ribeiro, Z. Bouali, and A. Mura. A combined ghost-point-forcing/direct-forcing immersed boundary method (IBM) for compressible flow simulations. *Computers & Fluids*, 162:91–112, 2018.

[30] J. Boussinesq. Sur la resistance qu'oppose un fluide indefini en repos, sans pesanteur, au mouvement varie d'une sphere solide qu'il mouille sur toute sa surface, quand les vitesses restent bien continues et assez faibles pour que leurs carres et produits soient negligiables. *CR Acad. Sc. Paris*, 100:935–937, 1885.

[31] E. Brown-Dymkoski, N. Kasimov, and O. V. Vasilyev. A characteristic based volume penalization method for general evolution problems applied to compressible viscous flows. *Journal of Computational Physics*, 262:344–357, 2014.

[32] E. Brown-Dymkoski, N. Kasimov, and O. V. Vasilyev. A characteristic-based volume penalization method for arbitrary Mach flows around solid obstacles. In *Direct and Large-Eddy Simulation IX*, pages 109–115. Springer, 2015.

[33] D. A. Buchta, G. S. Shallcross, and J. Capecelatro. Sound and turbulence modulation by particles in high-speed shear flow. *Journal of Fluid Mechanics*, In press:578–635, 2019.

[34] J. Capecelatro and O. Desjardins. An Euler–Lagrange strategy for simulating particle-laden flows. *Journal of Computational Physics*, 238:1–31, 2013.

[35] J. Capecelatro and O. Desjardins. Eulerian-Lagrangian modeling of turbulent liquid-solid slurries in horizontal pipes. *International Journal of Multiphase Flow*, 55:64–79, 2013.

[36] J. Capecelatro, O. Desjardins, and R. O. Fox. On fluid-particle dynamics in fully developed cluster-induced turbulence. *Journal of Fluid Mechanics*, 780: 578–635, 2015.

[37] J. Carling and B. Hunt. The near wall jet of a normally impinging, uniform, axisymmetric, supersonic jet. *Journal of Fluid Mechanics*, 66(1):159–176, 1974.

[38] M. Carpenter, D. Gottlieb, and S. Abarbenel. Time-stable boundary conditions for finite difference schemes involving hyperbolic systems: methodology and application for high-order compact schemes. *Journal of Computational Physics*, 111:220–236, 1994.

[39] Q. H. S. Chan, R. Stroud, Z. Martins, and H. Yabuta. Concerns of organic contamination for sample return space missions. *Space Science Reviews*, 216: 1–40, 2020.

[40] Y.-C. Chang, T. Hou, B. Merriman, and S. Osher. A level set formulation of Eulerian interface capturing methods for incompressible fluid flows. *Journal of Computational Physics*, 124(2):449–464, 1996.

[41] A. Chaudhuri, A. Hadjadj, and A. Chinnayya. On the use of immersed boundary methods for shock/obstacle interactions. *Journal of Computational Physics*, 230 (5):1731–1748, 2011.

[42] J. A. Christian, G. Wells, J. M. Lafleur, A. Verges, and R. D. Braun. Extension of traditional entry, descent, and landing technologies for human Mars exploration. *Journal of Spacecraft and Rockets*, 45(1):130–141, 2008.

[43] S. Chu and A. Prosperetti. On flux terms in volume averaging. *International Journal of Multiphase Flow*, 80:176–180, 2016.

[44] R. Clift, J. Grace, and M. Weber. *Bubbles, Drops, and Particles*. Academic Press Incorporated, 1978.

[45] A. W. Cook and W. H. Cabot. Hyperviscosity for shock-turbulence interactions. *Journal of Computational Physics*, 203(2):379–385, 2005.

[46] B. Cour-Palais and D. K. High. Results of examination of the returned surveyor 3 samples for particulate impacts. *Analysis of Surveyor*, 3:158–167, 1972.

[47] P. A. Cundall and O. D. L. Strack. A discrete numerical model for granular assemblies. *Geotechnique*, 29(1):47–65, 1979.

[48] A. Dadone and B. Grossman. Surface boundary conditions for the numerical solution of the Euler equations. *AIAA Journal*, 32(2):285–293, 1994.

[49] A. Dadone and B. Grossman. Ghost-cell method for analysis of inviscid three-dimensional flows on cartesian-grids. *Computers & Fluids*, 36(10):1513–1528, 2007.

[50] S. L. Davis, G. B. Jacobs, O. Sen, and H. Udaykumar. SPARSE-A subgrid particle averaged Reynolds stress equivalent model: testing with a priori closure. *Proceedings of the Royal Society A: Mathematical, Physical and Engineering Sciences*, 473(2199):20160769, 2017.

[51] B. Delarue and S. Pope. Application of PDF methods to compressible turbulent flows. *Physics of Fluids*, 9(9):2704–2715, 1997.

[52] E. P. DeMauro, J. L. Wagner, S. J. Beresh, and P. A. Farias. Unsteady drag following shock wave impingement on a dense particle curtain measured using pulse-burst PIV. *Physical Review Fluids*, 2(6):064301, 2017.

[53] E. P. DeMauro, J. L. Wagner, L. J. DeChant, S. J. Beresh, and A. M. Turpin. Improved scaling laws for the shock-induced dispersal of a dense particle curtain. *Journal of Fluid Mechanics*, 876:881–895, 2019.

[54] D. Drikakis, D. Ofengeim, E. Timofeev, and P. Voionovich. Computation of non-stationary shock-wave/cylinder interaction using adaptive-grid methods. *Journal of Fluids and Structures*, 11(6):665–692, 1997.

[55] A. Esteghamatian, F. Euzenat, A. Hammouti, M. Lance, and A. Wachs. A stochastic formulation for the drag force based on multiscale numerical simulation of fluidized beds. *International Journal of Multiphase Flow*, 99:363–382, 2018.

[56] E. Fadlun, R. Verzicco, P. Orlandi, and J. Mohd-Yusof. Combined immersed-boundary finite-difference methods for three-dimensional complex flow simulations. *Journal of Computational Physics*, 161(1):35–60, 2000.

[57] E. Feireisl, J. Neustupa, and J. Stebel. Convergence of a Brinkman-type penalization for compressible fluid flows. *Journal of Differential Equations*, 250(1): 596–606, 2011.

[58] R. O. Fox. Large-eddy-simulation tools for multiphase flows. *Annual Review of Fluid Mechanics*, 44:47–76, 2012.

[59] R. O. Fox. A kinetic-based hyperbolic two-fluid model for binary hard-sphere mixtures. *Journal of Fluid Mechanics*, 877:282–329, 2019.

[60] J. B. Freund. Proposed inflow/outflow boundary condition for direct computation of aerodynamic sound. *AIAA Journal*, 35(4):740, 1997.

[61] N. Frink. Recent progress toward a three-dimensional unstructured Navier–Stokes flow solver. In *32nd Aerospace Sciences Meeting and Exhibit*, page 61, 1994.

[62] N. Frink, P. Parikh, and S. Pirzadeh. A fast upwind solver for the Euler equations on three-dimensional unstructured meshes. In *29th Aerospace Sciences Meeting*, page 102, 1991.

[63] T. Fukada, S. Takeuchi, and T. Kajishima. Interaction force and residual stress models for volume-averaged momentum equation for flow laden with particles of comparable diameter to computational grid width. *International Journal of Multiphase Flow*, 85:298–313, 2016.

[64] T. Fukada, W. Fornari, L. Brandt, S. Takeuchi, and T. Kajishima. A numerical approach for particle-vortex interactions based on volume-averaged equations. *International Journal of Multiphase Flow*, 104:188–205, 2018.

[65] M. Gale, K. Buettner, R. Mehta, P. A. Liever, and J. Curtis. Gas-granular flow solver for plume surface interaction and cratering simulations. In *23rd AIAA Computational Fluid Dynamics Conference*, page 4503, 2017.

[66] M. Gale, R. S. Mehta, P. Liever, J. Curtis, and J. Yang. Realistic regolith models for plume-surface interaction in spacecraft propulsive landings. In *AIAA Scitech 2020 Forum*, page 0797, 2020.

[67] R. Ghias, R. Mittal, and H. Dong. A sharp interface immersed boundary method for compressible viscous flows. *Journal of Computational Physics*, 225(1):528–553, 2007.

[68] L. G. Gibilaro, K. Gallucci, R. Di Felice, and P. Pagliai. On the apparent viscosity of a fluidized bed. *Chemical Engineering Science*, 62(1):294–300, 2007.

[69] D. Gidaspow. *Multiphase flow and fluidization: continuum and kinetic theory descriptions*. Academic press, 1994.

[70] D. Goldstein, R. Handler, and L. Sirovich. Modeling a no-slip flow boundary with an external force field. *Journal of Computational Physics*, 105(2):354–366, 1993.

[71] P. Gualtieri, F. Picano, G. Sardina, and C. M. Casciola. Exact regularized point particle method for multiphase flows in the two-way coupling regime. *Journal of Fluid Mechanics*, 773:520–561, 2015.

[72] D. J. Gunn. Transfer of heat and mass to particles in fixed and fluidised beds. *International Journal of Heat Mass Transfer*, 21:467–476, 1978.

[73] L. Guo and J. Capecelatro. The role of clusters on heat transfer in sedimenting gas-solid flows. *International Journal of Heat and Mass Transfer*, 132:1217–1230, 2019.

[74] A. Hagermann, P. Rosenberg, M. Towner, J. Garry, H. Svedhem, M. Leese, B. Hathi, R. Lorenz, and J. Zarnecki. Speed of sound measurements and the methane abundance in Titan's atmosphere. *Icarus*, 189(2):538–543, 2007.

[75] A. D. Hanford and L. N. Long. The direct simulation of acoustics on Earth, Mars, and Titan. *The Journal of the Acoustical Society of America*, 125(2): 640–650, 2009.

[76] M. Hassanalian, D. Rice, and A. Abdelkefi. Evolution of space drones for planetary exploration: A review. *Progress in Aerospace Sciences*, 97:61–105, 2018.

[77] B. Henderson, J. Bridges, and M. Wernet. An experimental study of the oscillatory flow structure of tone-producing supersonic impinging jets. *Journal of Fluid Mechanics*, 542:115, 2005.

[78] C. B. Henderson. Drag coefficients of spheres in continuum and rarefied flows. *AIAA Journal*, 14(6):707–708, 1976.

[79] R. J. Hill, D. L. Koch, and A. J. Ladd. Moderate-Reynolds-number flows in ordered and random arrays of spheres. *Journal of Fluid Mechanics*, 448:243–278, 2001.

[80] S. M. Hörst. Titan's atmosphere and climate. *Journal of Geophysical Research: Planets*, 122(3):432–482, 2017.

[81] J. Horwitz and A. Mani. Accurate calculation of stokes drag for point-particle tracking in two-way coupled flows. *Journal of Computational Physics*, 318: 85–109, 2016.

[82] J. Horwitz and A. Mani. Accurate calculation of stokes drag for point–particle tracking in two-way coupled flows. *Journal of Computational Physics*, 318: 85–109, 2016.

[83] J. Horwitz and A. Mani. Correction scheme for point-particle models applied to a nonlinear drag law in simulations of particle-fluid interaction. *International Journal of Multiphase Flow*, 101:74–84, 2018.

[84] Z. Hosseinzadeh-Nik, S. Subramaniam, and J. D. Regele. Investigation and quantification of flow unsteadiness in shock-particle cloud interaction. *International Journal of Multiphase Flow*, 101:186–201, 2018.

[85] R. W. Houim and E. S. Oran. A multiphase model for compressible granular–gaseous flows: formulation and initial tests. *Journal of Fluid Mechanics*, 789: 166–220, 2016.

[86] S. Hsiao, K. Salari, and S. Balachandar. Pairwaise interaction extended point-particle (piep) model for compressible multiphase problem. *Bulletin of the American Physical Society*, 2020.

[87] Z. Huang, H. Wang, Q. Zhou, and T. Li. Effects of granular temperature on inter-phase drag in gas-solid flows. *Powder Technology*, 321:435–443, 2017.

[88] R. Husted, I. D. Smith, and P. Fennessey. Site Alteration Effects from Rocket Exhaust Impingement During a Simulated Viking Mars Landing. Part 2: Chemical and Biological Site Alteration. 1977.

[89] R. Hutton, H. Moore, R. Scott, R. Shorthill, and C. Spitzer. Surface erosion caused on Mars from Viking descent engine plume. *The Moon and the Planets*, 23(3):293–305, 1980.

[90] R. E. Hutton. Comparison of soil erosion theory with scaled LM jet erosion tests. 1968.

[91] C. Immer, P. Metzger, P. E. Hintze, A. Nick, and R. Horan. Apollo 12 lunar module exhaust plume impingement on lunar Surveyor III. *Icarus*, 211(2):1089–1102, 2011.

[92] A. Irannejad and F. Jaberi. Large eddy simulation of turbulent spray breakup and evaporation. *International Journal of Multiphase Flow*, 61:108–128, 2014.

[93] P. J. Ireland and O. Desjardins. Improving particle drag predictions in Euler–Lagrange simulations with two-way coupling. *Journal of Computational Physics*, 338:405–430, 2017.

[94] F. Ismail and P. L. Roe. Affordable, entropy-consistent euler flux functions II: Entropy production at shocks. *Journal of Computational Physics*, 228(15): 5410–5436, 2009.

[95] K. Jambunathan, E. Lai, M. Moss, and B. Button. A review of heat transfer data for single circular jet impingement. *International Journal of Heat and Fluid Flow*, 13(2):106–115, 1992.

[96] I. Jennions and B. Hunt. The axisymmetric impingement of supersonic air jets on cones. *The Aeronautical Quarterly*, 31(1):26–41, 1980.

[97] Jet Propulsion Laboratory. Mars sample return. URL `https://www.jpl.nasa.gov/missions/mars-sample-return-msr`.

[98] E. Johnsen and S. Lele. Numerical errors generated in simulations of slowly moving shocks. *Center for Turbulence Research, Annual Research Briefs*, pages 1–12, 2008.

[99] R. W. Johnson. *Handbook of Fluid Dynamics*. CRC Press, 2016.

[100] B. Kadoch, D. Kolomenskiy, P. Angot, and K. Schneider. A volume penalization method for incompressible flows and scalar advection–diffusion with moving obstacles. *Journal of Computational Physics*, 231(12):4365–4383, 2012.

[101] G. Kalghatgi and B. Hunt. The occurrence of stagnation bubbles in supersonic jet impingement flows. *The Aeronautical Quarterly*, 27(3):169–185, 1976.

[102] S. K. Kang and Y. A. Hassan. A comparative study of direct-forcing immersed boundary-lattice boltzmann methods for stationary complex boundaries. *International Journal for Numerical Methods in Fluids*, 66(9):1132–1158, 2011.

[103] R. Kannan and Z. Wang. Curvature and entropy based wall boundary condition for the high order spectral volume Euler solver. *Computers & Fluids*, 44(1):79–88, 2011.

[104] C. E. Kees, I. Akkerman, M. W. Farthing, and Y. Bazilevs. A conservative level set method suitable for variable-order approximations and unstructured meshes. *Journal of Computational Physics*, 230(12):4536–4558, 2011.

[105] J. F. Kennedy. The mechanics of dunes and antidunes in erodible-bed channels. *Journal of Fluid mechanics*, 16(4):521–544, 1963.

[106] N. K.-R. Kevlahan and J.-M. Ghidaglia. Computation of turbulent flow past an array of cylinders using a spectral method with Brinkman penalization. *European Journal of Mechanics-B/Fluids*, 20(3):333–350, 2001.

[107] A. G. Kidanemariam and M. Uhlmann. Direct numerical simulation of pattern formation in subaqueous sediment. *Journal of Fluid Mechanics*, 750, 2014.

[108] T. Kim, R. Ni, J. Capecelatro, Y. Yao, G. S. Shallcross, M. Mehta, and J. Rabinovitch. The dynamics of inertial particles in underexpanded jets: An experimental study. In *AIAA Scitech 2020 Forum*, page 1326, 2020.

[109] A. N. Kolmogorov. A refinement of previous hypotheses concerning the local structure of turbulence in a viscous incompressible fluid at high Reynolds number. *Journal of Fluid Mechanics*, 13(1):82–85, 1962.

[110] R. P. Kornfeld, R. Prakash, A. S. Devereaux, M. E. Greco, C. C. Harmon, and D. M. Kipp. Verification and validation of the Mars Science Laboratory/Curiosity rover entry, descent, and landing system. *Journal of Spacecraft and Rockets*, 51(4):1251–1269, 2014.

[111] L. Krivodonova and M. Berger. High-order accurate implementation of solid wall boundary conditions in curved geometries. *Journal of Computational Physics*, 211(2):492–512, 2006.

[112] A. Krothapalli, E. Rajkuperan, F. Alvi, and L. Lourenco. Flow field and noise characteristics of a supersonic impinging jet. In *4th AIAA/CEAS aeroacoustics conference*, page 2239, 1999.

[113] M. Kuhns, P. Metzger, A. Dove, J. Byron, S. Lamb, T. Roberson, L. Lohman, W. Chambers, G. Rixon, R. Kuhns, et al. Deep regolith cratering and plume effects modeling for lunar landing sites. In *Earth and Space 2021*, pages 62–78. 2021.

[114] P. K. Kundu, I. M. Cohen, and D. Dowling. Fluid Mechanics 4th, 2008.

[115] P. Lamont and B. Hunt. The impingement of underexpanded axisymmetric jets on wedges. *Journal of Fluid Mechanics*, 76(2):307–336, 1976.

[116] P. Lamont and B. Hunt. The impingement of underexpanded, axisymmetric jets on perpendicular and inclined flat plates. *Journal of Fluid Mechanics*, 100 (3):471–511, 1980.

[117] N. S. Land and L. V. Clark. *Experimental investigation of jet impingement on surfaces of fine particles in a vacuum environment*. National Aeronautics and Space Administration, 1965.

[118] A. M. Lattanzi, V. Tavanashad, S. Subramaniam, and J. Capecelatro. Stochastic models for capturing dispersion in particle-laden flows. *Journal of Fluid Mechanics*, 903, 2020.

[119] P. Lavoie, G. Blanchard, E. Radenac, E. Laurendeau, and P. Villedieu. A penalization method for 2D ice accretion simulations. Technical report, SAE Technical Paper, 2019.

[120] P. Lavoie, E. Radenac, G. Blanchard, É. Laurendeau, and P. Villedieu. An improved characteristic based volume penalization method for the Euler equations towards icing applications. *Computers & Fluids*, 222:104917, 2021.

[121] D. Lhuillier, C. H. Chang, and T. G. Theofanous. On the quest for a hyperbolic effective-field model of disperse flows. *Journal of Fluid Mechanics*, 731:184–194, 2013.

[122] S. Li and X. Jiang. Review and prospect of guidance and control for Mars atmospheric entry. *Progress in Aerospace Sciences*, 69:40–57, 2014.

[123] H. W. Liepmann and A. Roshko. *Elements of Gasdynamics*. Courier Corporation, 2001.

[124] P. A. Liever, M. P. Gale, R. S. Mehta, and J. S. West. Gas-granular simulation framework for spacecraft landing plume-surface interaction and debris transport analysis. In *Earth and Space 2018: Engineering for Extreme Environments*, pages 39–48. American Society of Civil Engineers Reston, VA, 2018.

[125] Y. Ling, A. Haselbacher, and S. Balachandar. Importance of unsteady contributions to force and heating for particles in compressible flows. Part 2: Application to particle dispersal by blast waves. *International Journal of Multiphase Flow*, 37(9):1013–1025, 2011.

[126] Y. Ling, J. L. Wagner, S. J. Beresh, S. P. Kearney, and S. Balachandar. Interaction of a planar shock wave with a dense particle curtain: Modeling and experiments. *Physics of Fluids*, 24(11):113301, 2012.

[127] Y. Ling, S. Balachandar, and M. Parmar. Inter-phase heat transfer and energy coupling in turbulent dispersed multiphase flows. *Physics of Fluids*, 28(3): 033304, 2016.

[128] M.-S. Liou, L. Nguyen, C.-H. Chang, S. Sushchikh, R. Nourgaliev, and T. Theofanous. Hyperbolicity, discontinuities, and numerics of two-fluid models. In *Computational Fluid Dynamics 2006*, pages 625–630. Springer, 2009.

[129] C. Liu and C. Hu. An immersed boundary solver for inviscid compressible flows. *International Journal for Numerical Methods in Fluids*, 85(11):619–640, 2017.

[130] C. Liu, X. Zheng, and C. H. Sung. Preconditioned multigrid methods for unsteady incompressible flows. *Journal of Computational Physics*, 139(1):35–57, 1998.

[131] Q. Liu and O. V. Vasilyev. A Brinkman penalization method for compressible flows in complex geometries. *Journal of Computational Physics*, 227(2):946–966, 2007.

[132] Q. Liu and O. V. Vasilyev. Nonreflecting boundary conditions based on nonlinear multidimensional characteristics. *International Journal for Numerical Methods in Fluids*, 62(1):24–55, 2010.

[133] E. Loth. Compressibility and rarefaction effects on drag of a spherical particle. *AIAA Journal*, 46(9):2219–2228, 2008.

[134] K. Luo, Y. Luo, T. Jin, and J. Fan. Numerical analysis on shock-cylinder interaction using immersed boundary method. *Science China Technological Sciences*, 60(9):1423–1432, 2017.

[135] D. Mackenzie. The gritty problem of Moon dust. *NewScientist*, 2005. URL `https://www.newscientist.com/article/mg18625012-000-the-gritty-problem-of-moo`

[136] A. Mani, J. Larsson, and P. Moin. Suitability of artificial bulk viscosity for large-eddy simulation of turbulent flows with shocks. *Journal of Computational Physics*, 228(19):7368–7374, 2009.

[137] Mars Exploration Program and the Jet Propulsion Laboratory. Mars Curiosity Rover, Timeline: Entry, Descent, and Landing. URL `https://mars.nasa.gov/msl/timeline/edl/`.

[138] H. Martin. Heat and mass transfer between impinging gas jets and solid surfaces. In *Advances in heat transfer*, volume 13, pages 1–60. Elsevier, 1977.

[139] N. Mason-Smith, D. Edgington-Mitchell, N. A. Buchmann, D. R. Honnery, and J. Soria. Shock structures and instabilities formed in an underexpanded jet impinging on to cylindrical sections. *Shock Waves*, 25(6):611–622, 2015.

[140] K. Mattsson, M. Svärd, and J. Nordström. Stable and accurate artificial dissipation. *Journal of Scientific Computing*, 21(1):57–79, 2004.

[141] D. J. Mavriplis. Accurate multigrid solution of the Euler equations on unstructured and adaptive meshes. *AIAA Journal*, 28(2):213–221, 1990.

[142] D. J. Mavriplis. Mesh generation and adaptivity for complex geometries and flows. In *Handbook of Computational Fluid Mechanics*, pages 417–459. Elsevier, 1996.

[143] M. R. Maxey and J. J. Riley. Equation of motion for a small rigid sphere in a nonuniform flow. *Physics of Fluids*, 26(4):883–889, 1983.

[144] M. R. Maxey, B. K. Patel, E. J. Chang, and L. P. Wang. Simulations of dispersed turbulent multiphase flow. *Fluid Dynamics Research*, 20(1-6):143, 1997.

[145] J. B. McLaughlin et al. Inertial migration of a small sphere in linear shear flows. *J. Fluid Mech*, 224(261-274):332, 1991.

[146] M. Mehrabadi, S. Tenneti, R. Garg, and S. Subramaniam. Pseudo-turbulent gas-phase velocity fluctuations in homogeneous gas–solid flow: fixed particle assemblies and freely evolving suspensions. *Journal of Fluid Mechanics*, 770: 210–246, 2015.

[147] M. Mehta, N. O. Renno, J. Marshall, M. R. Grover, A. Sengupta, N. A. Rusche, J. F. Kok, R. E. Arvidson, W. J. Markiewicz, M. T. Lemmon, et al. Explosive erosion during the Phoenix landing exposes subsurface water on Mars. *Icarus*, 211(1):172–194, 2011.

[148] M. Mehta, A. Sengupta, N. O. Renno, J. W. V. Norman, P. G. Huseman, D. S. Gulick, and M. Pokora. Thruster plume surface interactions: Applications for spacecraft landings on planetary bodies. *AIAA Journal*, 51(12):2800–2818, 2013.

[149] R. S. Mehta, P. A. Liever, J. L. Salmon, K. E. Buettner, and J. S. Curtis. Particle flow physics modeling for extreme environments. In *Earth and Space 2016: Engineering for Extreme Environments*, pages 131–141. American Society of Civil Engineers Reston, VA, 2016.

[150] Y. Mehta, C. Neal, T. Jackson, S. Balachandar, and S. Thakur. Shock interaction with three-dimensional face centered cubic array of particles. *Physical Review Fluids*, 1(5):054202, 2016.

[151] Y. Mehta, C. Neal, K. Salari, T. L. Jackson, S. Balachandar, and S. Thakur. Propagation of a strong shock over a random bed of spherical particles. *Journal of Fluid Mechanics*, 839:157–197, 2018.

[152] Y. Mehta, T. L. Jackson, and S. Balachandar. Pseudo-turbulence in inviscid simulations of shock interacting with a bed of randomly distributed particles. *Shock Waves*, pages 1–14, 2019.

[153] Y. Mehta, K. Salari, T. L. Jackson, and S. Balachandar. Effect of Mach number and volume fraction in air-shock interacting with a bed of randomly distributed spherical particles. *Physical Review Fluids*, 4(1):014303, 2019.

[154] P. T. Metzger, J. E. Lane, and C. D. Immer. Modification of roberts' theory for rocket exhaust plumes eroding lunar soil. In *Earth & Space 2008: Engineering, Science, Construction, and Operations in Challenging Environments*, pages 1–8. 2008.

[155] P. T. Metzger, C. D. Immer, C. M. Donahue, B. T. Vu, R. C. Latta III, and M. Deyo-Svendsen. Jet-induced cratering of a granular surface with application to lunar spaceports. *Journal of Aerospace Engineering*, 22(1):24–32, 2009.

[156] P. T. Metzger, J. Smith, and J. E. Lane. Phenomenology of soil erosion due to rocket exhaust on the Moon and the Mauna Kea lunar test site. *Journal of Geophysical Research: Planets*, 116(E6), 2011.

[157] D. G. Miller and A. B. Bailey. Sphere drag at Mach numbers from 0· 3 to 2· 0 at Reynolds numbers approaching 10 7. *Journal of Fluid Mechanics*, 93(3): 449–464, 1979.

[158] J.-P. Minier and E. Peirano. The PDF approach to turbulent polydispersed two-phase flows. *Physics reports*, 352(1-3):1–214, 2001.

[159] J.-P. Minier, E. Peirano, and S. Chibbaro. Pdf model based on langevin equation for polydispersed two-phase flows applied to a bluff-body gas-solid flow. *Physics of fluids*, 16(7):2419–2431, 2004.

[160] J.-P. Minier, S. Chibbaro, and S. B. Pope. Guidelines for the formulation of Lagrangian stochastic models for particle simulations of single-phase and dispersed two-phase turbulent flows. *Physics of Fluids*, 26(11):113303, 2014.

[161] R. Mittal and G. Iaccarino. Immersed boundary methods. *Annual Review of Fluid Mechanics*, 37:239–261, 2005.

[162] R. Mittal, H. Dong, M. Bozkurttas, F. Najjar, A. Vargas, and A. Von Loebbecke. A versatile sharp interface immersed boundary method for incompressible flows with complex boundaries. *Journal of Computational Physics*, 227(10):4825–4852, 2008.

[163] J. Mohd-Yusof. Combined immersed-boundary/B-spline methods for simulations of flow in complex geometries. *Center for Turbulence Research Annual Research Briefs*, 161(1):317–327, 1997.

[164] H. J. Moore, R. E. Hutton, R. F. Scott, C. R. Spitzer, and R. W. Shorthill. Surface materials of the viking landing sites. *Journal of Geophysical Research*, 82(28):4497–4523, 1977.

[165] W. Moore, S. Balachandar, and G. Akiki. A hybrid point-particle force model that combines physical and data-driven approaches. *Journal of Computational Physics*, 385:187–208, 2019.

[166] A. B. Morris et al. *Simulation of rocket plume impingement and dust dispersal on the lunar surface*. PhD thesis, University of Texas, 2012.

[167] T. Nagata, T. Nonomura, S. Takahashi, Y. Mizuno, and K. Fukuda. Investigation on subsonic to supersonic flow around a sphere at low Reynolds number of between 50 and 300 by direct numerical simulation. *Physics of Fluids*, 28(5): 056101, 2016.

[168] T. Nagata, T. Nonomura, S. Takahashi, Y. Mizuno, and K. Fukuda. Direct numerical simulation of flow around a heated/cooled isolated sphere up to a reynolds number of 300 under subsonic to supersonic conditions. *International Journal of Heat and Mass Transfer*, 120:284–299, 2018.

[169] J. Nordström and M. Svärd. Well-posed boundary conditions for the Navier–Stokes equations. *SIAM Journal on Numerical Analysis*, 43(3):1231–1255, 2005.

[170] C. W. Oseen. Neuere methoden und ergebnisse in der hydrodynamik. *Leipzig: Akademische Verlagsgesellschaft mb H.*, 1927.

[171] A. N. Osnes, M. Vartdal, M. G. Omang, and B. A. P. Reif. Computational analysis of shock-induced flow through stationary particle clouds. *International Journal of Multiphase Flow*, 114:268–286, 2019.

[172] A. N. Osnes, M. Vartdal, M. G. Omang, and B. A. P. Reif. Particle-resolved simulations of shock-induced flow through particle clouds at different Reynolds numbers. *arXiv preprint arXiv:1906.08299*, 2019.

[173] A. N. Osnes, M. Vartdal, M. G. Omang, and B. A. P. Reif. Particle-resolved simulations of shock-induced flow through particle clouds at different Reynolds numbers. *Physical Review Fluids*, 5(1):014305, 2020.

[174] N. T. Ouellette, H. Xu, and E. Bodenschatz. A quantitative study of three-dimensional lagrangian particle tracking algorithms. *Experiments in Fluids*, 40 (2):301–313, 2006.

[175] S. P. Pardhasaradhi, V. Venkatachalapathy, S. V. Joshi, and S. Govindan. Optical diagnostics study of gas particle transport phenomena in cold gas dynamic spraying and comparison with model predictions. *Journal of Thermal Spray Technology*, 17(4):551–563, 2008.

[176] G. I. Park, M. Bassenne, J. Urzay, and P. Moin. A simple dynamic subgrid-scale model for LES of particle-laden turbulence. *Physical Review Fluids*, 2(4): 044301, 2017.

[177] M. Parmar, A. Haselbacher, and S. Balachandar. Improved drag correlation for spheres and application to shock-tube experiments. *AIAA Journal*, 48(6): 1273–1276, 2010.

[178] M. Parmar, A. Haselbacher, and S. Balachandar. Generalized Basset-Boussinesq-Oseen equation for unsteady forces on a sphere in a compressible flow. *Physical Review Letters*, 106(8):084501, 2011.

[179] M. Parmar, A. Haselbacher, and S. Balachandar. Equation of motion for a sphere in non-uniform compressible flows. *Journal of Fluid Mechanics*, 699: 352–375, 2012.

[180] N. Patankar and D. Joseph. Modeling and numerical simulation of particulate flows by the Eulerian-Lagrangian approach. *International Journal of Multiphase Flow*, 27(10):1659–1684, 2001.

[181] C. Peng, B. Kong, A. Passalacqua, S. Subramaniam, and R. O. Fox. Implementation of pseudo-turbulence closures in an Eulerian-Eulerian two-fluid model for non-isothermal gas–solid flow. *Chemical Engineering Science*, Under review, 2019.

[182] P. Pepiot and O. Desjardins. Numerical analysis of the dynamics of two-and three-dimensional fluidized bed reactors using an Euler–Lagrange approach. *Powder Technology*, 220:104–121, 2012.

[183] C. S. Peskin. Flow patterns around heart valves: a numerical method. *Journal of Computational Physics*, 10(2):252–271, 1972.

[184] C. S. Peskin. The immersed boundary method. *Acta Numerica*, 11:479–517, 2002.

[185] A. Petculescu and R. Kruse. Predicting the characteristics of thunder on Titan: A framework to assess the detectability of lightning by acoustic sensing. *Journal of Geophysical Research: Planets*, 119(10):2167–2176, 2014.

[186] B. Petropoulos and C. Macris. Physical parameters of the Martian atmosphere. *Earth, Moon, and Planets*, 46(1):1–30, 1989.

[187] A. Piquet, O. Roussel, and A. Hadjadj. A comparative study of Brinkman penalization and direct-forcing immersed boundary methods for compressible viscous flows. *Computers & Fluids*, 136:272–284, 2016.

[188] S. Pirozzoli. Stabilized non-dissipative approximations of euler equations in generalized curvilinear coordinates. *Journal of Computational Physics*, 230(8): 2997–3014, 2011.

[189] S. Pope. *Turbulent flows*. Cambridge university press, 2000.

[190] S. B. Pope. Lagrangian PDF methods for turbulent flows. *Annual Review of Fluid Mechanics*, 26(1):23–63, 1994.

[191] J. Pozorski and S. V. Apte. Filtered particle tracking in isotropic turbulence and stochastic modeling of subgrid-scale dispersion. *International Journal of Multiphase Flow*, 35(2):118–128, 2009.

[192] R. Prakash, P. D. Burkhart, A. Chen, K. A. Comeaux, C. S. Guernsey, D. M. Kipp, L. V. Lorenzoni, G. F. Mendeck, R. W. Powell, T. P. Rivellini, et al. Mars Science Laboratory entry, descent, and landing system overview. In *2008 IEEE Aerospace Conference*, pages 1–18. IEEE, 2008.

[193] B. Rajani, A. Kandasamy, and S. Majumdar. Numerical simulation of laminar flow past a circular cylinder. *Applied Mathematical Modelling*, 33(3):1228–1247, 2009.

[194] J. T. Rasmussen, G.-H. Cottet, and J. H. Walther. A multiresolution remeshed vortex-in-cell algorithm using patches. *Journal of Computational Physics*, 230 (17):6742–6755, 2011.

[195] J. D. Regele, J. Rabinovitch, T. Colonius, and G. Blanquart. Unsteady effects in dense, high speed, particle laden flows. *International Journal of Multiphase Flow*, 61:1–13, 2014.

[196] L. Roberts. The action of a hypersonic jet on a dusty surface. *Institute of the Aerospace Sciences*, pages 63–50, 1963.

[197] D. J. Roddy, J. B. Rittenhouse, and R. F. Scott. Dynamic penetration studies in crushed rock under atmospheric and vacuum conditions. *AIAA Journal*, 1 (4):868–873, 1963.

[198] A. M. Roma, C. S. Peskin, and M. J. Berger. An adaptive version of the immersed boundary method. *Journal of Computational Physics*, 153(2):509–534, 1999.

[199] Y. Saad. *Iterative methods for sparse linear systems*. SIAM, 2003.

[200] P. Saffman. The lift on a small sphere in a slow shear flow. *Journal of Fluid Mechanics*, 22(2):385–400, 1965.

[201] E. Saiki and S. Biringen. Numerical simulation of a cylinder in uniform flow: application of a virtual boundary method. *Journal of Computational Physics*, 123(2):450–465, 1996.

[202] T. Saito, M. Marumoto, and K. Takayama. Numerical investigations of shock waves in gas-particle mixtures. *Shock Waves*, 13(4):299–322, 2003.

[203] J.-M. Salotti and E. Suhir. Manned missions to Mars: Minimizing risks of failure. *Acta Astronautica*, 93:148–161, 2014.

[204] S. Schneiderbauer and M. Saeedipour. Approximate deconvolution model for the simulation of turbulent gas-solid flows: An a priori analysis. *Physics of Fluids*, 30(2):023301, 2018.

[205] S. Schneiderbauer and M. Saeedipour. Numerical simulation of turbulent gas-solid flow using an approximate deconvolution model. *International Journal of Multiphase Flow*, 2019.

[206] R. F. Scott and H.-Y. KO. Transient rocket-engine gas flow in soil. *AIAA Journal*, 6(2):258–264, 1968.

[207] O. Sen, N. J. Gaul, S. Davis, K. K. Choi, G. Jacobs, and H. S. Udaykumar. Role of pseudo-turbulent stresses in shocked particle clouds and construction of surrogate models for closure. *Shock Waves*, pages 1–19, 2018.

[208] A. Sengupta, J. Kulleck, S. Sell, J. Van Norman, M. Mehta, and M. Pokora. Mars lander engine plume impingement environment of the Mars Science Laboratory. In *2009 IEEE Aerospace conference*, pages 1–10. IEEE, 2009.

[209] A. Sengupta, J. Kulleck, J. Van Norman, and M. Mehta. Thermal coating erosion in a simulated Martian landing environment. *Wear*, 270(5-6):335–343, 2011.

[210] J. A. Sethian and P. Smereka. Level set methods for fluid interfaces. *Annual Review of Fluid Mechanics*, 35(1):341–372, 2003.

[211] G. S. Shallcross and J. Capecelatro. A parametric study of particle-laden shock tubes using an Eulerian–Lagrangian framework. In *2018 AIAA Aerospace Sciences Meeting*, page 2080, 2018.

[212] G. S. Shallcross and J. Capecelatro. Eulerian–Lagrangian study of jet impingement on granular beds. In Preparation.

[213] G. S. Shallcross and J. Capecelatro. An explicit characteristic-based immersed boundary method for compressible flows. *Journal of Computational Physics*, Under Review.

[214] G. S. Shallcross, R. O. Fox, and J. Capecelatro. A volume-filtered description of compressible particle-laden flows. *International Journal of Multiphase Flow*, 122:103138, 2020.

[215] B. Sjögreen and H. Yee. On skew-symmetric splitting and entropy conservation schemes for the euler equations. In *Numerical Mathematics and Advanced Applications 2009*, pages 817–827. Springer, 2010.

[216] R. S. Snedeker et al. A study of free jet impingement. Part 1. Mean properties of free and impinging jets. *Journal of Fluid Mechanics*, 45(2):281–319, 1971.

[217] M. Sommerfeld. The structure of particle-laden, underexpanded free jets. *Shock Waves*, 3(4):299–311, 1994.

[218] A. D. Steltzner, A. Miguel San Martin, T. P. Rivellini, A. Chen, and D. Kipp. Mars Science Laboratory entry, descent, and landing system development challenges. *Journal of Spacecraft and Rockets*, 51(4):994–1003, 2014.

[219] S. Stolz and N. A. Adams. An approximate deconvolution procedure for large-eddy simulation. *Physics of Fluids*, 11(7):1699–1701, 1999.

[220] B. Strand. Summation by parts for finite difference approximations for d/dx. *Journal of Computational Physics*, 110(1):47–67, 1994.

[221] B. Sun, S. Tenneti, and S. Subramaniam. Modeling average gas–solid heat transfer using particle-resolved direct numerical simulation. *International Journal of Heat and Mass Transfer*, 86:898–913, 2015.

[222] M. Sun, T. Saito, K. Takayama, and H. Tanno. Unsteady drag on a sphere by shock wave loading. *Shock Waves*, 14(1-2):3–9, 2005.

[223] M. Sussman. *A level set approach for computing solutions to incompressible two-phase flow*. PhD thesis, Department of Mathematics, University of California, Los Angeles, 1994.

[224] V. S. Sutkar, N. G. Deen, A. V. Patil, V. Salikov, S. Antonyuk, S. Heinrich, and J. A. M. Kuipers. CFD–DEM model for coupled heat and mass transfer in a spout fluidized bed with liquid injection. *Chemical Engineering Journal*, 288: 185–197, 2016.

[225] M. Svärd. On coordinate transformations for summation-by-parts operators. *Journal of Scientific Computing*, 20(1):29–42, 2004.

[226] M. Svärd and J. Nordström. A stable high-order finite difference scheme for the compressible Navier–Stokes equations: no-slip wall boundary conditions. *Journal of Computational Physics*, 227(10):4805–4824, 2008.

[227] M. Svärd, M. H. Carpenter, and J. Nordström. A stable high-order finite difference scheme for the compressible Navier–Stokes equations, far-field boundary conditions. *Journal of Computational Physics*, 225(1):1020–1038, 2007.

[228] S. Takahashi, T. Nonomura, and K. Fukuda. A numerical scheme based on an immersed boundary method for compressible turbulent flows with shocks: application to two-dimensional flows around cylinders. *Journal of Applied Mathematics*, 2014, 2014.

[229] K. Takayama and K. Itoh. Unsteady drag over cylinders and aerofoils in transonic shock tube flows. *Shock Waves and Shock Tubes*, pages 479–485, 1986.

[230] S. Tan and C.-W. Shu. A high order moving boundary treatment for compressible inviscid flows. *Journal of Computational Physics*, 230(15):6023–6036, 2011.

[231] S. Taverniers, H. Udaykumar, and G. B. Jacobs. Two-way coupled Cloud-In-Cell modeling of non-isothermal particle-laden flows: A Subgrid Particle-Averaged Reynolds Stress-Equivalent (SPARSE) formulation. *Journal of Computational Physics*, 390:595–618, 2019.

[232] S. Tenneti and S. Subramaniam. Particle-resolved direct numerical simulation for gas-solid flow model development. *Annual Review of Fluid Mechanics*, 46: 199–230, 2014.

[233] S. Tenneti, R. Garg, and S. Subramaniam. Drag law for monodisperse gas–solid systems using particle-resolved direct numerical simulation of flow past fixed assemblies of spheres. *International Journal of Multiphase Flow*, 37(9): 1072–1092, 2011.

[234] S. Tenneti, B. Sun, R. Garg, and S. Subramaniam. Role of fluid heating in dense gas–solid flow as revealed by particle-resolved direct numerical simulation. *International Journal of Heat and Mass Transfer*, 58(1):471–479, 2013.

[235] S. Tenneti, M. Mehrabadi, and S. Subramaniam. Stochastic lagrangian model for hydrodynamic acceleration of inertial particles in gas-solid suspensions. *Journal of Fluid Mechanics*, 788:695, 2016.

[236] T. G. Theofanous and C. H. Chang. The dynamics of dense particle clouds subjected to shock waves. Part 2. Modeling/numerical issues and the way forward. *International Journal of Multiphase Flow*, 89:177–206, 2017.

[237] T. G. Theofanous, V. Mitkin, and C.-H. Chang. The dynamics of dense particle clouds subjected to shock waves. Part 1. Experiments and scaling laws. *Journal of Fluid Mechanics*, 792:658–681, 2016.

[238] T. G. Theofanous, V. Mitkin, and C.-H. Chang. Shock dispersal of dilute particle clouds. *Journal of Fluid Mechanics*, 841:732–745, 2018.

[239] A. Tosh, P. A. Liever, R. R. Arslanbekov, and S. D. Habchi. Numerical analysis of spacecraft rocket plume impingement under lunar environment. *Journal of Spacecraft and Rockets*, 48(1):93–102, 2011.

[240] Y.-H. Tseng and J. H. Ferziger. A ghost-cell immersed boundary method for flow in complex geometry. *Journal of Computational Physics*, 192(2):593–623, 2003.

[241] C. Tu and C. S. Peskin. Stability and instability in the computation of flows with moving immersed boundaries: a comparison of three methods. *SIAM Journal on Scientific and Statistical Computing*, 13(6):1361–1376, 1992.

[242] J. W. Tukey. An intoroduction to the calculation of numerical spectrum analysis. *Spectra Analysis of Time Series*, pages 25–46, 1967.

[243] G. E. Uhlenbeck and L. S. Ornstein. On the theory of the Brownian motion. *Physical review*, 36(5):823, 1930.

[244] M. Uhlmann. An immersed boundary method with direct forcing for the simulation of particulate flows. *Journal of Computational Physics*, 209(2):448–476, 2005.

[245] O. Vasilyev and N.-R. Kevlahan. Hybrid wavelet collocation–Brinkman penalization method for complex geometry flows. *International Journal for Numerical Methods in Fluids*, 40(3-4):531–538, 2002.

[246] J. C. Vassilicos. Dissipation in turbulent flows. *Annual Review of Fluid Mechanics*, 47:95–114, 2015.

[247] R. Vishnampet Ganapathi Subramanian. *An exact and consistent adjoint method for high-fidelity discretization of the compressible flow equations*. PhD thesis, University of Illinois at Urbana-Champaign, 2015.

[248] R. Viskanta. Heat transfer to impinging isothermal gas and flame jets. *Experimental thermal and fluid science*, 6(2):111–134, 1993.

[249] J. L. Wagner, S. J. Beresh, S. P. Kearney, W. M. Trott, J. N. Castaneda, B. O. Pruett, and M. R. Baer. A multiphase shock tube for shock wave interactions with dense particle fields. *Experiments in Fluids*, 52(6):1507–1517, 2012.

[250] J. L. Wagner, S. P. Kearney, S. J. Beresh, E. P. DeMauro, and B. O. Pruett. Flash x-ray measurements on the shock-induced dispersal of a dense particle curtain. *Experiments in Fluids*, 56(12):213, 2015.

[251] T. Watanabe, Y. Sakai, K. Nagata, Y. Ito, and T. Hayase. LES–Lagrangian particle method for turbulent reactive flows based on the approximate deconvolution model and mixing model. *Journal of Computational Physics*, 294: 127–148, 2015.

[252] B. Webb and C.-F. Ma. Single-phase liquid jet impingement heat transfer. In *Advances in Heat Transfer*, volume 26, pages 105–217. Elsevier, 1995.

[253] J. Wilkes Inman, P. Danehy, R. Nowak, and D. Alderfer. Fluorescence imaging study of impinging underexpanded jets. In *46th AIAA Aerospace Sciences Meeting and Exhibit*, page 619, 2008.

[254] Z. Xia, Y. Shi, Q. Zhang, and S. Chen. Modulation to compressible homogenous turbulence by heavy point particles. I. Effect of particles' density. *Physics of Fluids*, 28(1):016103, 2016.

[255] Y. Yao and J. Capecelatro. An accurate particle-mesh method for simulating charged particles in wall-bounded flows. *Powder Technology*, 387:239–250, 2021.

[256] Y. Yao, G. S. Shallcross, R. Ni, T. Kim, M. Mehta, J. Rabinovitch, and J. Capecelatro. The dynamics of inertial particles in under-expanded jets: A numerical study. In *AIAA Scitech 2020 Forum*, page 1327, 2020.

[257] D. W. Zaide and P. L. Roe. Flux functions for reducing numerical shockwave anomalies. *ICCFD7, Big Island, Hawaii*, pages 9–13, 2012.

[258] D. Zhang and A. Prosperetti. Momentum and energy equations for disperse two-phase flows and their closure for dilute suspensions. *International Journal of Multiphase Flow*, 23(3):425–453, 1997.

[259] N. Zhang and Z. C. Zheng. An improved direct-forcing immersed-boundary method for finite difference applications. *Journal of Computational Physics*, 221(1):250–268, 2007.

[260] Y. Zhang and C. Zhou. An immersed boundary method for simulation of inviscid compressible flows. *International Journal for Numerical Methods in Fluids*, 74 (11):775–793, 2014.

[261] K. Zhou and S. Balachandar. An analysis of the spatio-temporal resolution of the immersed boundary method with direct forcing. *Journal of Computational Physics*, page 109862, 2020.